

# **Technologies for System-on-Textile Integration**

A dissertation submitted to the  
SWISS FEDERAL INSTITUTE OF TECHNOLOGY  
ZURICH  
for the degree of  
Doctor of Sciences

presented by  
IVO LOCHER  
MSc., University of California, Los Angeles  
born 11th April 1973  
citizen of Remetschwil, Switzerland

accepted on the recommendation of  
Prof. Dr. Gerhard Tröster, examiner  
Prof. Dr. Lieva Van Langenhove, co-examiner

2006



## Acknowledgements

First of all, I would like to thank my advisor Prof. Gerhard Tröster for his support and valuable inputs during my work at the Institute for Electronics. Especially, his substantial comments to paper writing have led to many published papers. I would also like to thank Prof. Lieva Van Langenhove for co-examining and for her inputs to my dissertation.

Secondly, I owe thank to my co-advisor, Dr. Tünde Kirstein. She could provide many contacts to industry.

High appreciation belongs to Christoph Maurer from Sefar Inc., Filtration division. This dissertation would not have been possible without his support. Our collaboration has been very fruitful resulting in 2 patent submissions and a successful exhibition at Techtextil 2005. I would further like to thank Dr. Helen Vogt, Marcel Strotz and Daniel Odermatt from Sefar Inc. for their support and the discussions.

Thomas Hartl from Sefar Inc., Printing division has been a big support for manufacturing of conductive structures printed on fabrics.

Big thanks go to Dr. Beat Neuenschwander from HTI Burgdorf, Thomas Dumont from PSI and Enrico Ortelli from Dyconex AG for supporting my research work in laser ablation of polymer coatings. In this context, I also appreciate Peter Beil and Thomas Neubert from ILFA GmbH for their immediate agreement to laser treat our electronic fabrics.

Special thank also goes to Hansruedi Benedickter from IFH. He has been a big help giving many valuable inputs during RF measurements of electronic fabrics and antennas.

Horst Adelman from Institute of Food Science and Nutrition at ETHZ and Hans-Juerg Weber from EEH deserve a big thank for allowing me to use the climate chambers for my moisture measurements.

Further, I would like to thank Peter Karlsson from Hilpert Electronics AG for his support in dispensing of adhesives and for lending dispensing equipment.

Regarding my labmates, I sincerely appreciate the help of Maciej Klemm and his collaboration in development of textile patch antennas. Secondly, big thank goes to the former lab mates Didier Cottet and Janusz Grzyb for their support in RF measurements and evaluations. I would also like to thank my labmates Thomas von Büren, Mathias Stäger, Stijn Ossevoort, Oliver Amft and Thomas Stiefmeier for many fruitful discussions and collaborations in

the course work.

In addition, I owe thank to Heinrich Maag for the many PCBs he has etched for me. Thank goes also to my sister Silvia for proof reading the English grammar of my dissertation.

Eventually, I would like to thank my parents and my girlfriend Isabel for giving me a balance towards the scientific world.

Zürich, February 2006

Ivo Locher

# Contents

<b>Abstract</b>	<b>vii</b>
<b>Zusammenfassung</b>	<b>ix</b>
<b>1. Introduction</b>	<b>1</b>
1.1. Our vision of wearable computing . . . . .	2
1.2. Miscellaneous approaches to integrate electronics into fabrics . . . . .	4
1.3. Conductive fabric variants . . . . .	8
1.4. Summary . . . . .	11
<b>2. Motivation</b>	<b>13</b>
2.1. Covered topics in the dissertation . . . . .	14
2.2. Proof-of-concept . . . . .	15
2.2.1. Block diagram of the Fabric Integrated Wireless Temperature Sensor . . . . .	15
2.2.2. Implementation of the Fabric Integrated Wireless Temperature Sensor . . . . .	15
2.2.3. Outline to the chapters . . . . .	17
<b>3. Integration Technologies</b>	<b>19</b>
3.1. Introduction . . . . .	20
3.1.1. Related Work . . . . .	20
3.2. Textile substrates with embedded copper wires . . . . .	20
3.2.1. Fabric versions 0-3 . . . . .	20
3.2.2. Fabric version 4, PETEX . . . . .	21
3.3. Wire-based textile transmission lines . . . . .	25
3.3.1. Transmission line structures . . . . .	25
3.3.2. Electrical measurement results . . . . .	26
3.4. Screen-printed textile transmission lines . . . . .	36
3.4.1. Textile substrate and printing ink . . . . .	37
3.4.2. Screen-printing . . . . .	37
3.4.3. Transmission line structure . . . . .	38
3.4.4. Electrical measurement results . . . . .	39
3.4.5. Mechanical stresses . . . . .	41
3.4.6. Results and Conclusions . . . . .	43

3.5.	Textile vias and interconnects . . . . .	43
3.5.1.	Manufacturing of a textile via . . . . .	44
3.5.2.	Determination of the laser parameters . . . . .	44
3.5.3.	Wire interconnect with conductive adhesive . . . . .	50
3.5.4.	Epoxy encapsulation as mechanical protection . . . . .	50
3.5.5.	Electrical characterization of a textile via . . . . .	51
3.6.	Interposer Technology . . . . .	55
3.6.1.	Introduction and Motivation . . . . .	55
3.6.2.	Interposer Approach . . . . .	57
3.6.3.	Interposer types . . . . .	59
3.6.4.	Footprint area of an interposer . . . . .	62
3.6.5.	Reduction of occupied interposer area . . . . .	63
3.6.6.	Further considerations . . . . .	64
3.6.7.	Assembly of an interposer . . . . .	64
3.6.8.	Inductivity of an interposer connect . . . . .	65
3.7.	Circuit protection tests . . . . .	67
3.7.1.	Tensile stress test on fabric . . . . .	67
3.7.2.	Moisture absorption of epoxy encapsulation . . . . .	71
<b>4.</b>	<b>Textile Routing</b>	<b>77</b>
4.1.	Introduction . . . . .	78
4.2.	Component placement . . . . .	78
4.3.	Textile routing implementation . . . . .	78
4.3.1.	Method 1 for 'cut step' . . . . .	79
4.3.2.	Method 2 for 'cut step' . . . . .	80
4.3.3.	Routing considerations . . . . .	82
4.4.	Signal wiring . . . . .	82
4.5.	Routing strategy . . . . .	83
4.5.1.	Routing strategy applied to the Fabric Integrated Wireless Temperature Sensor . . . . .	85
4.6.	Routing constraint summary . . . . .	86
<b>5.</b>	<b>Wireless Connection Technology in Fabrics</b>	<b>87</b>
5.1.	Introduction . . . . .	88
5.2.	Patch antenna design approach . . . . .	88
5.3.	Related work . . . . .	90
5.4.	Textile materials . . . . .	90
5.4.1.	Electrically conductive fabric . . . . .	90
5.4.2.	Silver plated knitted fabric (1) . . . . .	92
5.4.3.	Silver-copper-nickel plated woven fabric (2) . . . . .	92

5.4.4.	Plating thickness . . . . .	93
5.4.5.	Textile substrates . . . . .	93
5.5.	Antenna design . . . . .	95
5.5.1.	Antenna feed . . . . .	95
5.5.2.	Antenna insets . . . . .	96
5.6.	Antenna manufacturing . . . . .	96
5.7.	Antenna simulation and measurement results . . . . .	99
5.7.1.	Antenna bending gauge . . . . .	99
5.7.2.	Antenna interconnect for measurements . . . . .	100
5.7.3.	Return loss . . . . .	101
5.7.4.	Radiation patterns . . . . .	103
5.7.5.	Axial ratio (AR) . . . . .	106
5.8.	Conclusion . . . . .	107
<b>6.</b>	<b>Fabric Embedded Temperature Sensor</b>	<b>109</b>
6.1.	Introduction . . . . .	110
6.2.	Measurement concept . . . . .	110
6.2.1.	Electronic measurement circuit . . . . .	110
6.2.2.	Theoretical temperature measurement accuracy . . . . .	111
6.3.	Fabric temperature sensors . . . . .	112
6.3.1.	Array grid sensor . . . . .	112
6.3.2.	Meander-shaped sensor . . . . .	112
6.3.3.	Comparison of the sensor variants . . . . .	113
6.4.	Temperature profile estimation . . . . .	114
6.5.	Temperature measurement accuracy . . . . .	115
6.5.1.	Calibration and determination of $\alpha_{metal}$ . . . . .	115
6.5.2.	Measured temperature distribution . . . . .	116
6.6.	Conclusion . . . . .	116
<b>7.</b>	<b>Conclusions</b>	<b>119</b>
7.1.	Achievements . . . . .	119
7.2.	Outlook . . . . .	120
	<b>Appendix</b>	<b>123</b>
<b>A.</b>	<b>Transmission Lines</b>	<b>123</b>
A.1.	Introduction . . . . .	123
A.2.	Transmission line parameter extraction . . . . .	124
A.3.	Textile transmission line characterization . . . . .	126
A.3.1.	Measurement perturbations . . . . .	126
A.3.2.	Unwrapping of a perturbed phase . . . . .	126

<b>B. Matrix definitions and conversions</b>	<b>129</b>
<b>C. Practical textile routing hints</b>	<b>131</b>
C.1. Interposer design . . . . .	131
C.2. EDA tool configuration for textile layout . . . . .	132
C.3. Correction of layout coordinates . . . . .	132
C.4. Fabrication files . . . . .	132
<b>D. Potential temperature measurement circuit</b>	<b>135</b>
<b>Glossary</b>	<b>137</b>
<b>Bibliography</b>	<b>141</b>
<b>Curriculum Vitae</b>	<b>151</b>



## Abstract

Wearable computing demands a smooth and unobtrusive integration of electronics into clothing in order to achieve user acceptance. A *Fabric Integrated Wireless Temperature Sensor* is presented as proof-of-concept in this dissertation highlighting the required technologies for successful realization. These novel technologies propose various approaches for a smooth integration of electronic components into fabrics. We summarize these technologies under the term *System-on-Textile* (SoT).

The dissertation focuses on a woven polyester fabric with embedded thin copper wires as substrate for the electronics. Each copper wire itself is insulated with a thin polymer coating. Using this substrate, different transmission line configurations are first evaluated regarding electrical performance. They feature bandwidths up to  $2GHz$ . It is shown that the usual  $50\Omega$  line impedance cannot be achieved. The obtained impedances lie in the range between  $180 - 310\Omega$ .

An interconnect technology is presented to establish arbitrary wiring structures among the wires in the fabric. These interconnects show only minor effects on signal transmission. Secondly, our approach for chip assembly utilizes an innovative interposer design such that arbitrary electronic components can easily be mounted onto the fabric. We identify routing strategies and constraints for signal and power wiring within the fabric.

The proposed epoxy encapsulation of the electronics has been tested against moisture absorption and its effects on conductivity. Tensile stresses confirm our approach of having the polyester yarn as supporting frame for the copper wires. Both, polyester yarn and copper wire, break at an elongation of about 20%. Assembled interposers slightly weaken the fabric.

The textile Bluetooth antennas have been designed for 'wireless personal area networks'. They are purely textile using a felt and a spacer fabric as dielectric and conductively plated fabrics for the antenna patch and ground plane. The Bluetooth specifications are satisfied even when the antennas are bent around a radius of  $37.5mm$ . The antennas are aimed as communication link between a wearable computer and infrastructure.

Eventually, we show how the woven fabric can be utilized as textile temperature sensor achieving an accuracy of 1 Kelvin.



# Zusammenfassung

Tragbare Computersysteme setzen eine angenehme und unauffällige Integration von Elektronik in Kleidung voraus, damit sie von den Anwendern akzeptiert werden. Ein *Textil-integrierter, drahtloser Temperatursensor* wird in dieser Dissertation als Anschauungsobjekt vorgestellt, welches die benötigten Technologien zur erfolgreichen Umsetzung aufzeigt. Diese neuartigen Technologien schlagen verschiedene Ansätze zur komfortablen Integration von elektronischen Komponenten in Kleidung vor. Zusammenfassend nennen wir diese Technologien *System-on-Textile* (SoT).

Die Dissertation konzentriert sich auf ein Polyester-Gewebe mit eingebetteten dünnen Kupferdrähten als Substrat für die Elektronik. Jeder Kupferdraht selbst ist mit einer dünnen Polymerlack-Schicht überzogen. Verschiedene elektrische Leitungsanordnungen werden mit diesem Substrat evaluiert betreffend elektrischer Eigenschaften. Der Frequenzgang der Leitungen verläuft flach bis zu einer Frequenz von etwa  $2\text{GHz}$ . Wir zeigen, dass die übliche  $50\Omega$  Leitungsimpedanz nicht erreicht werden kann. Die ermittelten Impedanzen liegen im Bereich von  $180 - 310\Omega$ .

Eine Verbindungstechnologie zum Aufbau beliebiger Verdrahtungsstrukturen mittels den Drähten im Gewebe wird vorgestellt. Diese Verbindungen beeinflussen die Signalübertragung nur unwesentlich. Im weiteren wird ein innovatives Interposer-Design zur Bestückung beliebiger Elektronikkomponenten auf Textil präsentiert. Ausserdem erörtern wir die zugehörigen Strategien und Beschränkungen für die Signal- und Speisungsverdrahtung innerhalb des Gewebes.

Die Feuchtigkeitsaufnahme der Epoxydharz-Kapselung der Elektronik wird getestet und die Isolationsfähigkeit überprüft. Zugversuche bestätigen unseren Ansatz eines Gewebes aus Polyester, welches die Kupferdrähte schützt. Die Polyesterfäden als auch die Kupferdrähte reißen bei einer Dehnung von über 20%. Auf das Gewebe aufgebrachte Interposer schwächen das Textil nur wenig.

Die textilen Bluetooth-Antennen sind für „wireless personal area networks“ ausgelegt. Die Bluetooth-Antennen bestehen gänzlich aus Textil: Filz und Abstandsgewirke für das Dielektrikum und leitend beschichtetes Textil für den Antennen-Patch und die Ground-Fläche. Die Bluetooth-

Spezifikationen werden erfüllt, selbst wenn die Antennen um eine Radius von  $37.5mm$  gebogen werden. Die Antennen werden zur Kommunikation zwischen tragbaren Computern und der Infrastruktur verwendet.

Schliesslich demonstrieren wir, wie das Gewebe als textiler Temperatursensor mit einer Genauigkeit von 1 Kelvin eingesetzt werden kann.

# 1

## Introduction\*

*Our vision of wearable computing is briefly presented in this chapter. We clarify our understanding on how electronic functionality can be integrated into clothing. Such a combination is called System-on-Textile. Miscellaneous other approaches and views of such systems are then discussed followed by an overview of existing conductive fabrics.*

---

\*partially based on [60]

## 1.1. Our vision of wearable computing

Wearable computing is a fast growing field in application-oriented research. Steadily progressing miniaturization in microelectronics along with advances in materials enable integration of functionality into clothing that allow entirely new applications. The vision of wearable computing describes future electronic systems as an integral part of our everyday clothing serving as intelligent personal assistants. According to Mann [66], a wearable computer is always on, does not restrict the user's activities and is aware of the user's situation. It features easy-to-use interfaces and supports the user unobtrusively with ad-hoc information.

Technology is not that far yet, however Venture Development Corporation (VDC) forecasted a world-wide market volume of \$556.3m for 'wearable computing' and \$47.4m for 'smart fabrics' in 2006. A possible definition of 'smart fabrics' could be: *fabrics that have been treated to fulfill specific functions in certain situations*. Such functions can be based for instance on physical or chemical reactions or on active components such electrical systems. Smart fabrics based on electrical systems are called 'electronic fabrics', 'e-fabrics' or 'e-textiles'. A selection of smart fabrics is shown in the list below.

- *Based on physical reaction:* gore membrane, lotus blossom effect, water repellence
- *Based on chemical reaction:* pesticide protection, flame retardance, antibacterial
- *Based on electrical system:* MP3 player jacket (by Interactive-Wear), textile keyboard (by Eleksen), textile pressure sensor and heating (by ITP GmbH), radiation protective clothing

Current annual growth rate for 'smart fabrics' and 'interactive textiles' (SFIT) is 19% (VDC). Obviously, the advantages of being assisted everywhere by wearable computing convince a growing number of people. Professor Yrjö Neuvo from Nokia concluded at the Ambience 2005 to the question what a market drives: "Everything what makes people slightly more convenient!".

The following chapters present technologies for an integration of electrical functions into clothing while maintaining wearing comfort. Such equipped clothing belongs to the category 'smart fabrics' and is called *System-on-Textile* (SoT). We do not aim to integrate large electronic devices into textiles, but rather small, dedicated electrical circuits such as sensors including

their signal conditioning components. By directly embedding into clothing, the sensors can be placed at positions where they can fulfill their sensing task in an optimal way, e.g. accelerometers at joints. Furthermore, Gemperle *et al.* give a good introduction where to place rigid components with only minor influence on wearability [38].

In contrast, chips with several hundreds of pads and high power dissipation such as high-speed microcontrollers are advantageously placed into rigid enclosures, e.g. accessories and belt buckles. There, circuits benefit from the properties of PCB technology such as high-density wiring, multilayer and precisely controlled impedances.

Figure 1.1 shows the partition of a wearable system into textile-embedded and accessory-embedded components and identifies the ingredients of an SoT from a technological point of view.

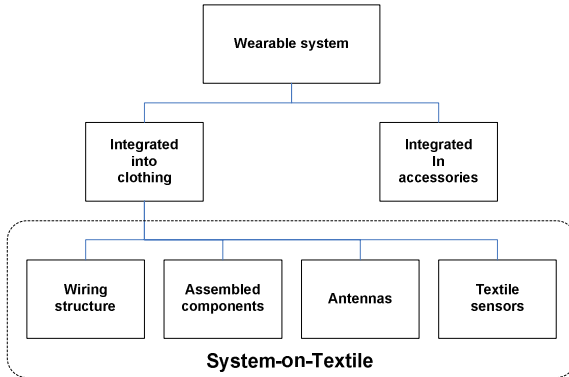


**Figure 1.1:** *Partitioning of a wearable system from a technological point of view*

In our opinion, wearing comfort is a key factor for user acceptance of wearable computing. We are convinced that this goal can only be achieved when textiles and textile-like materials adopt electrical functionality. In this dissertation, fabric sensors, fabric antennas and an integration technology for a smooth embedding of electrical components into fabrics have been investigated. Note that these technologies are not limited to clothing, but they can be applied to any system that utilizes fabrics such as car interior, curtains and seats.

## 1.2. Miscellaneous approaches to integrate electronics into fabrics

There exists no standard definition for wearable computing and electronic textiles. Thus, people have different views what integration of electronics into fabrics means. Some regard the fabric just as carrier for electronic device while interconnecting them with standard cables. Others try to integrate electronic functionality in an unobtrusive and comfortable way. Table 1.1 gives an overview of existing integration approaches grouped by the method that enables electrical connectivity.

**Table 1.1:** *Potential approaches for integration of electronics into fabrics*

Method	Institution	Project	Reference	Start
Sewing & Embroidery	MIT	E-Broidery	[76]	1998
	IZM Berlin		[49, 55]	
	TITV Greiz		[40]	
	Ghent University		[24]	
Weaving	GeorgiaTech	Wearable Motherboard	[74]	1998
	Virginia Tech		[47]	2002
	Interactive-Wear	MP3	[48]	
	TITV Greiz		[40]	
	NC State	Electrotextile	[28]	2001
	ETH Zurich		Chap. 3	2001
Printing	NTC, NC State		[70]	2005
	Dow Corning		[16]	2004
	ETH Zurich		Chap. 3	2004
Other methods	MIT	MIThril	[27]	2001
	ETH Zurich	WearArm	[65]	2001
	ETH Zurich	QBIC	[10]	2003
	Virginia Tech	e-TAGS	[54]	2003

### Sewing & Embroidery

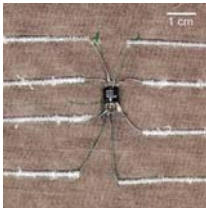
An early attempt to integrate electronics into fabrics is the *E-broidery* project. Post *et al.* [76] use embroidery of conductive yarn to interconnect and directly attach electronic components to textiles as shown in Figure 1.2(a). They discuss different types of conductive yarn, though all of them have resistances in the range of  $100\Omega/m$ . The paper also mentions a woven metallic silk organza



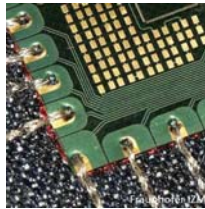
with conductive threads in weft direction. Connections in warp direction are established with separately soldered copper wires. Post *et al.* already identify the critical problems of electronic fabrics such as preservation of wearing comfort and washability.

IZM Berlin and TITV Greiz apply similar methods [40, 49]. They mount flexible PCBs on a fabric and sew metal plated multifilament yarn as interconnection between PCBs. This method is illustrated in Figure 1.2(b). IZM finally encapsulates the electronics with epoxy resins. With this technology, crossing of plated yarns seems to be difficult since they do not have an insulation coating.

Ghent University's research focuses on textile and textile-embedded sensors [24]. Electrically conductive thread is sewed to interconnect the sensors and to build RF<sup>1</sup> coils for wireless signal transmission (Figure 1.2(c)).



(a) E-Broidery Project, MIT [76]



(b) IZM Berlin [49]



(c) Ghent University [24]

**Figure 1.2:** Sewing Approaches

## Weaving

A bulky approach of electronic integration is the *Wearable Motherboard* from GeorgiaTech [74] (Figure 1.3(a)). There, rigid PCBs of size  $5 \times 5 \text{ cm}^2$  are attached to a woven shirt and are interconnected over an embedded bus structure consisting of electrical and optical fibers.

A woven fabric with embedded four wire bus forms the carrier for electronics in Virginia Tech's approach [47] as depicted in Figure 1.3(b). The wires have a diameter of about  $1 \text{ mm}$ . Since they are rather stiff, small PCBs can directly be soldered onto this bus. However, the electronic is exposed and no mechanical protection exists.

The Wearable Computing Lab of Infineon Technologies, now Interactive-Wear, already utilizes a technology for a comfortable embedding of electron-

<sup>1</sup>Radio Frequency

ics into jackets [48]. They provide a centralized electronic box of size of a cell phone and textile cables for interconnecting textile buttons and actuators (Figure 1.3(c)).

Gimpel *et al.* from TITV Greiz [40] use a woven fabric with embedded conductive threads. The plated multifilament thread features a resistance in the range of  $20\Omega/m$ . They mount electronic components directly onto the fabric as depicted in Figure 1.3(d).

Dhawan *et al.* from NC State [28] work with a woven fabric with conductive multifilament yarn as well. They apply welding and cutting to interconnect electronics as schematically depicted in Figure 1.3(e).

This dissertation focuses on a woven fabric by Sefar Inc. with embedded copper wires (Figure 1.3(f)). Each copper wire possesses a polymer coating and an electrical resistance of about  $18\Omega/m$ . Electrical connects are established by removing the wire coating and joining the wires. This technology to implement circuits on a fabric is described in Chapter 3.



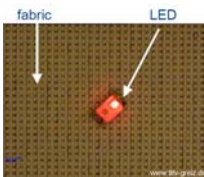
(a) Wearable Motherboard, GeorgiaTech [74]



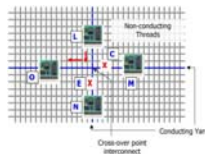
(b) Virginia Tech [47]



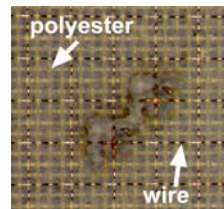
(c) Interactive-Wear [48]



(d) TITV Greiz [40]



(e) NC State [28]



(f) ETH Zurich

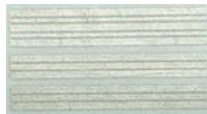
**Figure 1.3: Weaving Approaches**

## Printing

Merritt *et al.* [70] have screen-printed conductive structures on non-woven textiles as shown in Figure 1.4(a). They have measured variants of transmission lines and specified their electrical parameters such as DC resistance and line impedance before and after washing.

Berry *et al.* from Dow Corning mainly demonstrate printed RFID coils as application of their conductive ink [16]. They have performed several mechanical stress tests such as cyclic bending around a specified radius.

This dissertation also addresses screen-printed transmission line structures on woven fabrics as shown in Figure 1.4(b). They have been manufactured in collaboration with Sefar Inc. We analyze sheet resistance, line impedance as well as frequency response of these lines. The results are presented in Chapter 3.4. Additionally, we have performed several buckling tests on the printed structures.



(a) NTC, NC State [70]



(b) ETH Zurich

**Figure 1.4:** *Printing Approaches*

## Other methods

The *MITHril* project described by DeVaul *et al.* [27] is an early attempt to integrate electronics in clothing. Though they propose the vest for daily use, it is rather bulky and many cables and rigid components are attached to it (Figure 1.5(a)). Instead of an unobtrusive integration, the fabric just provides the mounting structure for the electronic devices.

The WearArm [65] is a wearable computer based on rigid and flexible PCBs that are placed in a textile bag as depicted in Figure 1.5(b). The head mounted display and the keyboard are connected with cables to the computer.

The QBIC project [10] is an attempt to integrate electronic functionality unobtrusively in accessories. The belt buckle contains the computer whereas the interfaces (USB, VGA) are fed to the belt.

Virginia Tech pursues in its approach a knitted fabric as carrier frame for attachment of several small PCBs calling them 'e-TAGS [54]. They are

electrically connected to the fabric with metal press buttons and ribbon cable connectors using insulated wires as seen in Figure 1.5(d).



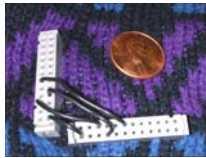
(a) MIThril, MIT [27]



(b) ETH Zurich, Wear-Arm [65]



(c) QBIC, ETH Zurich [54]



(d) Virginia Tech [54]

**Figure 1.5: Other Approaches**

### 1.3. Conductive fabric variants

Several approaches exist to establish electrical *wiring structures* (Figure 1.1) within electronic fabrics. This section presents an overview of established techniques that enable fabrics to conduct electrical current. Figure 1.6 shows a categorization of these techniques. 'Conductive fabrics' is split into two branches. The left branch lists fabrics whose conductive capability is embedded during manufacturing, e.g. weaving of metal wires. The right branch addresses fabrics that are not intrinsically conductive. Their conductivity is enabled after manufacturing (weaving, knitting, etc.) using an additional process.

A non-conductive fabric usually consists of polymer yarns such as polyester or polyamide whereas conductive components ideally utilize good conductors such as silver and copper.

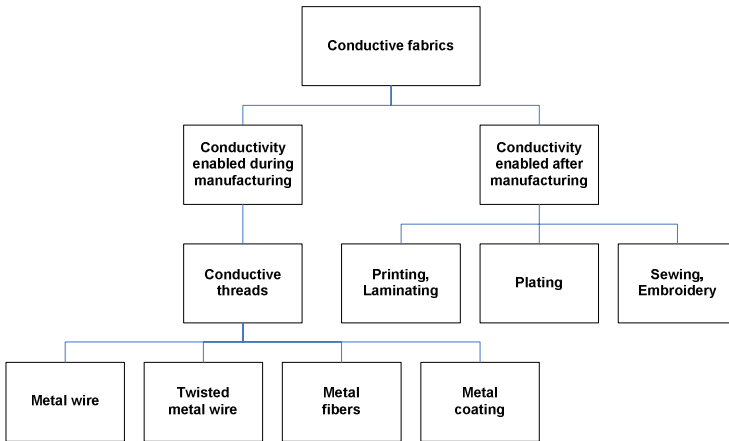


**Figure 1.6:** Techniques to enable conductivity in fabrics

### Conductive threads

The fabric is entirely or partially equipped with conductive threads. Polymer threads form a carrier frame, called substrate, for the conductive threads. In this kind of fabric, conductive layer and substrate are embedded into each other. Conductivity can be established with different thread types:

1. *Metal wire*: The thin metal wire is treated as separate thread. The fabric consists of alternating polymer thread and metal thread (see Figure 1.3(f)). The metal wire itself features an optional thin polymer coating as electrical insulation. This wire variant applied in a woven fabric provides a layer-like structure. The insulation coating prevents short-circuits between metal wires. These kinds of metal wires have originally been developed by Elektro-Feindraht AG, Switzerland [32] for clothing in shielding applications. Besides, their coatings are robust against washing abrasion.
2. *Twisted metal wire*: Similar to variant 1, but the metal wire is twisted around the polymer yarn. Therefore, yarn and metal wire can be handled as single entity (Figure 1.7(a)). The location of the wire is not as precisely known as in variant 1 due to its helical path.
3. *Metal fibers*: The conductive yarn consists of metal multifilaments [15]

or of metal staple yarn, e.g. stainless iron staples (Figure 1.7(b)). Staple yarn tends to fraying.

4. *Metal coating*: The polymer yarn (e.g. monofilament, multifilaments and staple yarn) is chemically coated with a thin metal layer (Figure 1.7(c)). Coating is limited to thicknesses of several hundred nanometers in order to preserve flexibility.

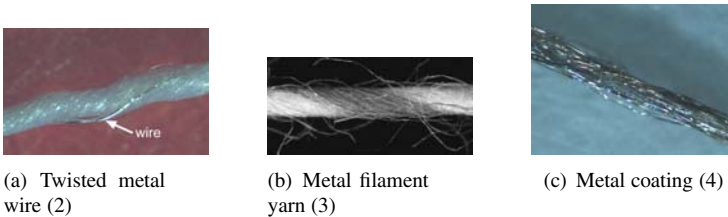


**Figure 1.7:** *Conductive yarns*

Using the 'conductive thread' approach, no additional step after manufacturing of the fabric is required to establish conductivity. The electrical resistance of these conductive threads lies in the range of  $10 - 500 \Omega/m$  [40, 55, 60].

As a side note, intrinsically conductive polymer threads still feature an electrical resistance of  $> 10k\Omega/m$  [26] and molecular instability. Therefore, they have not been considered in the listing above

### Printing, Laminating

A conductive structure is deposited (e.g. by ink-jet, screen-printing or laminating) on the non-conductive fabric (see Figure 1.4(b)). Printing of a conductive structure shows similar properties as plating and has a resistivity of  $0.6 - 1.4 \Omega mm^2/m$  ([70] and Section 3.4). Most conductive inks and pastes are based on silver filler and suffer from brittleness.

### Plating

The non-conductive fabric is chemically processed after manufacturing in order to deposit a metallic layer. After this process step, the entire surface of the fabric is conductive (Figure 1.8). Common values for the sheet resistance are  $0.05 - 1 \Omega/\square$  [87, 88].

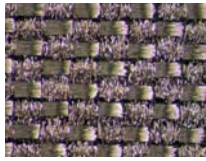


**Figure 1.8:** *Plating*

Plating is limited to sub-micron thicknesses in order to maintain typical textile properties. A larger thickness of the plating decreases the electrical resistance, but at the same time increases the probability of peeling. Several other factors compromise reliable low-ohmic conductance such as corrosion and oxidation of the fiber surface and process-dependent partially plated fibers.

### **Sewing, Embroidery**

The conductive structure is sewed with conductive threads on the non-conductive fabric as seen in Figure 1.2(b). Not a conductive layer that must be structured in a later step is added to the substrate, but the conductive structure itself. It can only be manufactured in a serial process, i.e. only one point-to-point connection at a time. A crossing of the bare threads seems impossible without short-circuit. Sewing using solid metal wires has proven to be unreliable for electrical connections [73]. The high mechanical stresses on the metal wires during sewing lead to broken wires.

## **1.4. Summary**

Depending on the application, each of the presented fabric variants has its advantages and its disadvantages. This dissertation focuses on a woven fabric with insulated copper wires (conductive yarn variant 1 in Figure 1.6). The fabric is called PETEX (Sefar Inc.) and is used to implement textile transmission lines and wiring structures for circuits on the fabric. The corresponding technologies are discussed in Chapter 3. Subsection 3.4 of Chapter 3 also addresses printed transmission lines.

Plated fabrics are deployed for textile Bluetooth patch antennas, which are introduced in Chapter 5.

Using these technologies, entire circuits can be replaced by fabrics composing a *System-on-Textile*. Inspired from PCB manufacturing, we call the

technology for electronic integration into fabrics *textile packaging* and the wiring of electronic components on fabrics *textile routing*.



# 2

## Motivation

*In this chapter, the key topics of this dissertation are identified. A proof-of-concept motivates the necessary technologies for a successful integration of electronic functionality into clothing. Each component is indicated and briefly discussed.*

## 2.1. Covered topics in the dissertation

In this dissertation, we address the topics of textile transmission lines, textile integrated circuits, textile antennas as well as textile temperature sensors. We focus on a woven fabric with embedded copper wire grid in the discussion of textile temperature sensors, transmission lines and textile integrated circuits. Our approach for integration of circuits in fabrics is illustrated in Figure 2.1. The wiring structure among circuit components are established by connecting the fabric embedded copper wires. Cuts must be placed at specific locations in the wiring in order to avoid short-circuits between copper wires.

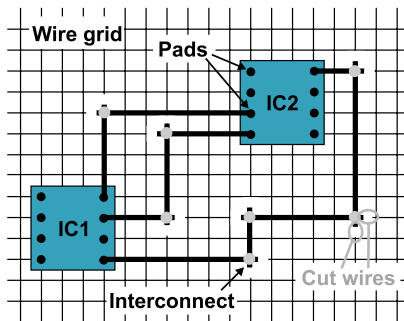


**Figure 2.1:** Approach to integrate circuits in a fabric with wire grid. Note that only the wire grid of the fabric is shown.

In this dissertation, we want to know how far we can advance using a fabric with embedded wire grid. We want to clarify the following questions:

- What impedances and bandwidths are achievable with transmission lines integrated in the fabric? (Chapter 3)
- What technologies are necessary to enable wiring structures in the fabric and how can arbitrary electrical components be assembled and routed? (Chapter 3)
- What rules apply for a textile routing structure? (Chapter 4)
- What accuracy can be obtained in the temperature measurement with the fabric? (Chapter 6)

Note that different fabrics are utilized for the textile antennas. The antennas are composed of conductively plated fabrics and non-conductive fabrics as dielectric. The following questions are discussed in Chapter 5:

- How do purely textile antennas perform?
- How does the antenna performance react on bending?
- Are standard simulation tools, e.g. Ansoft HFSS [11], suitable for the design of textile antennas?

The above-mentioned technologies identify the necessary ingredients for a System-on-Textile (SoT).

## **2.2. Proof-of-concept**

The developed technologies and the obtained knowledge are demonstrated in a proof-of-concept. The proof-of-concept application is a Fabric Integrated Wireless Temperature Sensor. It combines textile temperature sensor, textile integrated circuits, textile transmission line and textile antennas in a single application.

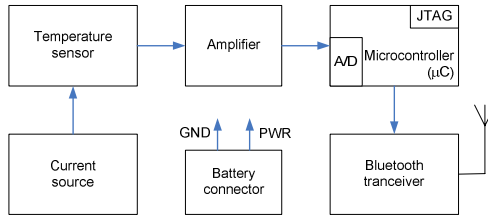
### **2.2.1. Block diagram of the Fabric Integrated Wireless Temperature Sensor**

Figure 2.2 shows the block diagram of the Fabric Integrated Wireless Temperature Sensor. It consists of the textile temperature sensor as input. The electrical components are assembled on the fabric with embedded wire grid and are interconnected over these wires. The antenna feed line consists of a CPW-like textile transmission line. The antenna is purely textile and satisfies Bluetooth specifications.

The Fabric Integrated Wireless Temperature Sensor measures the temperature and transmits the value wirelessly over Bluetooth to a host. The host can be a PC that displays the measured temperature.

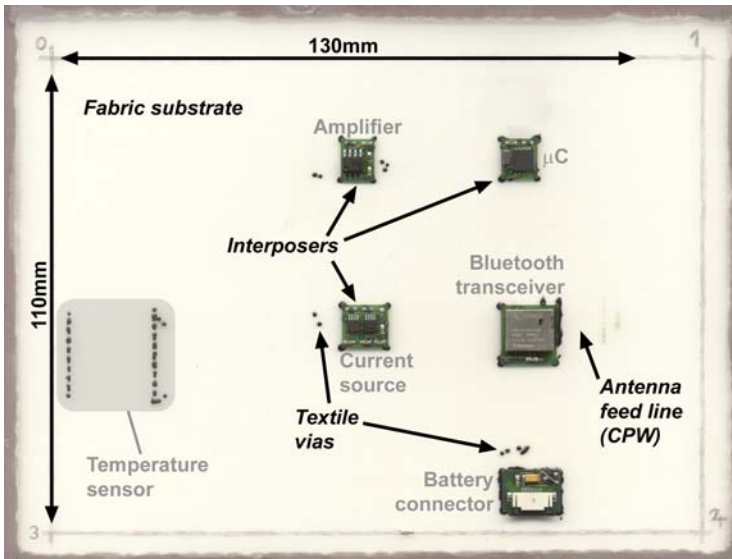
### **2.2.2. Implementation of the Fabric Integrated Wireless Temperature Sensor**

Figure 2.3 illustrates how the Fabric Integrated Wireless Temperature Sensor is actually distributed on the fabric. Some expressions indicated in italics might not be understood by the reader yet. However, the remarks in Chapter 3 clarifies all of these expressions.



**Figure 2.2:** *Block diagram of the Fabric Integrated Wireless Temperature Sensor*

The microcontroller [93] is programmed over the JTAG<sup>1</sup> connector. This connector can be truncated at the narrowed location after finishing programming (see Figure 2.3).



**Figure 2.3:** *Proof-of-Concept - The distribution of the electronic components for the temperature sensor on the fabric*

<sup>1</sup>Joint Test Action Group

Table 2.1 lists some statistics to the wire usage, the number of cuts and the number of textile vias used in the fabric substrate of the Fabric Integrated Wireless Temperature Sensor.

**Table 2.1:** *Statistics to the Fabric Integrated Wireless Temperature Sensor*

Item	#
Textile vias	96
- Vias in sensor element	34
- Vias for antenna feed	43
Wire cuts	67
Utilized wires in total	90
- Wires for antenna feed	19
- Wires in sensor	20

Table 2.2 shows the number of pads and components of each interposer utilized in the Fabric Integrated Wireless Temperature Sensor.

**Table 2.2:** *Statistics to utilized interposers*

Interposer	# of pads to fabric	# of components on interposer
Current source	7	9
Amplifier	7	4
$\mu C$	14	4
Bluetooth transceiver	18	2
Battery connector	10	4
Total	60	23

### 2.2.3. Outline to the chapters

The temperature sensor with an area of  $2x2cm^2$  entirely consists of fabric material featuring a temperature range from  $0^{\circ}C$  to  $60^{\circ}C$ . Chapter 6 explains the principle and realization of this sensor.

The CPW-like feed line structure achieves a low line impedance such that the mismatch between the  $50\Omega$  output of the Bluetooth RF electronic and the feed line is acceptable. Chapter 3 discusses different textile transmission line variants.

The electrical components and Bluetooth transmission circuit [44] cannot be made of textiles. However, the substrate for assembly of these electronic components can be textile. In Chapter 3, technologies will be presented for textile transmission lines, textile interconnects and component assembly on textiles.

Chapter 4 explains how electronic circuits need to be arranged on a textile substrate in order to maintain drapability while ensuring electrical function.

The antenna can purely consist of textiles. Chapter 5 describes different variants of textile patch antennas and their behavior under bent conditions. The antenna itself is not shown in Figure 2.3, though its feed line.

# 3

## Integration Technologies\*

*This chapter discusses the technologies needed to embed electronic circuits into fabrics. In the first sections, a woven fabric with embedded copper wires is introduced as substrate for System-on-Textile. Different textile transmission lines are characterized in detail. Signals up to 2GHz can be transmitted using the proposed substrate. Additionally, transmission lines printed on fabrics are investigated in a short section.*

*The second part of the chapter explains interconnect technologies for arbitrary routing structures within the fabric as well as for component assembly onto the fabric. The interconnects are electrically specified by scattering parameters. Eventually, a possible protection for the electronics on the fabric is presented along with its mechanical tensile strength and its behavior in moisture.*

---

\*partially based on [59, 60]

### 3.1. Introduction

In this chapter, technologies to integrate electronics into fabrics are described. The implementation of textile transmission lines is a fundamental step towards this goal. A brief introduction to transmission line theory is given in Appendix A along with a new approach to filter out perturbations in the measurements of the substrate's permittivity.

First, we identify a woven fabric with embedded copper wires as substrate for electrical circuits. We analyze the fabric regarding geometrical tolerances and characterize the electrical parameters of different transmission lines variants within the fabric.

Second, similar investigations are performed with a woven acryl-cotton fabric and printed transmission lines.

Based on the fabric with embedded copper wires, an interconnect technology is presented in order to establish arbitrary wiring structures. A novel interposer technology allows assembly of arbitrary components and chip packages on the fabric. These two key technologies enable the implementation of electrical circuits on the fabric.

#### 3.1.1. Related Work

Cottet et al. [25] have studied the performance of textile transmission lines regarding DC resistance, line impedance, frequency response and permittivity. They have applied different variants of fabric version 0 (Figure 3.1(a)) for their transmission lines.

Dhawan et al. [29] have focused on far-end and near-end crosstalk within a fabric with conductive multifilament threads. Their results are valid for a specific measurement setup. Such measurements are not discussed in this dissertation.

### 3.2. Textile substrates with embedded copper wires

#### 3.2.1. Fabric versions 0-3

Five iterations of woven fabrics with embedded copper wires in warp and weft direction have been processed until the final fabric version 4 (PETEX) shown in Figure 3.2 has been achieved. All fabrics have been fabricated by Sefar Inc., except version 0. In the following paragraphs, the different fabric versions are briefly discussed.

Version 0, shown in Figure 3.1(a), utilizes a multifilament polyester yarn. The copper wire is twisted around the yarn. Apart from yarn pitch variations



in the range of  $150\mu m$  [25], the copper wire locations are not precisely defined within the fabric because of their helical path around the yarn. The DC resistance of a wire in the fabric features about  $17.8\Omega/m$  [25].

Figure 3.1(b) depicts version 1 of the multifilament fabric. It can be seen that the copper wire pitch differs for warp and weft. This irregularity results in unequal line impedances of transmission lines in warp and weft direction. Additionally, no polyester yarn is woven into the fabric in weft direction. Mechanical loads in weft direction must therefore be absorbed by the copper wires.

In version 2, the copper wire and the multifilament yarn are woven concurrently in the weft. As a result, the copper wires are not precisely aligned to each other as can be seen in Figure 3.1(c).

Fabric version 3 exists in variants with wires in the weft direction only and with wires in both directions. The fabric already shows a high precision according to Figure 3.1(d). However, the differences in the mechanical properties of multifilament yarn and copper wire result in an unreliable manufacturing process where copper wires tend to break. Furthermore, the fabric with its weight of  $151g/m^2$  is rather heavy. Fabric version 2 and 3 have a similar DC resistance of  $14.5\Omega/m$  per wire.

### 3.2.2. Fabric version 4, PETEX

The final version 4 is a hybrid fabric called PETEX shown in Figure 3.2. It consists of woven polyester monofilament yarn (PET) with diameter  $42\mu m$  and copper alloy wires with diameter  $50 \pm 8\mu m$  (AWG46<sup>1</sup>). Each copper wire itself is coating with a polyurethane varnish as electrical insulation. The copper wire grid in the textile features a spacing of  $570\mu m$  (mesh count in warp and in weft is  $17.5cm^{-1}$ ). The combination of PET yarn and copper wires requires a special weaving technology, which includes two yarn systems in warp and weft direction (3 PET wires and 1 copper wire) with separate tensioning systems. The wires in warp and weft have undergone different thermal treatment in advance. Therefore, different mechanical properties are achieved in the two directions. The wires in warp direction possess a higher tensile strength compared to the wires in weft direction. These differences support a reliable manufacturing process and minimize breakage. The PET yarn has similar tensile strengths in both directions.

The DC resistance of the wire in warp direction is about  $15.7\Omega/m$  whereas the wire resistance has  $17.2\Omega/m$  in weft direction. This difference is caused by different tensions in warp and weft during the manufacturing pro-

---

<sup>1</sup>American Wire Gauge

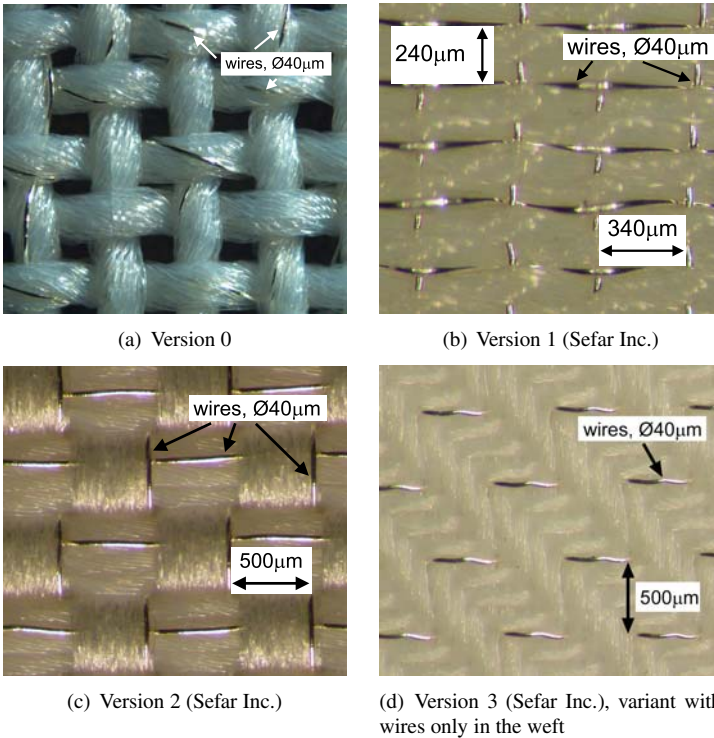
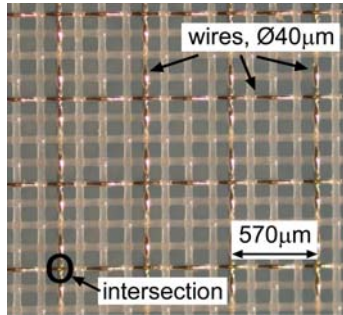


**Figure 3.1:** Iterative steps towards the PETEX hybrid fabric

cess. Considering the pitch of  $570\mu m$ , the wire resistance can be translated in a sheet resistance of  $8.95m\Omega/\square$  and  $9.8m\Omega/\square$ , respectively. As comparison, the straight copper wire possesses a DC resistance of  $13.82\Omega/m$  and a copper laminated PCB of 1 ounce ( $35\mu m$ ) has a sheet resistance of  $0.49m\Omega/\square$ .

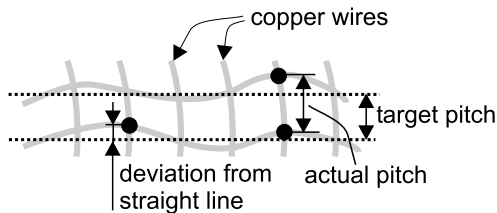
PETEX features a thickness of  $90\mu m$ , a mesh opening of  $95 \pm 10\mu m$ , an opening area of 44% and a weight of  $74g/m^2$ . The fabric represents a compromise between preserving textile properties and copper wire density.

The copper wires within PETEX deviate from straight lines and the copper wire pitches vary over the length. Thus, the positions of the wire intersections indicated in Figure 3.2 vary as well. For the deployment as substrate for SoT, the locations of these intersections must be known in order to connect the proper wires (see Section 3.5). Figure 3.3 illustrates the stated problem



**Figure 3.2:** PETEX hybrid fabric (Sefar Inc.)

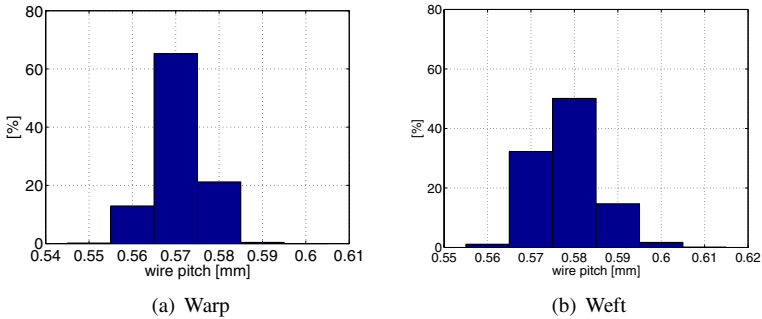
and how the actual wire pitches and the deviations from a straight line are obtained. Each intersection of wires is tracked in advance and the actual wire pitches are then determined. Linear regression is applied to derive the deviation of the wires from straight lines.



**Figure 3.3:** Determination of wire pitch and line variation within PETEX

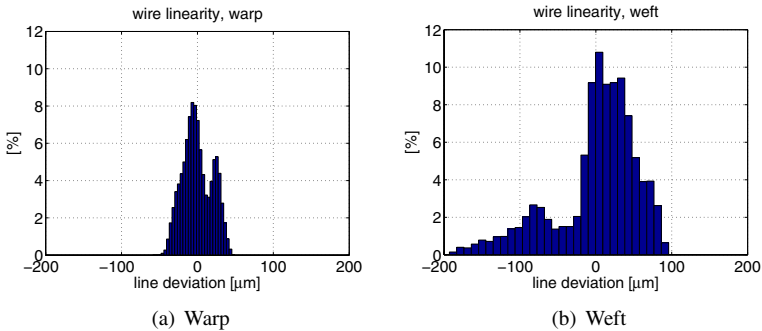
Figure 3.4 shows the wire pitch distribution in warp and weft direction by observing over 50,000 wire intersections. Whereas the distribution in warp direction is centered around the intended pitch of  $0.57\text{mm}$ , the distribution in weft direction is shifted to the right by about  $10\mu\text{m}$ . Both histograms follow a Gaussian distribution. The standard deviations in warp and weft direction are  $\sigma_{warp} = 6.1\mu\text{m}$  and  $\sigma_{weft} = 8.0\mu\text{m}$ , respectively. Details to the applied tracking method of the wire intersections are described in the second approach of Appendix C.3.

In addition, the deviation of the copper wires from straight lines is shown in Figure 3.5 for warp and weft direction. Again, the warp direction reveals a better result than the weft direction. The standard deviations are



**Figure 3.4:** *Copper wire pitch distribution in warp and weft direction within PETEX*

$\sigma_{warp} = 19.5\mu m$  and  $\sigma_{weft} = 55.5\mu m$ , respectively. Notice that stretch within the fabric affects these values. These figures change when using different stretches. The smaller the standard deviation is, the more uniform is the stretch in the fabric.



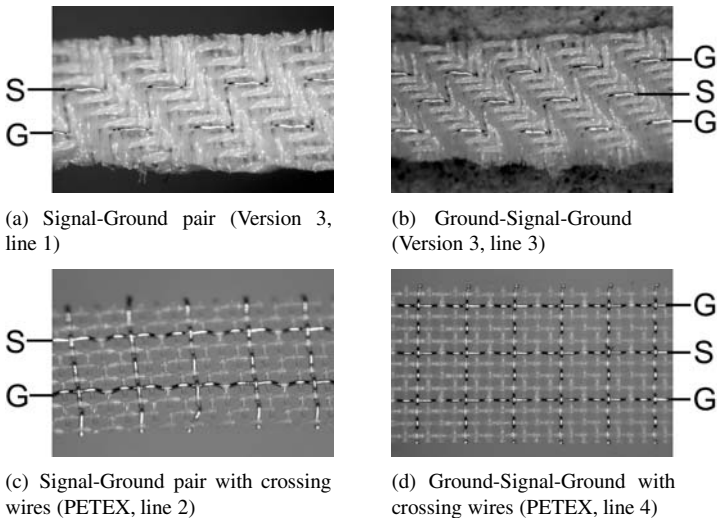
**Figure 3.5:** *Copper wire line deviation in PETEX*

Figure 3.6 presents SEM<sup>2</sup> images of fabric version 0 and the final PETEX. The difference between monofilaments and multifilament can clearly be seen. PETEX's copper wires are directly accessible whereas the wires in fabric version 0 are occluded by the polyester fibers.

<sup>2</sup>Scanning Electron Microscopy



Instead, wire pair (wp) and triple wire (tw) configurations are investigated using fabric substrates with copper wire in one direction (version 3) and in both directions (PETEX). In order to avoid parasitic coupling with surrounding floating wires, the substrate is cropped that only the required wires remain as can be seen in Figure 3.7. Further, a CPW-like structure with one signal wire surrounded by 15 ground wires on each side is analyzed. Eventually, the wire pair and triple wire transmission lines with surrounding floating wires are presented for completion. Table 3.1 gives an overview of the transmission lines analyzed.



**Figure 3.7:** Configurations of wire pair transmission lines with fabric versions 3 and PETEX

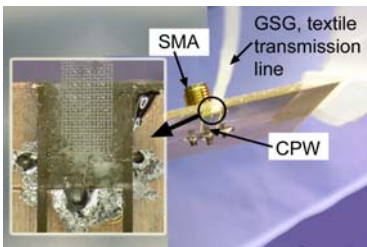
In order to connect the lines to the measurement equipment, PCB adapters with SMA connectors have been manufactured. A  $50\Omega$  CPW adapter shown in Figure 3.8(a) is utilized for triple wires and CPW-like lines whereas a  $50\Omega$  microstrip line adapter is used for wire pairs (Figure 3.8(b)).

### 3.3.2. Electrical measurement results

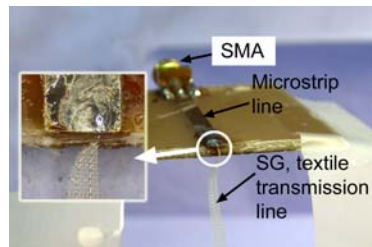
This subsection presents the measurement results of the transmission line configurations listed in Table 3.1. The textile transmission lines are kept under slight strain in order to straighten the fabric during the measurements.

**Table 3.1:** Transmission line variants; SG=signal-ground wire pair, GSG=ground-signal-ground triple wire, ..GGSGG..=CPW-like structure

Line #	Wire Configuration	Substrate	Floating wires in parallel	Lengths [mm]
1.	SG (wp)	V3	-	34.5 / 149.5
2.	SG (wp)	PETEX	-	31.0 / 149.5
3.	GSG (tw)	V3	-	34.5 / 149.5
4.	GSG (tw)	PETEX	-	31.0 / 149.5
5.	SG (wp)	V3	✓	34.5 / 149.5
6.	SG (wp)	PETEX	✓	31.0 / 149.5
7.	GSG (tw)	V3	✓	46.0 / 149.5
8.	GSG (tw)	PETEX	✓	133 / 196.0
9.	..GGSGG..	V3	-	129 / 200.0
10.	..GGSGG..	PETEX	-	131 / 196.0



(a) CPW adapter for triple wire configuration



(b) Microstrip line adapter for wire pair configuration

**Figure 3.8:** PCB adapters connecting from SMA to fabric transmission line

Secondly, the transmission lines are surrounded by air with at least 15cm distance to the next solid object. The measurements are performed at room temperature using the equipment listed in Table 3.2.

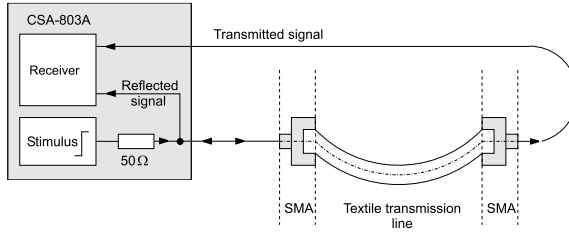
### Line impedance $Z_0$

The line impedances have been obtained by using TDR/TDT [92] measurements. The corresponding measurement setup is depicted in Figure 3.9.

The obtained curves in Figure 3.10(a) show that signal-ground (SG) and ground-signal-ground (GSG) configuration lead to line impedances far above

**Table 3.2:** *Measurement equipment*

Measurement	Principle	Equipment	Manual
$Z_0$	TDR/TDT	Tektronix CSA-803A IPA-501 software	[91] [92]
BW	s-parameter	HP VNA 8753E	[7]
eff. $\epsilon_r$	s-parameter	HP VNA 8753E	[7]

**Figure 3.9:** *Measurement setup for TDR/TDT measurements of textile transmission lines*

the usual  $50\Omega$ . The  $50\Omega$  line impedance cannot be achieved with common fabric substrates since a permittivity of about  $\epsilon_r = 60$  is required. As expected, a GSG configuration lowers the impedance compared to a SG configuration. All impedances range between  $180\Omega$  and  $300\Omega$ . Though the wire pitch is larger in PETEX, it reveals lower impedances by about  $50\Omega$ . This behavior seems to be because of the crossing wires. Additionally, the wires runs undulated within the fabrics due to the weaving process. Adjacent wires are shifted against each other in fabric version 3 (see Figure 3.7(b)). By assuming a sinusoidal shape of the wires, two adjacent wires propagate with  $180^\circ$  phase shift. As a result, the mean distance between the wires is about  $0.6\text{mm}$  as compared to the wire pitch of  $0.5\text{mm}$ . This fact leads as well to higher impedance. In contrast, the wires in PETEX propagate 'in phase'.

Figure 3.10(b) depicts measurements of the same transmission line configurations as in Figure 3.10(a), but with adjacent floating wires in parallel within the fabric. Coupling with the floating wires lowers the line impedances of GSG transmission lines by about  $10\Omega$ . On the other hand, the impedance of the PETEX SG configuration rises by about  $15\Omega$  when measured within the fabric. Secondly, the cross-running wires within PETEX smooth the measurement of impedance curves by cutting off parasitic modes. These findings



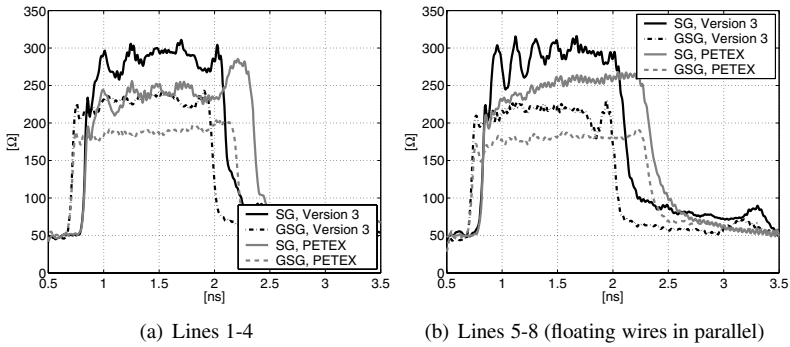


**Figure 3.10:** Measured characteristic impedances of wire transmission lines determined by TDR/TDT (Table 3.1). The time scale of the x-axis directly corresponds to the position on the textile transmission line.

generally agree with the results by Cottet *et al.* [25].

Figure 3.11 shows the measurements of the CPW-like transmission line configuration (lines 9+10). This configuration reveals about the same line impedance as the GSG configurations.

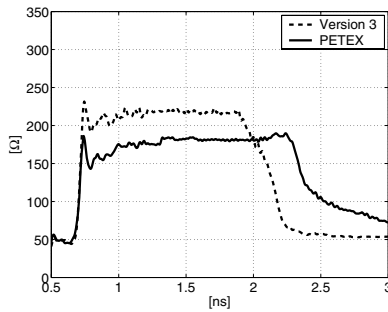


**Figure 3.11:** Measured characteristic impedances of wire transmission lines 9-10 (CPW) determined by TDR/TDT (Table 3.1). The time scale of the x-axis directly corresponds to the position on the textile transmission line.

Notice that an ideal CPW sketched in Figure 3.12 features a line impedance of  $220\Omega$  assuming  $w = 40\mu\text{m}$ ,  $s = 0.53\text{mm}$ ,  $h = 90\mu\text{m}$  and a conductive layer thickness of  $t = 40\mu\text{m}$ . These values are directly derived

from the PETEX fabric geometry. The exact relative permittivity  $\epsilon_r$  is not critical since the impedance  $Z_0$  ranges only from  $210 - 224\Omega$  for  $\epsilon_r = 1..3$  (air..PET). Similar values for  $Z_0$  have been derived using the specifications of fabric version 3. The formulas to compute  $\epsilon_{eff}$  and  $Z_0$  of a CPW as in Figure 3.12 are given in (3.1).  $K(\cdot)$  denotes the elliptic integral.



**Figure 3.12:** Cross section of a CPW

$$\epsilon_{eff} = 1 + \frac{\epsilon_r - 1}{2} \frac{K(k_1)K(k'_0)}{K(k'_1)K(k_0)}$$

$$k_0 = \frac{w}{w+2s} \quad k_1 = \frac{\sinh(\pi w/4h)}{\sinh(\pi \frac{w+2s}{4h})} \quad k'_x = \sqrt{1 - k_x^2} \quad (3.1)$$

$$Z_0 = \frac{30\pi}{\sqrt{\epsilon_{eff}}} \frac{K(k'_0)}{K(k_0)}$$

Comparing the measurement results in Figure 3.11 with the CPW model as approximation for a CPW-like transmission line reveals a reasonable model fit for fabric version 3. The crossing wires of PETEX lower the line impedance significantly and the CPW model assumption fails.

### Frequency response

The HP VNA is utilized to measure the scattering parameters of the textile transmission lines. The corresponding frequency response is then extracted according to the principle described in Section A.2. We use the same measurement setup as for TDR/TDT measurements shown in Figure 3.9, but replace the CSA-803A with the HP VNA.

Figures 3.13, 3.14 and 3.15 depict the frequency response of the transmission line configurations listed in Table 3.1. The attenuation of the transmission lines is normalized to  $1cm$  length.

For the following discussion, we define the *bandwidth*  $BW$  as range from  $0Hz$  until the first occurring notch below  $-0.5dB/cm$  in the frequency response.

The transmission line variants feature bandwidths from  $1.8 - 6GHz$ . The bandwidth of line 4 (GSG, PETEX) actually exceeds the measurement range of  $6GHz$  as can be seen in Figure 3.14(b). It is obvious from the figures that

the parallel floating wires do not affect the performance at frequencies lower than  $200\text{MHz}$ . The bandwidth of transmission lines 5-7 even indicate only small deterioration due to the floating lines until  $2\text{GHz}$ . However, parasitic modes due to coupling with the floating wires and reflections increasingly disturb signal transmission above  $2\text{GHz}$  for line configurations 5-7 and above  $200\text{MHz}$  for line configuration 8. Thus, transmission line bandwidths are mainly limited by these effects [25, 58] but by ohmic losses. These effects can be seen best in Figure 3.14(b) for the PETEX triple wire and in Figure 3.15 for the CPW-like structures. Secondly, PETEX delivers noisier results than fabric version 3 due to the crossing wires. The CPW-like structure shows worst results because of the many parallel ground line introducing the odd modes.

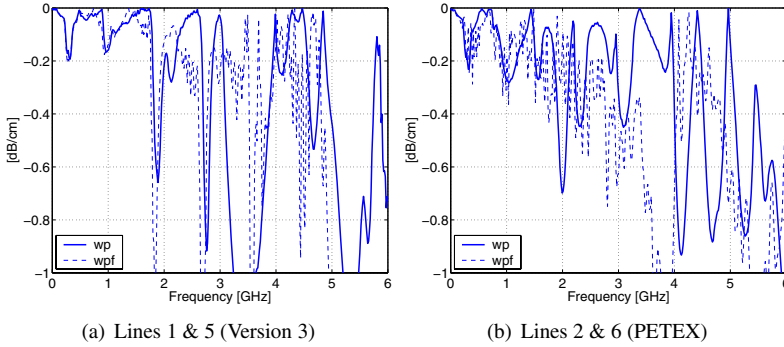


**Figure 3.13:** Frequency response of wire pairs;  $wp$ =single wire pair,  $wpf$ =wire pair with floating wires in parallel (Table 3.1)

### Relative effective permittivity $\epsilon_r$

The relative effective permittivity is obtained from scattering parameter measurements as well. A method to determine  $\epsilon_r$  is explained in Section A.2 along with a smoothing algorithm for  $\epsilon_r$ . The smoothing is a crucial tool to suppress measurement disturbances and to achieve a flat permittivity curve over the frequency range. The disturbances are caused by odd modes and resonances in the transmission line. The resonances and odd modes occur in turn due to floating wires in the fabric, unequal lengths of the ground and signal wires in the transmission line configuration, the wavy wire shape within the woven fabric as well as due to geometrical tolerances in general. These effects

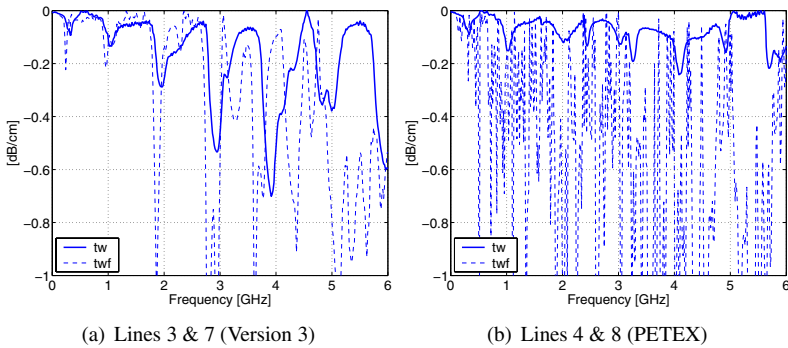


**Figure 3.14:** Frequency response of triple wires; *tw*=single triple wire, *twf*=triple wire with floating wires in parallel (Table 3.1)

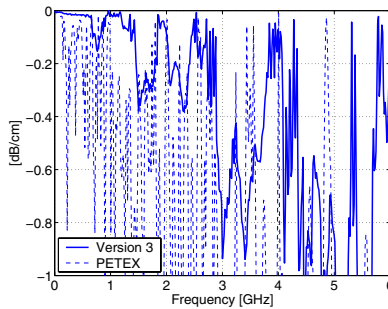


**Figure 3.15:** Frequency response of CPW-like structures (lines 9+10 in Table 3.1)

have already been mentioned by Cottet *et al.* [25].

Figures 3.16, 3.17 and 3.18 show the permittivity of the transmission line configurations listed in Table 3.1. The extracted permittivities over all transmission line configurations show similar values,  $\epsilon_r = 1.65 - 1.75$  for fabric version 3 and  $\epsilon_r = 2.0 - 2.45$  for PETEX.

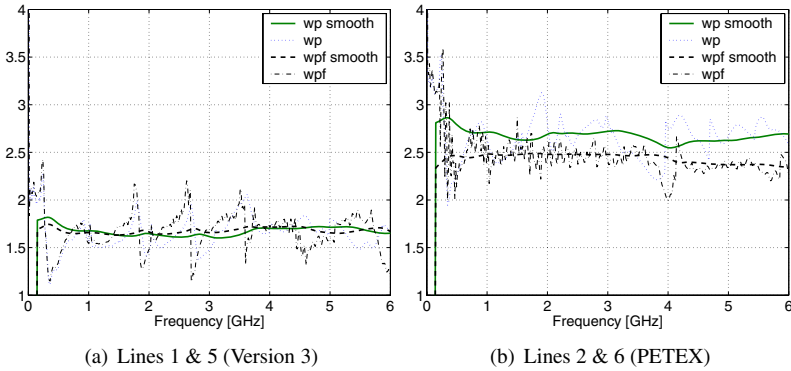


**Figure 3.16:** Extracted relative effective permittivity  $\epsilon_r$  of wire pairs;  $wp$ =single wire pair,  $wfp$ =wire pair surrounded by floating wires (Table 3.1)

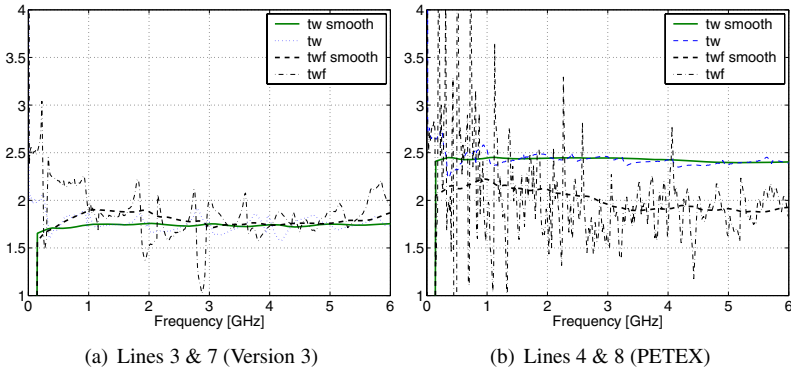


**Figure 3.17:** Extracted relative effective permittivity  $\epsilon_r$  of triple wires;  $tw$ =single triple wire,  $twf$ =triple wire surrounded by floating wires (Table 3.1)

### Comparison and conclusion

The line impedance values  $Z_0$  determined by TDR/TDT measurements are verified with the VNA measurements in Table 3.3.  $Z_0$  can be computed using Formula (3.2) given by Ball [14]. This formula is valid for line impedance computations of symmetrical wire line configurations whereby the extracted

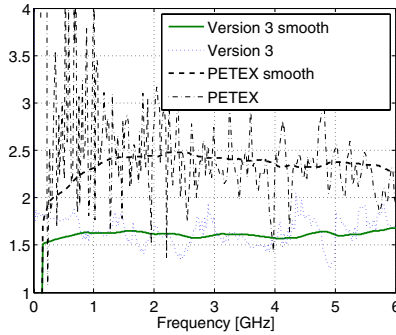


**Figure 3.18:** *Extracted relative effective permittivity  $\epsilon_r$  of CPWs (line 9+10 in Table 3.1)*

permittivities of the VNA measurements are plugged-in. The two measurement methods agree well within a tolerance of about 5% for PETEX and about 10% for fabric version 3. The CPW-like and the GSG configuration in PETEX are exceptions.

As illustrated in Table 3.3, textile wire pairs and triple wires can be approximated with the standard formula for straight wires (Formula (3.2)) despite of the wavy wire shape. This approximation performs more accurate for the PETEX fabric.

Additionally, HFSS simulations [11] have been conducted to determine the impedance  $Z_{air}$  of the PETEX transmission lines. The simulation model consists of a grid with straight copper wires with no polyester fibers in-between. Thus, the dielectric is air. An example of such a simulation model is depicted in Figure 3.19. The values listed in Table 3.3 have been obtained by using  $Z_0 = Z_{air}/\sqrt{\epsilon_r}$  with  $\epsilon_r$  from the VNA measurements. The results agree within 5% for wire pair configuration and within 15% for triple wire configuration.

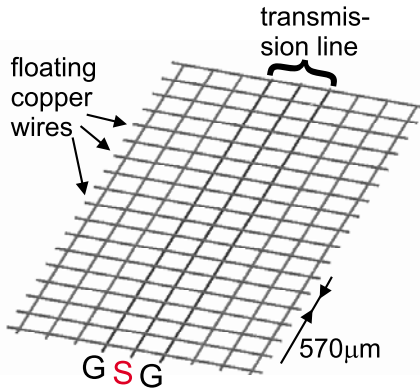
The bandwidths of the transmission lines determined by the frequency response are listed in Table 3.3 as well.

$$Z_0 = \frac{1}{2\pi} \sqrt{\frac{\mu_0}{\epsilon_0 \epsilon_r}} \left\{ \ln\left(\frac{d}{r}\right) + \frac{1}{n} \ln\left(\frac{d}{nr}\right) \right\}, \quad \begin{array}{l} n: \# \text{ of ground lines} \\ d: \text{ distance between wires} \\ r: \text{ wire radius} \end{array} \quad (3.2)$$

The following conclusions can be drawn from the different textile trans-

**Table 3.3:** Comparison of textile transmission line impedances obtained by different methods and transmission line bandwidths

Line #	Config.	Measurement Method			HFSS $Z_0$ [ $\Omega$ ]	BW [GHz]
		TDR/TDT $Z_0$ [ $\Omega$ ]	VNA $Z_0$ [ $\Omega$ ]	VNA $\epsilon_r$ [-]		
1	wp	295	313	1.7	-	1.8
2	wp	245	244	2.7	254	2.0
3	tw	235	216	1.75	-	2.9
4	tw	185	179	2.45	159	>6.0
5	wpf	295	313	1.7	-	1.8
6	wpf	260	257	2.45	260	2.2
7	twf	225	216	1.75	-	1.8
8	twf	180	198	2.0	168	0.5
9	cpw	220	219	1.65	-	2.8
10	cpw	180	215	2.3	-	0.3

**Figure 3.19:** Example of HFSS simulation model for textile transmission line in GSG configuration with floating wires, length=10mm

mission line measurements:

- Cross-running wires within the fabric increase permittivity and thus, lower line impedance.

- First notches in the frequency response occur at about  $2GHz$ . The PETEX triple wire without floating wires in parallel does not show any major notches up to  $6GHz$ .
- Parallel running, floating wires mainly affect the frequency response above  $2GHz$ .
- The smoothed curves represent a good approximation of the actual permittivities.
- The analytical wire transmission line model according to Formula (3.2) reveals a valid approximation for PETEX and for fabric version 3.
- The CPW model delivers valid results for fabric version 3 in CPW-like configuration.
- Measurement equipment and cables with reference impedance close to  $250\Omega$  would improve measurement result by suppressing big reflections and resonances. However, such equipment is commercially not available, of course.

Table 3.4 gives a qualitative summary of the effects of floating wires on the transmission line parameters  $Z_0$ , BW and  $\epsilon_r$ .

**Table 3.4:** *Qualitative overview of effects of the different transmission line configurations on  $Z_0$ , BW and  $\epsilon_r$  ( $\vee$ =decrease,  $\vee\vee$ =strong decrease,  $\wedge$ =increase,  $\wedge\wedge$ =strong increase)*

	Floating wires orientation within fabric		
	parallel	across	parallel & across
$Z_0$	$\vee$	$\vee\vee$	$\vee$
BW	perturbation	-	strong perturbation
$\epsilon_r$	-	$\wedge\wedge$	$\wedge$

Generally, an arbitrary wiring structure in PETEX always incorporates floating wires. Because of this fact, transmission lines in wire pair configuration are recommended when high bandwidth is required. Triple wire configuration is favored when the emphasize lies on low line impedance.

### 3.4. Screen-printed textile transmission lines

This section presents textile transmission lines as well. However, the transmission lines consist of screen-printed conductive ink instead of copper wires.



It is shown that a  $50\Omega$  line impedance is achievable with this printing technology.

Secondly, mechanical folding tests are performed in order to analyze the adhesion of the ink to the fabric.

### 3.4.1. Textile substrate and printing ink

An acryl-cotton woven fabric with a surface roughness  $R_a = 80 - 100\mu m$  is used as substrate for screen-printing of transmission lines. A picture of this fabric is shown in Figure 3.20. The fabric possesses no mesh openings such that acceptable printing results are achieved<sup>3</sup>. It features a thickness of  $0.25mm$  and a relative permittivity  $\epsilon_r = 2.68$ . The permittivity has been determined by capacitive plate measurement.



**Figure 3.20:** Acryl-cotton substrate for screen-printing

The ink is a silver-filled paste [1] with a solid content of  $73.5\% - 76\%$ . It has a viscosity of  $10 - 25mPa.s$  and a specific resistance of  $0.625\Omega.mm^2/m$ . The curing has to be performed at  $120^\circ C$  for 15 min at least. Curing time is a crucial factor to achieve good conductivity.

### 3.4.2. Screen-printing

Screen-printing is a simple, but powerful printing process. Generally, it consists of a structured stencil mounted in a frame for stabilization. The frame lies on top of the printing media (here: the acryl-cotton fabric) and the ink (here: conductive silver paste) is pressed through the stencil by a scraper onto the media.

The stencil for the transmission lines consists of a *Sefar PET 1000 48-70* with a mesh aperture of  $133\mu m$ , a sieve opening of  $41\%$  and a sieve thickness of  $110\mu m$ . The theoretical ink volume per square meter is  $45.1cm^3/m^2$ .

<sup>3</sup>Another fabric with mesh openings did not deliver satisfactory printing results

Smaller mesh openings deliver unsatisfactory results using this ink, i.e. unprinted areas.

### 3.4.3. Transmission line structure

In our investigations, coplanar waveguide structures with finite-width ground planes (FW-CPW) [84] have been printed on the acryl-cotton fabric. A pictures of such a transmission line is shown in Figure 3.21.

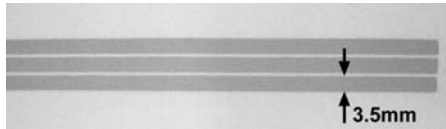


**Figure 3.21:** Printed textile transmission line (10 print pass)

Figure 3.22 shows a close-up of the transmission line structure printed with a different number of passes. 10 print passes mean that paste is pressed through the stencil at the same location for 10 times. It can be seen that the number of passes affects the fineness of the structures, especially on the edges. On the other hand, a higher number of passes results in a better penetration of the fabric and therefore, in a thicker paste layer. It is directly related to its conductivity. Although the stencil has been designed for 3mm wide lines with 1mm gaps in-between, the printed line possessed a width of 3.5mm with 0.5mm gaps in-between in Figure 3.22(b).

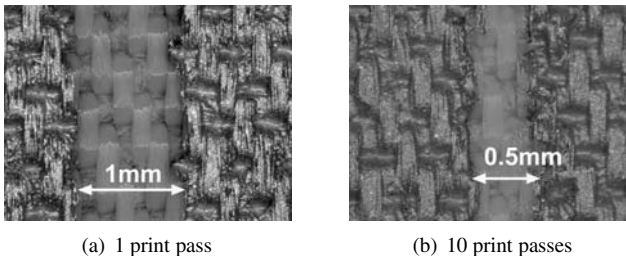


**Figure 3.22:** Screen-printed structures

### 3.4.4. Electrical measurement results

#### DC resistance

During printing, the stencil limits the silver paste thickness to  $45.1\mu\text{m}$ . For all samples, a paste thickness of  $39.5 - 40\mu\text{m}$  is measured independent on the number of printing passes. In contrast, the electrical resistance depends on the number of passes as depicted in Figure 3.23. Multiple print passes cause a better ink penetration of the fabric. Given the measured resistance of the printed lines, a paste thickness that agrees with the specific resistance of the ink can be calculated. We call this thickness *effective thickness* and it is indicated in Figure 3.23 as well.

Notice as well that the utilized fabric did not show any conductivity on the backside.

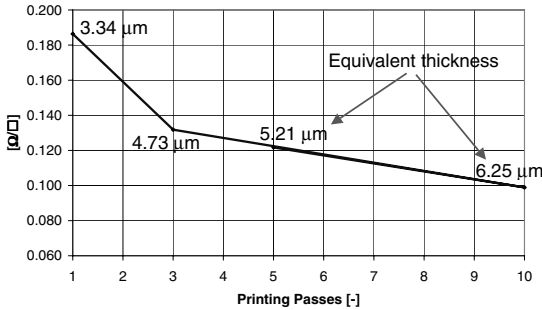


**Figure 3.23:** DC resistance as a function of printing passes

#### Transmission line parameter

The measurement of the transmission line parameters utilizes the same setup and methods as in Subsection 3.3.2. Again, the transmission lines are kept straight and are surrounded by air. The presented values and figures are obtained from the transmission line that has been manufactured using 10 printing passes.

The measured line impedance  $Z_0$  of this line is shown in Figure 3.24.

The bandwidth BW and the effective relative permittivity  $\epsilon_{r,eff}$  have been extracted using techniques as described in Section A.1. These parameters are shown in Figure 3.25. The printed line features a bandwidth of about  $4.7\text{GHz}$  ( $-0.5\text{dB/cm-point}$ ).

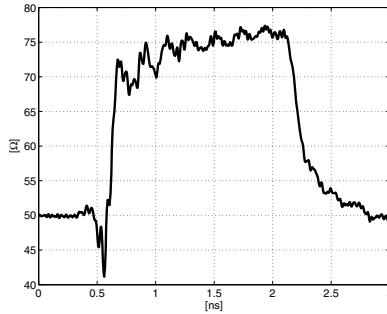


**Figure 3.24:** TDR/TDT measurement of the printed transmission line (Figure 3.21)

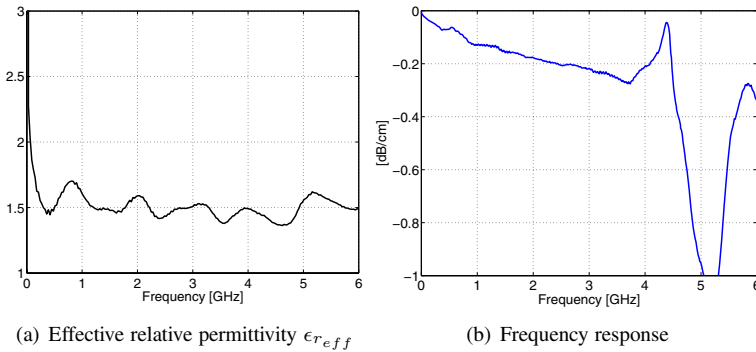


**Figure 3.25:** Parameters of screen-printed transmission line (Figure 3.21)

### Transmission line parameter verification

For verification reasons, line impedance and permittivity have been obtained and extracted using several approaches. Table 3.5 gives an overview of the results. VNA and TDR are measurement results using vector network analyzer and time domain reflectometry, respectively. Ansoft HFSS [11] is a 3D FEM simulation tool. As comparison, the values for a CPW with infinite ground planes and no backed ground are given.

The obtained impedances differ by about 10%. A  $50\Omega$  line impedance can

<sup>4</sup>Using techniques described by Grzyb *et al.* in [41].

**Table 3.5:** Printed transmission line parameter summary

Method	$Z_0$	$\epsilon_{r_{eff}}$
VNA	$72\Omega^4$	1.4
TDR	$75\Omega$	—
HFSS	$80\Omega$	1.3
CPW	$70\Omega$	1.26

be achieved by increasing the trace width to  $10mm$  while decreasing the gap width to  $0.4mm$ .

### 3.4.5. Mechanical stresses

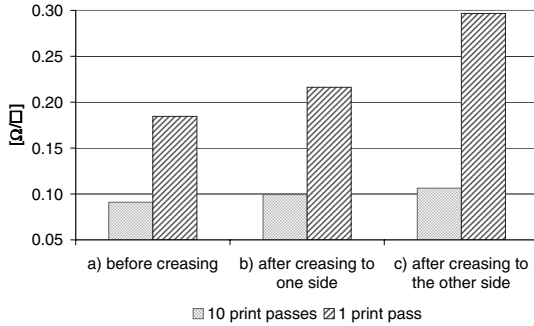
Several stress tests are performed to determine the mechanical properties of the cured paste with regard to creasing. Figure 3.26 illustrates how creasing of the fabric with the printed transmission lines is conducted. The DC resistance is monitored during the tests in order to register changes in the printed structure.

We have chosen this setup since no test standards for conductive structures printed on fabrics exist.

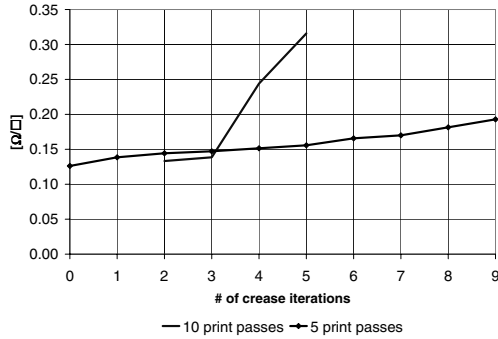
**Figure 3.26:** Creasing of the fabric with printed transmission lines

Figure 3.27 shows the DC resistance change when the transmission line is stressed with b) a single crease to one side and straightened again followed by c) a single crease to the other side and straightening again.

Secondly, the resistance is measured in dependence of the number of creasing iterations at a certain location on the transmission line. It is depicted in Figure 3.28. Note that the resistance of the 10 times printed line suddenly increases. The creasing edge has slightly been shifted during the folding iterations. This shift has led to a larger area where the paste crumbled and therefore, to a higher resistance. Pictures of those effects are shown in Figure 3.29.



**Figure 3.27:** DC resistance changes due to creasing



**Figure 3.28:** DC resistance changes vs. number of creasing iterations

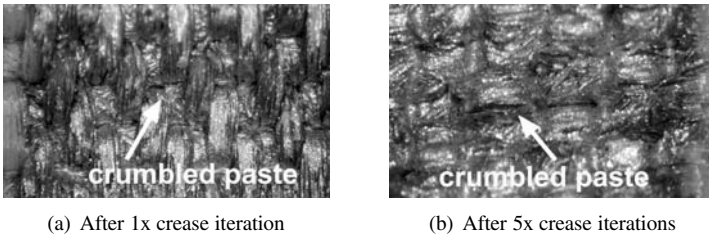


**Figure 3.29:** Crumbling occurs after crease iterations

### 3.4.6. Results and Conclusions

In contrast to wire-based textile transmission lines,  $50\Omega$  line impedance can be achieved with screen-printed lines. The impedance discontinuity between measurement equipment and our printed transmission line is about 3 times lower compared to wire-based transmission lines. Thus, signal reflections are lowered by this amount and the extracted line parameters, bandwidth and  $\epsilon_r$ , are less perturbed. The printed line with its bandwidth of  $4.7GHz$  outperforms the wire-based transmission lines.

The minimal feature size in the screen-printing process depends not only on the paste, the stencil and the number of printing passes, but also on the textile substrate. It is about  $0.5mm$  for line width and spacing on our fabric. Therefore, printing is a suitable technique for coarse structures such as patch antennas, ground planes and simple one-layer routing structures.

Bending with a radius larger than  $1cm$  does not affect the DC resistance at all. Bending with smaller radii or even folding results in an increasing resistance due to cracks in the silver paste. The effect is bigger when fewer printing passes have been applied. Eventually, the paste crumbles from the fabric and conductivity is lost. Creasing at slightly shifted locations should be prevented as indicated in Figure 3.28. If folds can be avoided, 5 – 10 printing passes give good results regarding geometrical precision and electrical performance.

The cured silver paste with a solid content of about 75% suffers from brittleness. Jiang *et al.* [46] showed for a carbon coating that adhesion improves the smoother the substrate surface is. Therefore, a rubber-like layer could first be deposited onto the acryl-cotten fabric to planarize the surface. The silver paste on top of it should then show better adhesion.

## 3.5. Textile vias and interconnects

This section focuses on the copper wire based fabric PETEX. A manufacturing technology is discussed in order to establish an arbitrarily connected wiring structure within the fabric. This technology is necessary for SoT to enable the wiring of components assembled on the fabric. Such a wiring structure consists of single interconnects between copper wires called *textile via*. Figure 3.30 shows a sketch of such a textile via.

Considering the arrangement of the wires within PETEX, it is obvious that only perpendicular wiring structures can be implemented with textile vias.

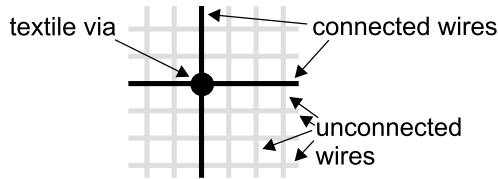


**Figure 3.30:** Sketch of a textile via

### 3.5.1. Manufacturing of a textile via

The wires in PETEX are insulated against each other. Hence, the insulation needs to be removed at a point in order to interconnect crossing wires. Such a *textile via* is the fundamental building block for a routing structure in the fabric. The four necessary manufacturing steps of a textile via are explained in the diagram in Figure 3.31.

Figure 3.32 shows a cross-section through a textile via. The rough surface of the copper wires results from laser treatment.

### 3.5.2. Determination of the laser parameters

Laser light is applied in three process operations during manufacturing of a textile via. The goal is to determine the laser parameters for the three operations:

- a) Removal of polyesterimid (or polyurethane) coating of the copper wire (laser ablation)
- b) Removal of polyester yarn
- c) Cutting of the copper wire

Laser ablation is a method to remove a layer of a specific material (e.g. polymer) without damaging the underlying other material (e.g. copper). An introduction about the fundamentals of laser ablation is given by Lippert *et al.* in [56] and by Duley in [31].

Removal of the polyester and the coating needs special attention. On the one hand, the polyester as well as the coating can carbonize during laser treatment. Secondly, the polyester can melt and plaster up. In both cases, the treated spot might be contaminated or overcast with polyester again.

On the other hand, the varnish must entirely be removed without damaging the copper wire. Figure 3.33 illustrates the procedure to determine the



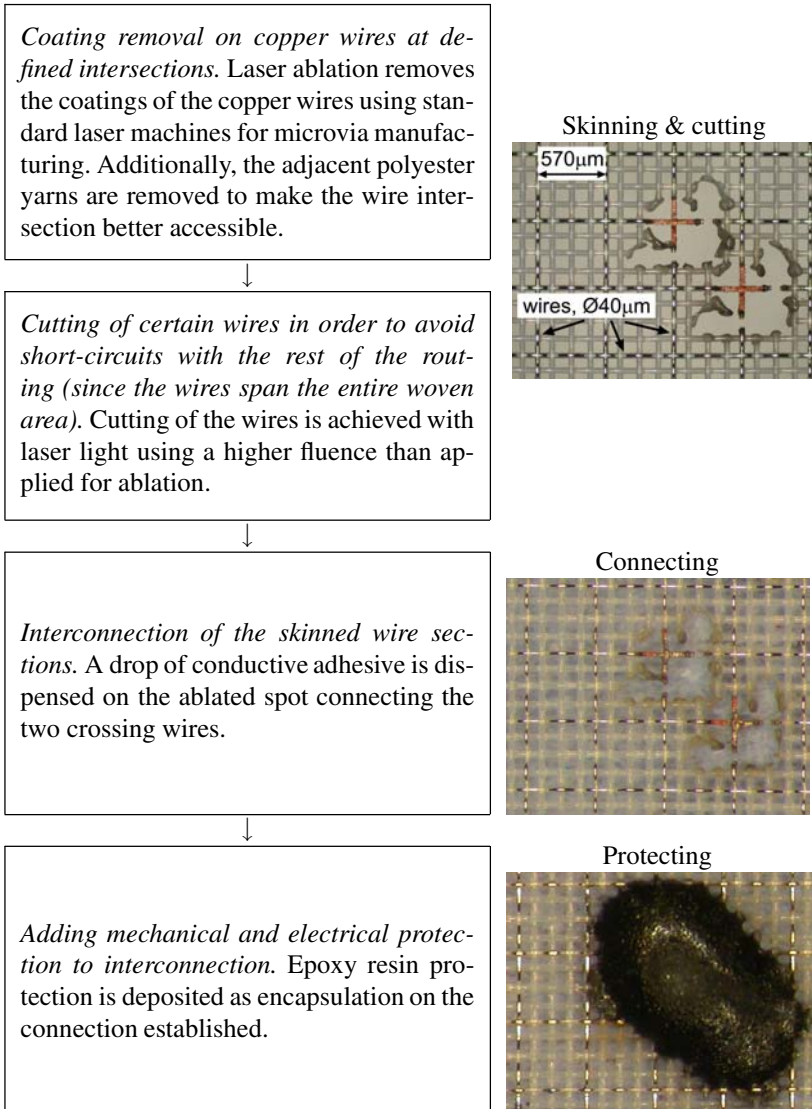


**Figure 3.31:** Manufacturing steps of a textile via

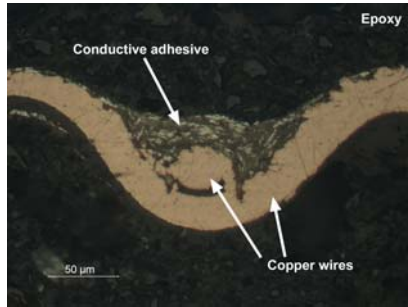


**Figure 3.32:** Cross-section through a textile via

optimal laser ablation parameters. The absorption spectrum identifies the optimal laser wavelength  $\lambda$  and the profilometry specifies the ablation rate  $d(F)$ .



**Figure 3.33:** Procedure to obtain the optimal laser parameters for ablation.

Cutting of the copper wires is not critical since those laser parameters are already known from literature.

In the following subsections, we first identify the ablation parameters for wire skinning with a XeCl excimer laser. Secondly, we give the parameters for a Nd:YAG laser at  $355nm$  wavelength since such lasers are used in industrial machines for PCB manufacturing, e.g. [35, 64]. This laser type can remove the wire coating (operation a) and the polyester yarn (operation b) in one pass.

### Preparation of the varnish specimens

The light absorption spectrum of the wire varnish determines the optimal laser wavelength for skinning. The spectrum is measured with a Varian Cary 500 spectrometer [99]. Since this device cannot directly measure the spectrum of the coated wire, specimens are prepared on glass substrates. A wire varnish layer of  $2.5\mu m$  thickness is spin-coated onto glass substrates at  $2000rpm$ . Curing of the varnish is then performed according to Table 3.6. It is important to achieve an entirely cross-linked polymer coating.

The spectrometer measures the transmittance of the coating by comparing the specimen to a reference glass substrate without coating. With this method, the spectrum of the pure coating is determined.

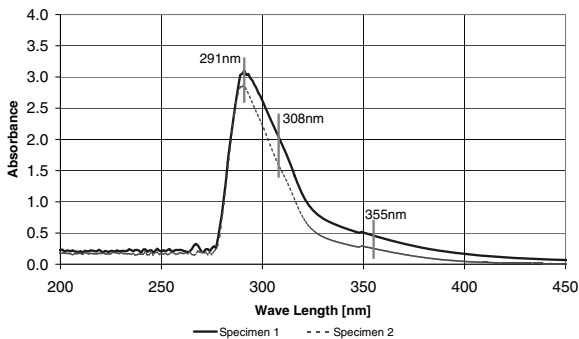
**Table 3.6:** *Curing parameters of the wire varnish*

	Temperature	Time
Specimen 1	500°C	1 min
Specimen 2	300°C	20 min

### Absorption spectrum of the wire coating

The absorption spectrum of the wire coating is shown for the two specimens in Figure 3.34. The absorbance is defined as  $A = -\log_{10}(T)$  whereas  $T$  corresponds to the transmittance [103].

According to Elektro-Feindraht AG<sup>5</sup>, the coating of the wire is deposited and cured in several iterations during the manufacturing process. Since the measured spectra coincide for the differently cured specimens, we conclude that the polymer is entirely cross-linked for both specimens. Thus, the coating on the glass substrate is equal to the wire varnish.



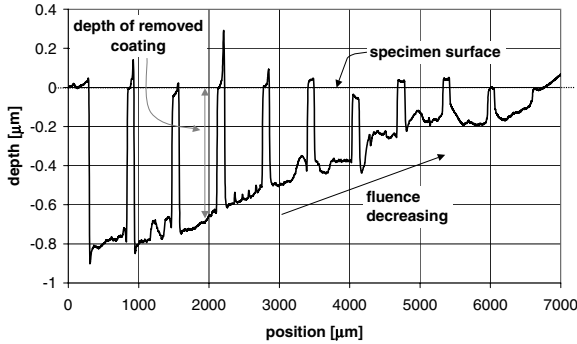
**Figure 3.34:** *Light absorption spectrum (UV-Visual spectrum) of the wire varnish*

Figure 3.34 indicates that the wavelength of a XeCl excimer laser (wavelength 308nm) is nearest to the absorption maximum at 291nm.

<sup>5</sup>Elektro-Feindraht AG is the manufacturer of the copper wires

### Ablation matrix and profilometry

In order to determine the ablation rate at  $308nm$ , an ablation matrix is generated on a specimen with ascending number of laser impulses in one direction of the matrix and with increasing laser fluence  $F$  (energy density) in the other direction. Afterwards, the surface of the specimen is inspected by profilometry for each row in the matrix. Figure 3.35 illustrates such an inspected row for a constant number of laser impulses.



**Figure 3.35:** Row of the ablation matrix inspected by profilometry (constant # of laser impulses)

The ablation rate shown in Figure 3.36 is then obtained from the depths in the ablation matrix. It is depicted for one and five laser impulses. The coating layer on the glass substrate has entirely been removed when using more the five laser impulses. The measured ablation curve is usually approximated with Formula (3.3) [57] where  $F_{th}$  is the laser fluence threshold. Laser fluences below the threshold  $F_{th}$  do not ablate coating. The approximation (3.3) is shown in Figure 3.36 as well. For a better fit at small laser fluences, only measurements until  $400mJ/cm^2$  are considered for the approximation.

$$d(F) = \frac{1}{\alpha_{eff}} \ln \frac{F}{F_{th}} \left[ \frac{m}{impulse} \right] \quad (3.3)$$

The identified laser parameters are given in Table 3.7. The effective absorption coefficient  $\alpha_{eff}$  [57] is determined with an accuracy of  $\pm 0.18 \cdot 10^{-3}cm^{-1}$ . Thus, an ablation rate of about  $200nm$  per impulse is achieved above a laser fluence of  $400mJ/cm^2$ . In conclusion, the entire coating layer on the copper wire ( $\sim 7\mu m$  thickness) is removed with about 35 laser impulses.

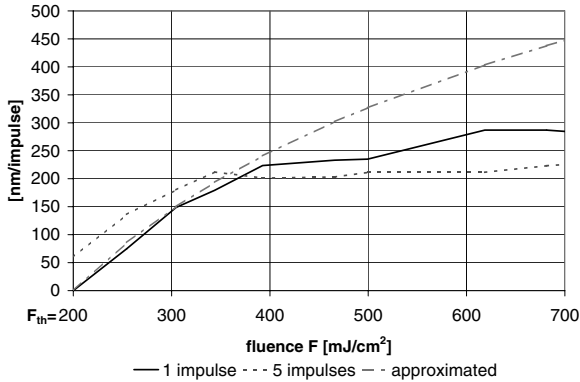


**Figure 3.36:** Ablation rate  $d(F)$  of the wire coating (@ 308nm)

For comparison, the ablation parameters for copper at 308nm are listed in Table 3.7 as well. These parameters have been taken from Torrisi *et al.* [96]. The fluence threshold for copper is about 15 times higher than the threshold for the coating. Thus, the copper will not be damaged during ablation of the coating.

**Table 3.7:** Laser ablation parameters at 308nm

Material	$\alpha_{eff}$ [ $m^{-1}$ ]	$F_{th}$ [ $mJ/cm^2$ ]
Coating	0.28	200
Copper	$7.5 \cdot 10^7$ , [96]	3000, [96]

### Nd:YAG laser parameters for wire skinning

A XeCl excimer laser is optimal for skinning of the wire coating. However, a Nd:YAG laser at 355nm wavelength is used later on since industrial machines in PCB manufacturing work at this wavelength. Note that the absorbance in Figure 3.34 has already dropped significantly at a wavelength of 355nm.

Such a laser can remove the wire coating (operation a) and the polyester yarn (operation b) in one step using an impulse energy of  $80\mu J$  at a focal diameter of  $20\mu m$  and an impulse repetition rate of  $30kHz$  with impulse length of  $100ns$ . The processing point (laser spot) is moved with a velocity of  $3.2\mu m/impulse$  ( $= 100mm/s$ ) during laser treatment.

According to literature [104], the ablation threshold for copper is at  $F_{th} = 3J/cm^2$  and the absorption coefficient for copper is  $\alpha_{eff} = 7.31 \cdot 10^7 m^{-1}$  at  $355nm$  wavelength.

### Cutting of the wires using laser light (operation c)

Higher laser fluence is needed in the wire cutting step (operation c). A laser energy of  $250\mu J$  at a focal diameter of  $20\mu m$  is needed at  $355nm$  wavelength at an impulse rate of  $15 - 18kHz$  with impulse length of  $100ns$  and a mark speed of  $100mm/s$ .

#### 3.5.3. Wire interconnect with conductive adhesive

The adhesive drops of about  $0.5nl$  are dispensed using a needle with diameter  $0.2mm$  (Gauge 27). We apply a silver-filled conductive epoxy (E4110 by EPO-TEK [34]) that is cured at  $100^\circ C$  during 3 hours.

#### 3.5.4. Epoxy encapsulation as mechanical protection

The epoxy encapsulation is dispensed as well using Stycast 2850 by Emerson & Cuming [33]. Its viscosity of  $10 - 15Pa.s$  allows deposition onto the fabric without spreading and therefore, no casting mold is necessary. The curing happens at room temperature. Currently, dispensing of epoxy is applied on both sides of the fabric in order to encapsulate a textile via. Lowering of the viscosity would enable the epoxy to flow around the entire textile via while deposited only on one side. This step would ease the manufacturing process. However, a lower viscosity could then lead to spreading of the epoxy. Eventually, the optimal viscosity depends on the fabric mesh openings.

A feasible alternative is the use of the so-called 'dam and fill' approach from glob-tops in chip packaging [2, 52, 75]. There, an epoxy dam is first dispensed around a chip. Afterwards, the cavity inside the dam is filled with epoxy. The dam prohibits spreading of the filler epoxy over the entire area. Figure 3.37 illustrates the glob-top manufacturing process. The dam epoxy usually has a viscosity of  $> 500Pa.s$  and the cavity fill epoxy about  $30Pa.s$  [2]. Both epoxies feature similar chemistry, but the cavity epoxy has a lower fill loading compared to the dam epoxy.

An introduction to the use of polymers and polymer encapsulations in electrical engineering is given by Schaumburg in [82] as well.

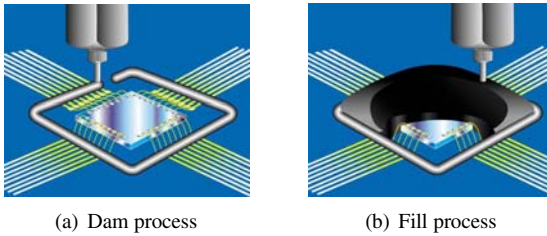


**Figure 3.37:** *Manufacturing of a glob-top encapsulation [75]*

### 3.5.5. Electrical characterization of a textile via

In this subsection, textile vias and textile via configurations are characterized regarding DC resistance, line impedance discontinuity and frequency response. Five textile via configurations are presented in order to interconnect the SG and GSG transmission lines introduced in Section 3.3.

#### DC resistance

The DC resistance of a textile via is obtained by measuring a cascade of vias using the 4-wire resistance measurement method [3]. The resistance of a single via  $R_{via}$  can then be determined by Formula (3.4).  $R_{meas}$  corresponds to the measured resistance whereas  $R_{wire_H}$  and  $R_{wire_V}$  correspond to the resistance of the plain copper wire ( $50\mu m$  diameter) in horizontal and vertical direction, respectively. The two values are known from the overall wire length in the cascade structure and the wire resistance in warp and weft direction given in Subsection 3.2.2. The term '-2' in the denominator occurs since the two outermost vias do not induce any voltage drop. They are just used to connect the voltage sensing. Figure 3.38 illustrates such a cascade of textile vias.

$$R_{via} = \frac{R_{meas} - R_{wire_H} - R_{wire_V}}{N - 2} \quad [\Omega] \quad (3.4)$$

The average resistance  $R_{via}$  reaches  $14.1m\Omega$  over  $N = 21$  vias. The standard deviation is  $\sigma = 0.18m\Omega$ .

#### Textile via variants for RF measurements

Textile transmission line configurations have been introduced in Section 3.3. In order to enable routing capability of such transmission lines, suitable via

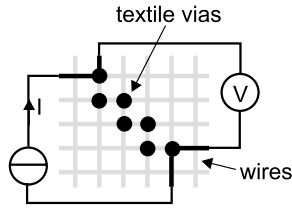


**Figure 3.38:** Cascade structure to measure the DC resistance of textile vias

configurations are essential. Figure 3.39 illustrates five possible via variants, two for wire pair configuration and three for tripe wire configuration. Whereas variant 1 in Figure 3.39(a) has the disadvantage of unequal wire lengths (here: the signal wire is longer than the ground wire), variant 2 in Figure 3.39(b) realizes a cross-over to maintain equal wire lengths. Variant 3 in Figure 3.39(c) and variant 4 in Figure 3.39(d) show similar properties. Finally, variant 5 in Figure 3.39(e) is a mix of variant 3 and 4.

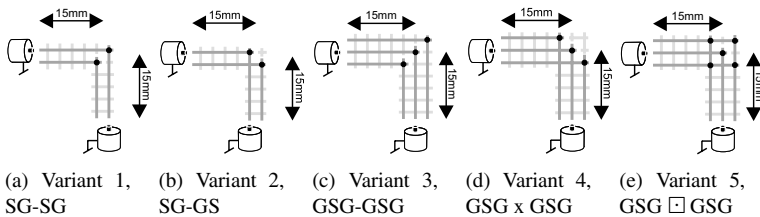


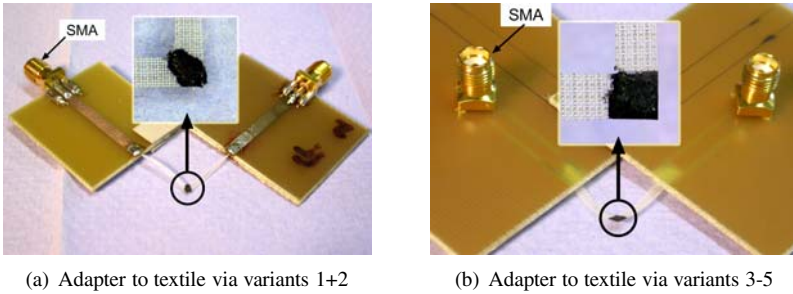
**Figure 3.39:** Textile via variants using PETEX

The feed transmission lines to the vias have been isolated in advance to remove floating wires in parallel. The same SMA adapters as for the transmission lines in Section 3.3 have been applied for measurement of the textile vias as seen in Figure 3.40. Secondly, the same measurement equipment and setup as in Section 3.3 have been used during the via measurements.

### TDR measurements

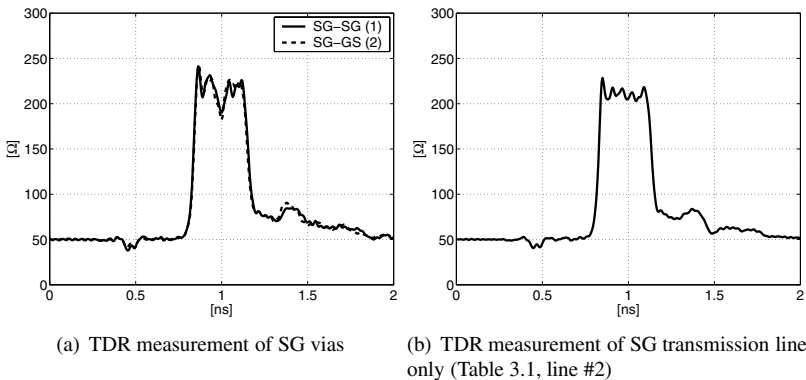
Figure 3.41(a) depicts the TDR measurements of via variants 1 and 2. The vias introduce discontinuities in line impedance. For comparison, the measurement of a transmission line of the same length is given in Figure 3.41(b).





(a) Adapter to textile via variants 1+2

(b) Adapter to textile via variants 3-5

**Figure 3.40:** Pictures of SMA adapters for textile via measurements

(a) TDR measurement of SG vias

(b) TDR measurement of SG transmission line only (Table 3.1, line #2)

**Figure 3.41:** TDR measurements of textile via variants 1+2

Figure 3.42(a) depicts the TDR measurements of via variants 3 till 5. The vias cause a big notch in the impedance characteristic. The TDR measurement of a transmission line of the same length in triple wire configuration is given in Figure 3.42(b).

### Scattering parameters

Figures 3.43 and 3.44 show the scattering parameter (s-parameter)  $S_{21}$  of the via variants. Since a via is a passive structure its s-parameters are symmetrical, thus,  $S_{22} = S_{11}$  and  $S_{12} = S_{21}$ . Some figures contain 2 curves corresponding to two measured specimens of the same via variant.

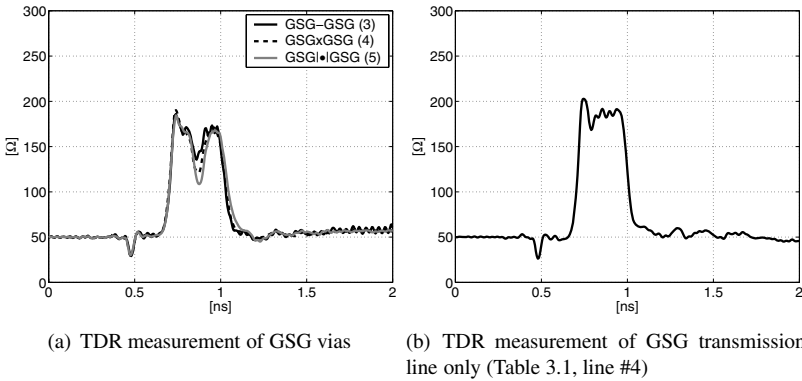


**Figure 3.42:** TDR measurements of textile via variants 3-5

The s-parameters of the plain vias have been deembedded using s-parameter measurements of two corresponding textile transmission lines as well as an s-parameter measurement of the textile via including the feed lines. The deembedding applies an extended approach of the method to extract transmission line parameters from measurements described in Section A.1. This extension is based on the paper of Grzyb *et al.* [41]. Since the extraction of the textile transmission line parameters already includes many error sources such as odd modes (See section A.1), it is clear that the via deembedding faces the same problems. The figures also contain these odd modes.

Among the five variants, variants 1+2 show the best performance. Both variants feature a bandwidth of approximately  $500 - 600\text{MHz}$  whereas variants 3-5 possess a bandwidth of only about  $300\text{MHz}$ .

## Conclusion

From the s-parameter measurements, it can be seen that vias in wire pair configuration perform better than in triple wire configuration. The adjacent ground wires and vias in triple wire configuration generate odd modes at lower frequencies than in wire pair configuration. The unequal lengths of signal and ground wires do not affect the frequency response in any via variant.

It is obvious that the vias limit the bandwidth of a wiring structure when compared with the results of the transmission lines in Section 3.3. Since an arbitrary wiring structure in PETEX is always surrounded by floating wires, the SG transmission line configuration along with via variants 1 or 2 are re-

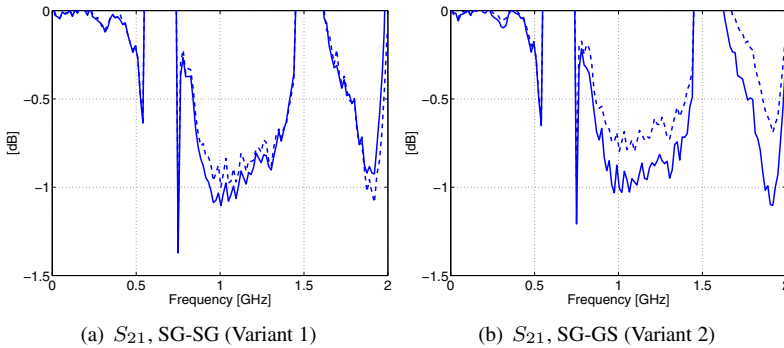


**Figure 3.43:** Scattering parameters of SG vias

commended to achieve the best overall bandwidth.

### 3.6. Interposer Technology

Whereas Section 3.5 focused on interconnects within the fabric, electrical component assembly onto the fabric is described in this section. The proposed interposer technology adapts the pitch mismatch between components and fabric and allows the wiring of arbitrary components.

Firstly, the problems of a direct component assembly on fabrics are identified and the use of interposer is motivated. Secondly, the principle build-up of such an interposer is illustrated. We distinguish between application-dependent and application-independent interposers. An optimization of application-independent interposers is presented regarding shortest overall trace lengths. Eventually, we give formulas to compute the fabric area consumption of interposers.

#### 3.6.1. Introduction and Motivation

There is a significant difference between PETEX and conventional substrates (e.g. FR4). The trace pitch can vary on conventional substrates whereas the wire pitch within PETEX is constant.

Even though the component pitch matches the fabric pitch, several aspects must be considered. Figure 3.45 points these aspects out. Since the pads are aligned in columns in Figure 3.45(a), they connect to the same copper wires. Thus, cuts are needed to prevent shorts between component pads. Such cuts

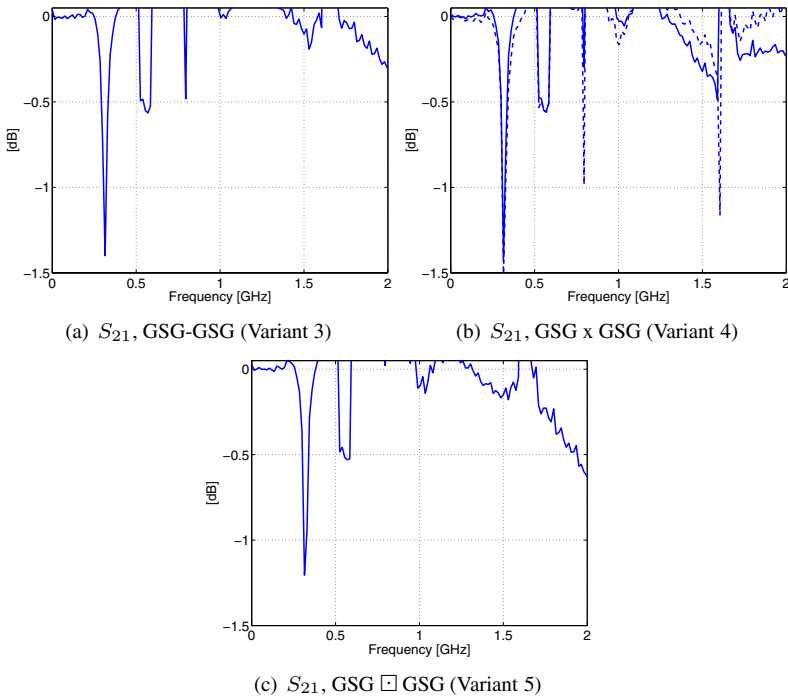


**Figure 3.44:** Scattering parameters of GSG vias

result in a weakened mechanical stability of the substrate as well as in an additional step in the manufacturing process.

Secondly, connection of components such as BGAs necessitates several wiring layers in general. Methods to estimate the number of routing layers on conventional substrates are given in [21, 37, 42, 98]. However, these methods are not valid for PETEX. As soon as more than one pad row exists on each side of the package, an escape routing is not feasible anymore as depicted in Figure 3.45(b).

In conclusion, an interposer has to be inserted between component and fabric substrate that re-distributes the pads of the component to the wires in the fabric as shown in Figure 3.46.

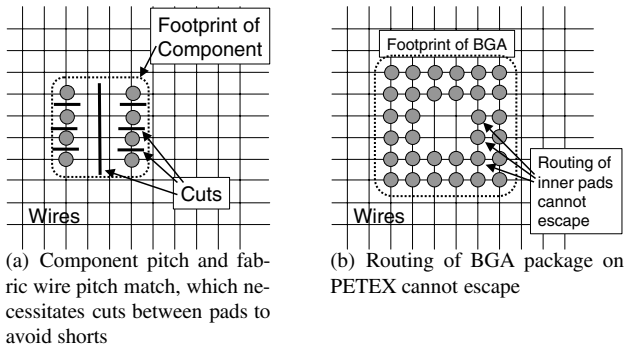


**Figure 3.45:** Problems of direct mounting of packages onto PETEX

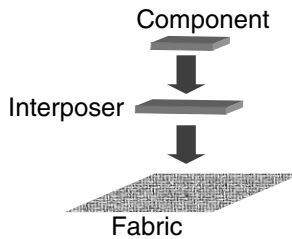


**Figure 3.46:** Component assembly with interposer on the fabric

### 3.6.2. Interposer Approach

An interposer adapts the component pitch to the substrate's pitch. This principle is already established in the BGA technology [17, 36] in order to adapt the chip pitch to the pitch of the substrate, e.g. FR4.

Applied to PETEX, an interposer can even eliminate the cuts shown in Figure 3.45(a) by re-distributing the component pads in an orthogonal manner seen in Figure 3.47.

Such an interposer features several advantages in comparison to a direct component attach:

- No cuts in the fabric are needed for the escaping routing of a component. Therefore, mechanical stability of the fabric is unaffected.
- The pitches of the components and the fabric can be adapted to each other.

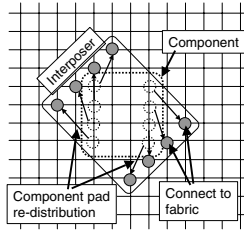


**Figure 3.47:** *Interposer re-distributes the component pads to align with the fabric pitch*

- No restrictions of the number of component pads exist.
- The interposer enables assembly independent of the component package. Therefore, the interposer supports chip packaging technologies such as bare dies, flip chips, CSPs, BGAs and SO packages.
- The interposer pad assignment can be optimized to the application circuit. Thus, a pre-routing can be introduced on the interposer.

Figure 3.48 illustrates a possible interconnect structure between two interposers mounted on the fabric. Since the copper wires in the fabric are insulated against each other, no cuts are needed.

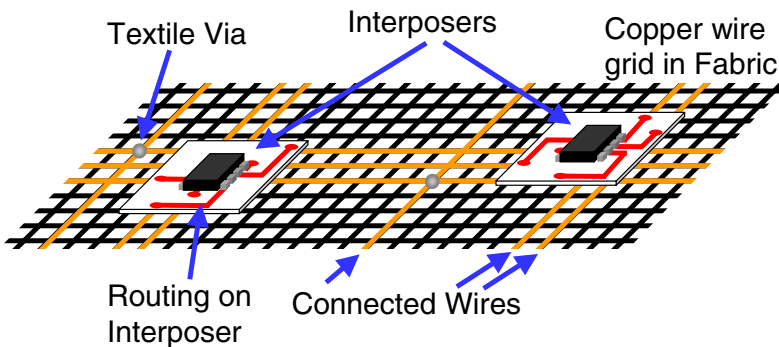


**Figure 3.48:** *Electronic circuit on the fabric using interposers*

### 3.6.3. Interposer types

Two options are feasible for interposers. The interposers are either tailored towards the application circuit or independent of the circuit. Further, we call the pads on the interposer on the component side 'component pads' and the pads towards the fabric 'interposer pads'.

#### Application-dependent interposer

The use of an application-dependent interposer results in a simple wiring structure in the fabric. The component pad assignment to the interposer pads on the fabric is arbitrary. Therefore, the pad assignment can be used to simplify the wiring structure within the fabric. Ideally, only transmission lines with few branches remain in the fabric wiring.

On the other hand, this approach leads to a countless number of interposer variants for similar electronic components.

The principle build-up of an application-dependent interposer is shown in Figure 3.49.

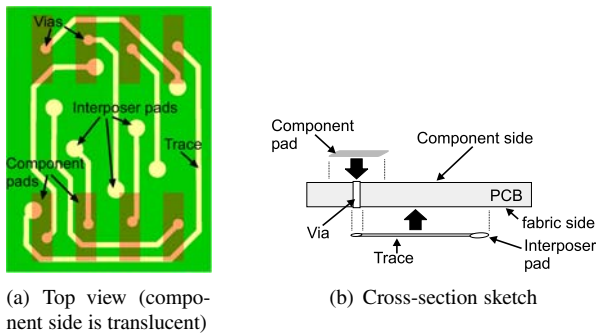


**Figure 3.49:** *Example for an interposer build-up (component pads on top side, interposer pads on bottom side)*

In fact, vias in interposers cannot only be used as connect from the top to the bottom side, but as interposer pads to the fabric simultaneously. This design is utilized for the interposer example in Figure 3.50.

### Application-independent interposer

An application-independent interposer has a fixed assignment of the component pads to the interposer pads. The assignment can for instance be optimized for shortest connects between these pads.

Figure 3.50 shows the two sides of an application-independent interposer.

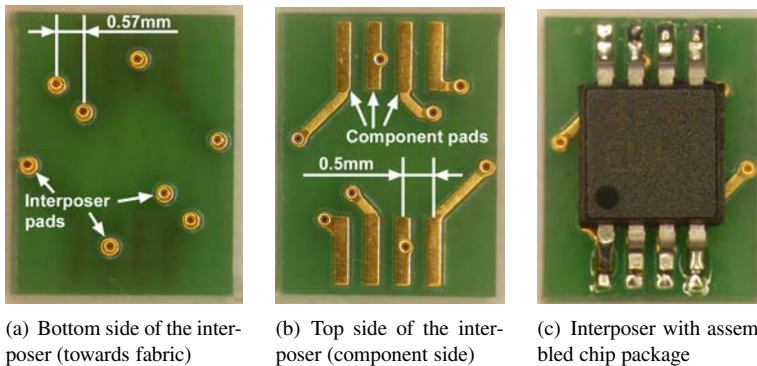


**Figure 3.50:** *Application-independent interposer to adapt a  $\mu$ SOP chip package to PETEX*

### Application-independent interposer with shortest trace lengths

As mentioned before, application-independent interposers can be optimized such that the total trace length on the interposer is minimal.

Note that there exist  $n!$  potential assignments of the  $n$  component pads to the interposer pads. Secondly, there are  $n!$  arrangements to distribute the interposer pads on the fabric. In total,  $(n!)^2$  variants have to be tested in order to find an optimum.

The problem of the pad assignment is known as *bipartite weighted matching problem with complete matching* in graph theory [30]. Figure 3.51 illustrates the graph problem for one interposer pad arrangement where  $w_k$  corresponds to the distances between component pads and interposer pads. Approach (3.5) states the optimization problem. A unique solution does not exist: if weights  $w_k$  are equal, the edges in the graph can be interchanged.

$$\min_{\text{s.t. complete matching}} \sum_k w_k \quad (3.5)$$



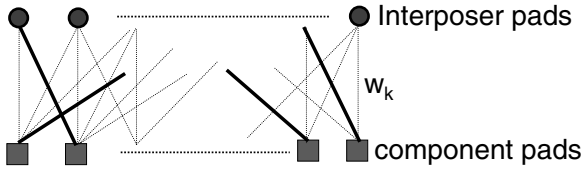


**Figure 3.51:** Pad assignment problem illustrated for one interposer pad arrangement ( $w_k$ : distance between component and interposer pads = weights in the graph)

An approach to solve the assignment problem is given in Formula (3.6) and (3.7) where  $\underline{i}, \underline{c} \in \mathbb{C}^n$ .  $\underline{i}$  denotes the coordinates of the interposer pads and  $\underline{c}$  denotes to the coordinates of the component pads. The dimension  $n$  of the two vectors is equal to the number of component/interposer pads. Real parts of  $\underline{i}$  and  $\underline{c}$  correspond to the x-coordinates of the pads and imaginary parts correspond to the y-coordinates of the pads as depicted in Figure 3.52.

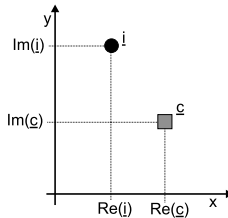


**Figure 3.52:** Interposer coordinate notation for optimization problem (3.7),  $\underline{i}, \underline{c} \in \mathbb{C}$

$$\underline{\Delta} = A \cdot \underline{i} - \underline{c} = \begin{bmatrix} 0 & 1 & \dots & 0 \\ 0 & 0 & \dots & 1 \\ \vdots & \vdots & \vdots & \vdots \\ 0 & \dots & 1 & 0 \end{bmatrix} \begin{bmatrix} i_1 \\ i_2 \\ \vdots \\ i_n \end{bmatrix} - \begin{bmatrix} c_1 \\ c_2 \\ \vdots \\ c_n \end{bmatrix} \quad (3.6)$$

$$\min_{\forall \underline{i}} \min_A \underline{\Delta}^* \underline{\Delta} \quad (3.7)$$

s.t.  $\underline{1}^T A = \underline{1}^T$   
 $A \cdot \underline{1} = \underline{1}$   
 $|\det(A)| = 1$

$\underline{c}$  is a constant containing the coordinates of the component pads.  $\underline{i}$  contains the coordinates of the interposer pads for one of the  $n!$  existing interposer pad arrangements.  $A$  is a full-rank matrix containing only one '1' in each row and column. It conducts the assignment of the interposer pads to the component pads. The inner minimization in (3.7) shuffles the '1's in  $A$  such that the overall lengths between interposer pads and component pads are minimal for a given interposer pad arrangement  $\underline{i}$ . The given constraints guarantee that only one '1' is in each row and column of  $A$  and that  $A$  is full-rank. The outer minimization iterates over all possible interposer pad arrangements  $\underline{i}$  to find an optimum.

Figure 3.53 depicts an optimal solution of an interposer pad arrangement and a component pad assignment, which minimizes the total trace lengths on the interposer. Solid squares denote the center of the component pads whereas solid circles denote the interposer pads towards the fabric.

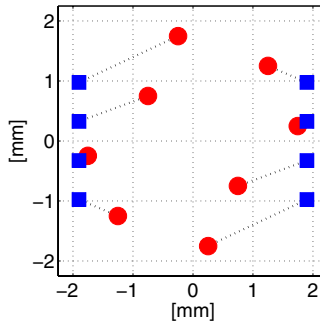


**Figure 3.53:** *Interposer pad arrangement with component pad assignments of minimal total trace length for a  $\mu$ SOP package (■: center of component pads, ●: interposer pads)*

Note that the computational amount for optimization of an application-independent interposer rises rapidly by  $(n!)^2$ .

### 3.6.4. Footprint area of an interposer

The routing structure on an interposer depends on the component package (i.e. component pitch) and the fabric wire pitch. Further, either component pitch or fabric pitch directly defines the minimum interposer area  $A_{min}$ . This

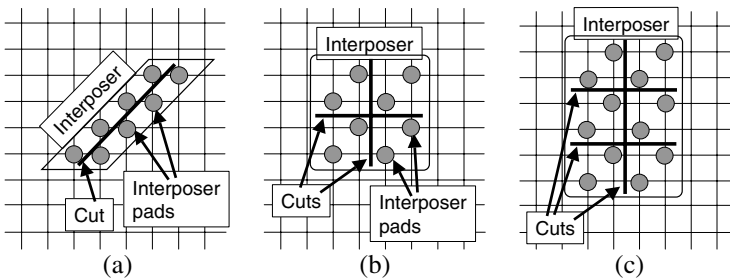
relation is formulated in (3.8) where  $n$  is the number of interposer pads,  $p_{tex}$  is the fabric wire pitch and  $A_{comp}$  is the area occupied by the component package.

$$A_{min} = \max [A_{comp}, (n \cdot p_{tex})^2] \tag{3.8}$$

### 3.6.5. Reduction of occupied interposer area

Specific cuts in the fabric can reduce the occupied area of an interposer when  $(n \cdot p_{tex})^2 > A_{comp}$ . Figure 3.54 shows three examples along with the corresponding formula for the reduced area  $A_{ip}$ . Note that only the interposer pads are drawn in the Figure. The symbols in the given formulas have the the same meaning as in Formula (3.8). Formula (3.9) determines then the occupied area  $A_{min}$  of an interposer.

$$A_{min} = \max [A_{comp}, A_{ip}] \tag{3.9}$$



$$A_{ip} = n \cdot p_{tex}^2$$

$$A_{ip} = \left(\frac{n}{2} \cdot p_{tex}\right)^2$$

$$A_{ip} = \frac{n}{2} \frac{n}{n_c + 1} \cdot p_{tex}^2$$

$n_c$ : # of cuts in horizontal direction

**Figure 3.54:** Examples of interposers with cuts in the fabric to reduce the occupied area

A diagonal cut as in Figure 3.54(a) delivers the smallest area  $A_{ip}$  for all  $n$ . However, the larger the number of pads is, the longer the interposer becomes while its width stays constant.

The principle in Figure 3.54(b) is recommended to achieve a quadratic or nearly quadratic interposer shape. Notice that at least a horizontal and a

vertical cut are necessary to obtain an area reduction in comparison to an interposer without cuts in the fabric. If the number of pads cannot be divided into even groups by cuts, the expression  $n/2$  in  $A_{ip}$  extends to  $n/2 + 1$ .

Figure 3.54(c) finally is the continuation of the principle in Figure 3.54(b). A single cut must be kept in either the horizontal or the vertical direction. Otherwise, certain pads are not electrically accessible anymore.  $c_n$  denotes the number of cuts in the direction with more than one cut (in the figure: horizontal cuts). The limit is achieved when a cut is placed between every pad. Such a case corresponds to Figure 3.45(a) and the pad area  $A_{ip}$  coincides with that one in Figure 3.54(a). Again, the higher the number of pads is, the longer the interposer becomes.

As soon as cuts are introduced in the fabric, the escape directions for the wiring of an interposer pad become limited to 2 directions (case a+b) or even to 1 direction (case c).

### 3.6.6. Further considerations

#### Interposer manufacturing

Vias/interposer pads must be plated with gold to ensure a oxidation-free electrical connection with the conductive adhesive. Vias of an interposer that only function as vias should be tented such that probable shorts with the fabric can be avoided.

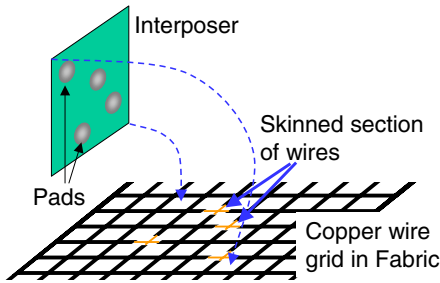
#### RF performance

A final note is given regarding RF behavior of the interposer. If no cuts are placed in the fabric, signal lines possess open ends of unknown lengths that introduce reflections. Thus, high frequency applications are limited. On the other hand, dedicated cuts in the fabric close to the interposer pad can relax this problem.

### 3.6.7. Assembly of an interposer

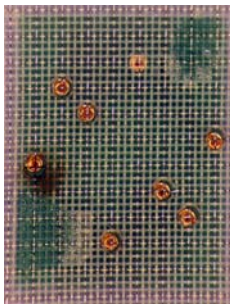
Figure 3.55 illustrates how an interposer is connected to the fabric. As easily can be seen, no cuts are necessary anymore and mechanical stability of the fabric is ensured.

Figure 3.56(a) shows a laser ablated fabric with interposer underneath. The wire coating and the polyester yarn is removed at each laser treated point in the fabric.

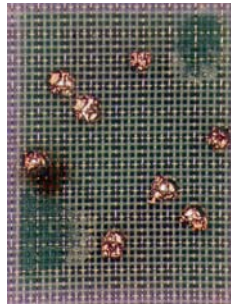


**Figure 3.55:** *Mounting of an interposer to the fabric*

Figure 3.56(b) depicts the same interposer connected to the fabric. The conductive adhesive establishes the electrical connection between the interposer pads and the copper wires in the fabric.



(a) Laser ablated fabric with interposer underneath



(b) Interposer connected to the fabric

**Figure 3.56:** *Interposer and fabric assembly*

For a better understanding, Figure 3.57 presents a cross-section through an interposer. The cut has been placed where an interposer pad connects to the fabric.

### 3.6.8. Inductivity of an interposer connect

The inductance of a  $33\mu\text{m}$  bond wire ranges from  $2 - 4.4\text{nH}$  [8, 69] for lengths of  $2 - 4\text{mm}$ . In contrast, a  $30\text{mil}$  solder ball of a BGA packages only features about  $0.2\text{nH}$  [69]. For comparison reasons, an interposer connect is

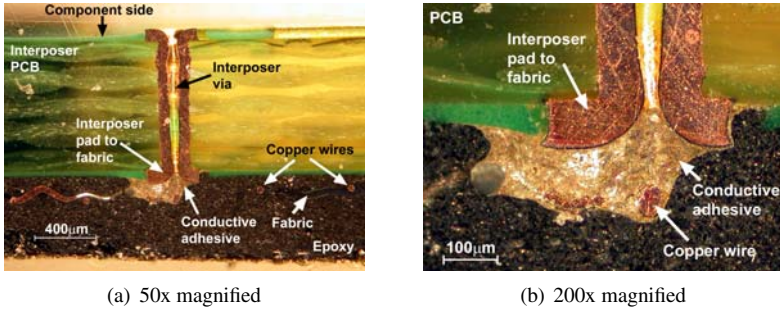


**Figure 3.57:** Cross-section through interposer-to-fabric connect

modeled as shown in Figure 3.58 and simulated with *FastHenry* [50]. The copper wire in the fabric is kept short ( $0.5\text{mm}$ ) and the trace on the interposer is  $3\text{mm}$  corresponding to an average length. The via through the interposer has a height of  $1\text{mm}$ . Notice that the interposer PCB is not shown here. The simulations revealed an inductivity of  $2.9\text{nH}$  for such an interconnect. A longer copper wire would add about  $1.05\text{nH}/\text{mm}$  due to self-inductance.

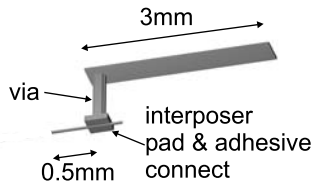


**Figure 3.58:** Simulation model of interposer connect

Thus, the inductivity of an interposer connect lies in the same region as a bond wire connects.

Further, the parallel wires within the fabric couple to each other. Simulations are performed in *FastHenry* to obtain the mutual inductances among adjacent wires within PETEX. Figure 3.59 shows the simulation model and the mutual inductance of one wire to its adjacent wires. As expected, the simulations indicate an exponentially decaying coupling following the law of magnetic coupling.

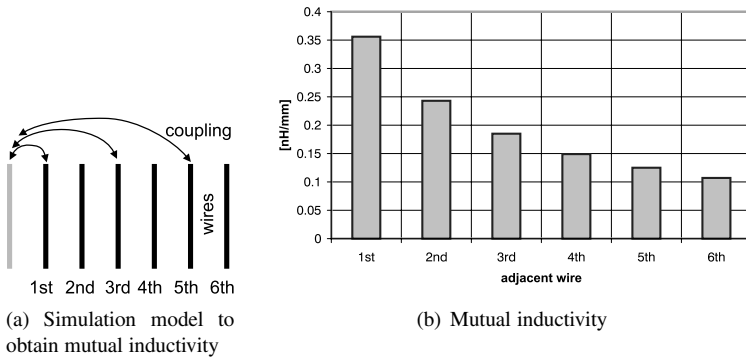


**Figure 3.59:** Mutual inductance among the wires within PETEX

### 3.7. Circuit protection tests

Interposers assembled on PETEX as well as textile vias are protected with epoxy resin.

In this section, the behavior of PETEX and the epoxy circuit protection is analyzed under tensile stress. The plain PETEX is tested until breakage in warp and weft direction while monitoring its electrical conductivity. The goal is to determine whether the woven polyester yarn frame of PETEX protects the copper wires from breakage.

Secondly, a two-pad interposer is assembled on the fabric and encapsulated. The fabric with interposer is then strained until breakage. The question is 'what breaks first', the fabric itself or does the interposer pop off.

Apart from that, the epoxy encapsulation on the fabric is exposed to a humidity of 85%RH at 85°C. The creepage current is then measured to determine moisture penetration and sealing of the epoxy.

An overview of mechanical test for fabrics is given by Saville [81].

#### 3.7.1. Tensile stress test on fabric

Several fabric samples of 44mm width are analyzed in a tensile test machine<sup>6</sup>. The sample lengths in warp and weft direction feature 10cm. The resistance of the copper wires in the fabric is observed during the tests with the internal ohmmeter of the Agilent 34980A switch unit [4]. Depending on the fabric

<sup>6</sup>Brand: Zwick Roell

sample, 20 up to 70 wires could be contacted in parallel to measure resistance. Figure 3.60 depicts the measurement setup.



**Figure 3.60:** *Tensile test setup. The resistance of the copper wires in PETEX is monitored during the tensile tests.*

All tensile tests are performed at room temperature. Figure 3.61 shows the obtained measurement curves. The fabric breaks at about the same force at an elongation of 32% and 23% in warp and weft direction, respectively. Whereas the copper wires break while the fabric (polyester) still yields in warp direction, the polyester yarns break while the copper wires are still intact in weft direction. This effect originates from the different stresses in warp and weft direction during manufacturing according to Sefar Inc.

The measured resistance change is caused by yielding and breakage of the copper wires. Yielding leads to constriction of the wires that results in a steadily increasing resistance. Breakage results in a sudden change of the resistance. Notice the steps in the resistance curve corresponding to the breakage of single copper wires.

It is interesting to mention that the copper wires do not break at the tear edge of the polyester at a first stage. Instead, the copper wires start breaking at random locations within the fabric as can be seen in Figure 3.62. Corresponding to the stress-strain figures, this effect is much stronger in warp direction.



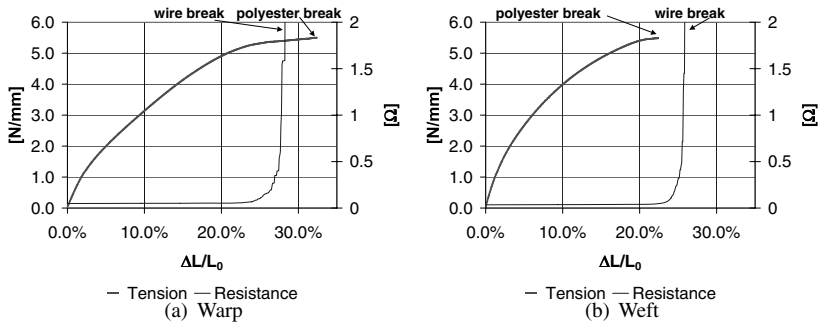


**Figure 3.61:** *Stress-strain diagram of PETEX including measurements of electrical resistance change of the copper wires*

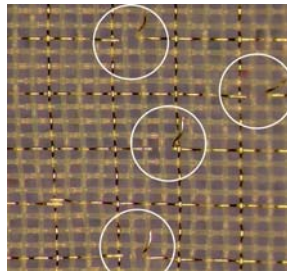


**Figure 3.62:** *Broken copper wires within the fabric due to tensile stress (warp direction)*

### Tensile stress on fabric with interposer

The same tensile tests are conducted with PETEX samples including an interposer encapsulated in epoxy. In fact, the interposer just forms a bridge between two wires. The conductivity between these two wires is then monitored during the tests. Further, we are interested whether the interposer weakens the fabric.

Most samples break right at the edge of the interposer. However, the interposer sometimes unhinges of the fabric before breakage as can be seen in Figure 3.63.

The measured curves in Figure 3.64 behave similar in warp and weft as the plain fabric. The breakage occurs about 5 – 10% earlier in elongation

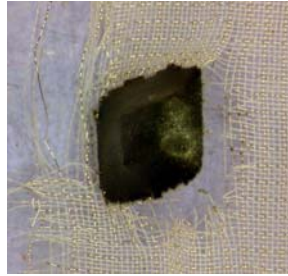


**Figure 3.63:** *Unhinged interposer during tensile tests*

compared to the plain fabric. The difference originates from the interposer assembly as well as from the different sample dimensions. A fabric sample with interposer has a width of 50mm and a length of 185mm.

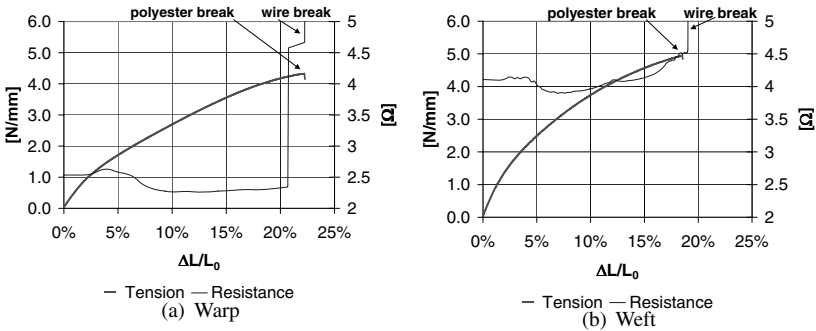


**Figure 3.64:** *Stress-strain diagram and electrical resistance change of PE-TEX with assembled interposer*

**Results and conclusions**

Table 3.8 lists the measured tensile strengths and elongations of PETEX with and without interposer. The numbers in bold face indicate the weaker component in the tests, either the polyester (PET) or the copper wire.

In weft direction, the copper wires even break after the polyester yarns. Secondly, assembled and encapsulated electronics slightly weakens the fab-

**Table 3.8:** *Tensile strength of PETEX*

	Plain PETEX			PETEX with interposer		
	Tensile strength [ <i>N/mm</i> ]	Elong. at break PET [%]	Wire [%]	Tensile strength [ <i>N/mm</i> ]	Elong. at break PET [%]	Wire [%]
Warp	5.5	32.0	<b>27.0</b>	4.3	22.5	<b>21.0</b>
Weft	5.5	<b>23.0</b>	26.0	4.9	<b>18.0</b>	18.5

ric. Breakage in the fabric occurs right at the edges of an encapsulation since the stiff epoxy resin causes a scoring guide.

The yield strain of polyester is about 1%. Almost total length recovery occurs even after an elongation of 10% [43]. Stresses above these values are not expected in daily life. Hence, the polyester yarn frame in the fabric protects the copper wires from tensile stresses.

### 3.7.2. Moisture absorption of epoxy encapsulation

The moisture absorption measurements determine the seal effect of the epoxy encapsulation. We want to know if such an encapsulation is suitable to protect electronics from moisture. The datasheets for the polyester material of PETEX and the epoxy resin [33] give only limited information on their behavior in moisture, *viz* 0.4% moisture content at 20°C, 60%RH and 0.15% maximal moisture content, respectively.

In a first step, we determine the exposure time to humidity until moisture saturation within the encapsulation is achieved. In a second step, we actually measure the creepage current for two climates, 30°C, 60%RH and 85°C, 85%RH, respectively.

#### Exposure time until saturation

The exposure time to humidity until water saturation occurs has not been known for the epoxy resin and the polyester previously. Literature [18, 97] gives imprecise numbers. Therefore, measurements to determine this time have been performed in advance using similar capacitive measurement techniques as described in [95]. In short, plate capacitors with PETEX as dielectric between the plates have been manufactured and encapsulated in epoxy resin. A plate has dimension  $5 \times 5 \text{ mm}^2$ . Some capacitors have been left unprotected. The capacity has been measured with the HP4192 impedance ana-

lyzer [6].

Accumulated water between the plates causes a raised capacity. We have measured the time until the capacity stopped increasing. Our samples show saturation after about 80 hours exposure to  $85^{\circ}C$ ,  $85\%RH$ .

### Creep measurement specimens

Troyk *et al.* [97] suggest a comp pattern to measure moisture penetration in chip packages. Following their approach, a comb pattern is built within PETEX as depicted in Figure 3.65. The wire coating under the epoxy protection has been removed in advance simulating electrical connects to an interposer. Different specimens, with and without epoxy protection, have been prepared as listed in Table 3.9. The fabric size of all specimens is  $4x4cm^2$ .

All feeding cables have been equipped with a teflon (PTFE) cladding in order to minimize measurement errors. Since literature does not agree about the use of shielded or unshielded cables<sup>7</sup>, specimens in both variants have been prepared.

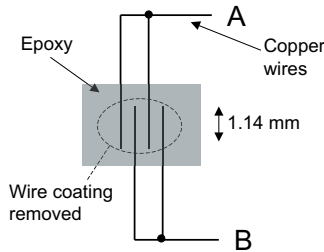


**Figure 3.65:** Utilized comp pattern for creep measurement in PETEX

Specimens 1+2 of Table 3.9 are shown in Figure 3.66. The comp pattern of Figure 3.65 is underneath the epoxy encapsulation in Figure 3.66(a). The same PETEX piece as in Figure 3.66(a) is located inside the metal shielding in Figure 3.66(b) and connected to the coax cables.

<sup>7</sup>Shielded cables reduce the noise caused by scattering fields compared to unshielded cables. On the other hand, the signal wires are tightly together in shielded cables introducing an potential parasitic creep among these wires.

**Table 3.9:** *Specimens for creep measurements*

Specimen	Comment	Epoxy Protection	Shielding
1	without shielding	1x1cm <sup>2</sup>	
2	with shielding	1x1cm <sup>2</sup>	✓
3	without epoxy		
4	plain fabric		

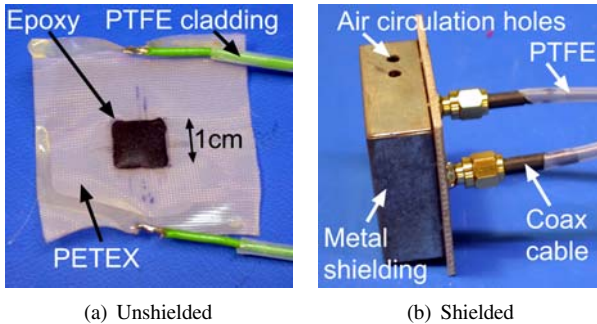


**Figure 3.66:** *Specimen 1+2 of Table 3.9 to measure moisture penetration*

**Creep measurement setup**

The creep is measured with a Keithley 485 picoampere meter [51] at 50V using an Agilent E3631 power supply [5]. The measurements are performed in a Heraeus HC4015 climate chamber. The measurement setup is shown in Figure 3.67.

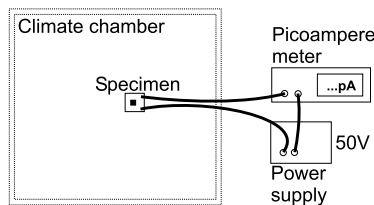


**Figure 3.67:** *Setup for moisture penetration measurement*

First, the climatic has been stabilized at 30°C, 60%RH for one week. Af-

ter that, temperature and humidity have been elevated to  $85^{\circ}\text{C}$ ,  $85\%RH$  for two weeks. These climates correspond to the IPC/JEDEC J-STFD-020B level 1 standard for *Moisture/Reflow Sensitivity Classification for Non-hermetic Solid State Surface Mount Devices*.<sup>8</sup>

### Creep measurements

Figure 3.68 depicts averaged creep curves of specimen 2. Its characteristic of an exponentially decaying curve is typical for polymers [71, 97] in general. Table 3.10 lists the maximal end values of the decayed creep current of the specimens.

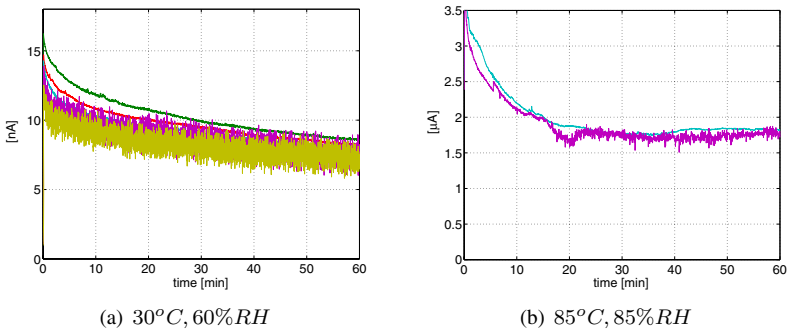


**Figure 3.68:** Specimen 2: creep curve of repetitive measurements at 50V

**Table 3.10:** Creep measurement results

Specimen	Maximal current @ 50V	
	$30^{\circ}\text{C}$ , $60\%RH$	$85^{\circ}\text{C}$ , $85\%RH$
1	$700\text{pA}$	$4.0\mu\text{A}$
2	$35\text{nA}$	$3.0\mu\text{A}$
3	0	$1.3\mu\text{A}$
4	0	$250\text{pA}$

<sup>8</sup>The Pressure Cooker Test (PCT) or Autoclave test [90] has not been applied since the conditions of  $121^{\circ}\text{C}$ ,  $100\%RH$  at  $2\text{atm}$  are far off the normal operation point of the SoT. Secondly,  $121^{\circ}\text{C}$  is just at the edge of the maximum allowed temperature for polyester.

**Conclusion**

As expected, the epoxy encapsulation lowers the insulation resistance as compared to air. The maximal current occurs in specimen 1 at  $85^{\circ}C$ ,  $85\%RH$ . This current corresponds to a resistance of  $12.5M\Omega$ .

No significant difference could be noticed between shielded and unshielded specimens. The measurement difference is probably so small that it is occluded by the rather high creep in specimens 1+2.

The wire coating in the plain fabric is robust against moisture as long as it is not damaged. No creep current can be measured at  $30^{\circ}C$ ,  $60\%RH$  and only a minor current appears at  $85^{\circ}C$ ,  $85\%RH$ .

Depending on the electrical application, the occurring creep in the epoxy encapsulation might already be unacceptable at the given climates. Thus, the epoxy resin is subject for further optimizations regarding insulation properties.





# 4

## Textile Routing\*

*After having shown in Chapter 3 that the PETEX fabric substrate as well as the embedded copper wires possesses promising properties for electrical signal transmission we focus on the design of circuits on fabrics in this chapter. We discuss textile-specific constraints for component placement and routing. Some of these constraints might already be supported by EDA<sup>1</sup> tools and others probably need modifications, e.g. macros. We also present two methods to implement the cutting step of wires into the design process. Our motivation is to utilize standard EDA tools with few modifications for fabric substrates. Finally, a strategy for reliable signal and power supply wiring is proposed.*

---

\*partially based on [60]

<sup>1</sup>Electronic Design Automation

## 4.1. Introduction

This chapter presents design aspects for implementation of circuits on fabrics with a wire grid structure such as in PETEX. We point out specific design rules and constraints for a textile routing structure.

First, the component and interposer placement is addressed in order to preserve drapability of the fabric. Second, the wire cuts introduced in Section 3.5 are discussed with regard to the textile layout and two methods to place them are described. Further, a routing design flow is proposed for the signal and power wiring in the fabric.

## 4.2. Component placement

Among the usual constraints of circuit layouts such as having short connections and few vias, an important new requirement is introduced for fabrics. Even though placement of electrical components on fabrics results in rigid spots as much drapability as possible should be maintained. An approach is to place components and interposers in a quadratic grid. Such a grid is shown in Figure 4.1 for an example with 9 equal interposers. A maximum number of folds and folding directions can be achieved with such an arrangement while having interposers with minimal distances to each other. Eventually, best drapability is ensured. The components and interposers should be small and of equal size. The grid spacing is determined by the longest edge of a component/interposer indicated with  $a$  in Figure 4.1. Hence, the grid spacing would be at least  $2a$ . As result, a circuit with  $n^2$  components placed in such a manner with  $n$  components in a row features  $6(n - 1)$  possible folds.

## 4.3. Textile routing implementation

In contrast to PCB layouts, a textile wiring must be entirely perpendicular determined by the structure of the fabric. Such a layout can be enforced by adjusting the design rules of EDA tools [9, 22] or by the user. Favorably, different layers for horizontal and vertical traces are chosen to enforce the placement of vias at each change of trace direction. These vias will be the *textile vias* in the manufacturing process later on.

Additionally, proper cuts need to be placed around the vias avoiding shorts with other signals. Two methods for this step will be discussed in the subsequent sections. It will be shown how this *cut step* is integrated in the existing EDA process.

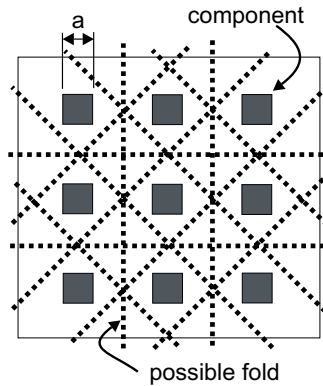


**Figure 4.1:** Placement of 9 components on a fabric that ensures drapability

#### 4.3.1. Method 1 for 'cut step'

In the first approach, we need to define three types of vias including their  $90^\circ$  turns as shown in Figure 4.2. Their shape resembles thermal vias. Each trench of a via represents a cut in the fabric whereas the via drilling hole defines the electrical connection of wires. Further, the definition of a power plane in the layer stack-up is essential.

One of the vias in Figure 4.2 must be placed at each change of trace direction in the layout process. The via and its orientation must be chosen such that no unwanted connections to other electrical nets occur. Secondly, the vias must be placed in the wire grid of the fabric. Interposer pads need to be replaced by vias. Finally, only the Gerber file of the power plane and of the via drilling holes will be needed for manufacturing. The power plane file defines the cuts whereas the drilling defines the positions for the laser skinning, for the adhesive drops and for the protective epoxy. Figure 4.3 illustrates the first approach whereby the gray lines indicate the grid of copper wires.

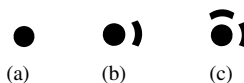


**Figure 4.2:** Three via definitions in EDA tool for 'cut step' method 1 (Section 4.3.1)

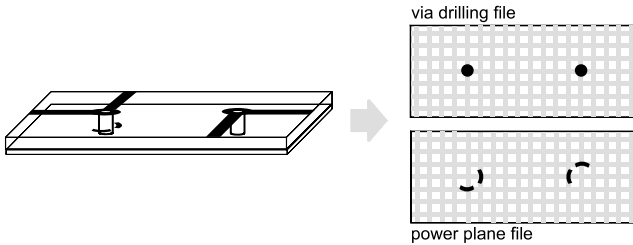


**Figure 4.3:** Necessary manufacturing layers for 1st method (Section 4.3.1)

#### 4.3.2. Method 2 for 'cut step'

The second approach is similar to the first one, but no attention to the choice of vias must be paid and no power plane is necessary. It is based on the IPC-D-356B [45] file generated by EDA tools such as Altium DXP and Cadence Allegro [9, 22]. This file contains all information about via/pad positions in the layout and the nets they belong. A script has been implemented that reads this file and generates a Gerber file with the vias and pads. It then analyzes the vias/pads positions and generates a second Gerber file containing the positions and lengths of the cuts. The algorithm is explained in more detail in the next subsection. The two Gerber files represents the manufacturing data as depicted in Figure 4.4.

#### Implemented algorithm for placement of the cuts

The algorithm of the script goes through the list of vias and pads. It selects a via/pad and perpendicularly seeks in all four directions in the plane until it hits another via/pad, a cut or the border of the board. In case of a via/pad, the algorithm checks whether it belongs to the same net. If not, a cut of appropriate length is placed at the appropriate location in order to electrically separate them. If a cut or the border is hit, the selected via/pad is already insulated and nothing needs to be done. After that, the next via/pad in the list is selected and the algorithm is iterated again. The principle of this algorithm is shown in Figure 4.5(a) where the arrows indicate the seek direction and the letters denote the electrical nets the via/pad belongs to. Figure 4.5(b) expresses the result with the added cuts after iterating over pad A.

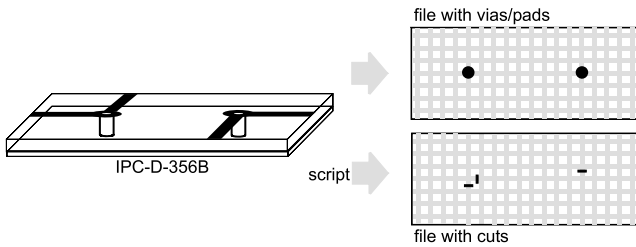


**Figure 4.4:** Necessary manufacturing layers for second 'cut step' method

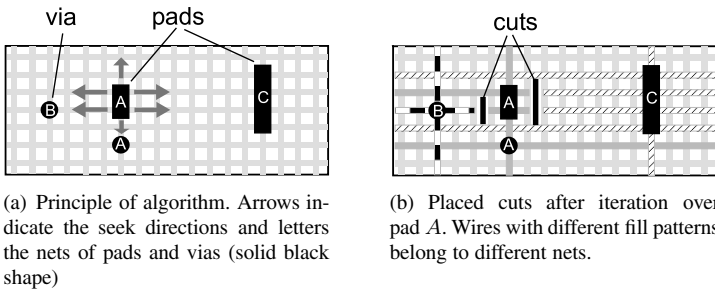


**Figure 4.5:** Principle of 'cut step' method 2 (Section 4.3.1)

### Discussion of method 2

Main goal of the second method is to preserve the mechanical strength of the textile. It analyzes the structure and places cuts only when necessary. In comparison, method one places cuts at all bendings of a signal path, which is not always needed. This drawback is, however, relieved when vias and pads are cast in epoxy later on. Nevertheless, approach one is rather error prone since the user has to choose the vias for the right cuts whereas the cuts are placed automatically in approach two.

Approach two produces open-ended traces in the electrical path leading to worse electrical performance, though this effect is not severe at low frequencies. Besides, the algorithm for method two can easily be changed so that cuts are always placed similarly to approach one.

Method 2 has already been successfully applied to several projects. An example for a blinking LED is shown in Figure 4.6.

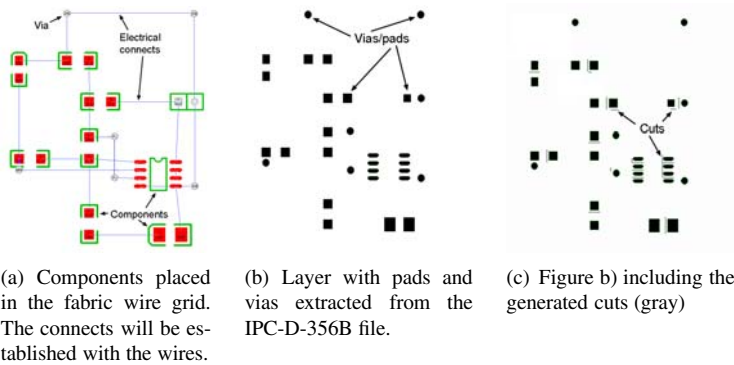


**Figure 4.6:** Example of 'cut step' method 2 for a blinking LED on PETEX

### 4.3.3. Routing considerations

Although PETEX is a precision fabric, its geometry is still about 10 times less accurate than a PCB, e.g. FR4. Thus, the localization of a specific wire within the fabric is critical over longer distances. A work-around to relax this problem proposes a strategy to use single wires for local routing structures and several wires in parallel for global routing. A misalignment by few wires is then not critical anymore. Of course, such a strategy consumes more space in the fabric.

An alternative approach by visually tracing each single wire within the fabric is presented in Appendix C.

## 4.4. Signal wiring

In this section, we address three specific signal types, which can occur in electrical circuits. They are discussed with respect to their implementation in fabrics.

- *Analog signals:* In order to avoid inducing noise due to stray fields, an analog signal should always be accompanied with a ground line. Thus, the area for induction of scattering fields is kept small and the signal is somewhat shielded from noise. Generally, analog lines should be kept short.
- *RF signals:* As soon as a signal line length exceed about  $1/10$  the wave-

length  $\lambda$  of its signal, controlled line impedances of the lines become important. For instance, a  $3GHz$  signal in air features a wavelength of  $10cm$ . For other dielectrics, the wavelength is even shorter. Discontinuities in impedances lead to reflections, odd modes and losses in general. Thus, wire line configurations as proposed in Chapter 3 are recommended for RF signals. RF signal lines should be kept short.

- *Power supply*: Since a copper wire in the fabric has a resistance of about  $15\Omega/m$ , the voltage drop along the wires must be considered in the routing design. Wires in parallel lower this resistance.

## 4.5. Routing strategy

After having discussed the implementation of a textile routing and aspects of some critical signals, a feasible routing strategy is proposed for a textile layout. Figure 4.7 depicts the iterative design flow of the textile routing process.

Explanations and comments to each box is given in the list below:

1. *Current & Voltage Budget*. The current consumption and supply voltage of each component and sub-circuit must be determined with the datasheets.
2. *Grouping of Components*. The components must be arranged in functional groups. Each group will be realized as an interposer later on. The grouping process must consider several aspects. The consumed area of the components of a group must be small; hence the interposer will be small. Secondly, the number of traces to other groups should be minimal in order to minimize the routing effort in the fabric. Note that a group with small area, but many connects to other groups artificially enlarges the interposer size due to the high number of interconnects to the fabric.
3. *Number of Power Lines*. The thin copper wires only allow a current of less than  $10mA$  (according to AWG46). To each group, the number of power lines must be assigned in order not to exceed this current per wire. Notice as well that the current of each group accumulates in the power supply wiring and at the battery plug. If the number of power lines exceeds a given limit, the components must be regrouped.
4. *Maximal Length of Power Lines*. The DC resistance of the copper wire causes a voltage drop in the power supply. The voltage requirements

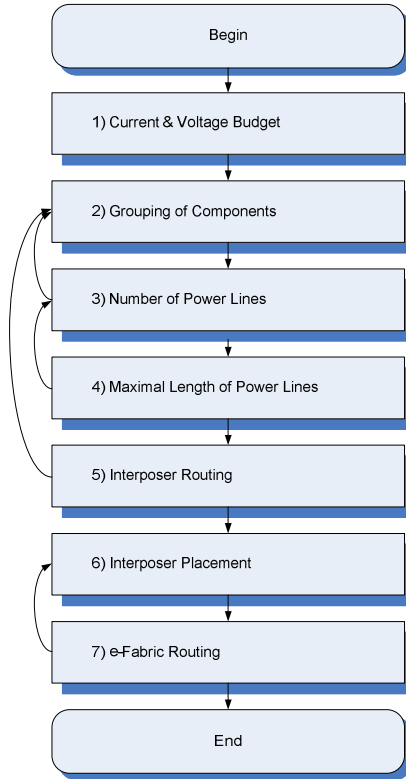


**Figure 4.7:** Textile routing process flow

of each group determine its maximal allowed power line length (VCC and GND) to feed the circuit. Figure 4.8 may help to determine the maximum wire length as well as the number of wires. The maximum length  $L_{max}$  is given by Formula (4.1) where  $N$  is the number of wires,  $\Delta V_{max}$  the allowed voltage drop,  $I_{Group}$  the required current for a group and  $R_{Wire}$  the wire resistance per meter.

$$L_{max} = \frac{\Delta V_{max} \cdot N}{I_{Group} R_{Wire}} \quad (4.1)$$

Consider the current accumulation in the wires, especially at the power supply and power plug. If the power lines need to be longer than its



maximal voltage drop allows, the number of power lines must be increased to lower the DC resistance.

5. *Interposer Routing.* The components within a group are routed forming the interposer. Secondly, the interconnect pads towards the fabric are placed orthogonally such that no cuts or only few cuts in the fabric are necessary. The routing and the pads towards the fabric will determine the final size of the interposer. If the interposer becomes too large, the components must be regrouped.
6. *Interposer Placement.* The interposers are placed such that drapability of the fabric is preserved as well as the routing effort within the fabric is minimal.
7. *e-Fabric Routing.* The interconnecting structure to the interposers is routed within the fabric. Avoid current (ground) loops and add cuts if necessary. Make sure that the routing structure preserves the wire pitch of the fabric. Consider transmission line configurations for RF signals.

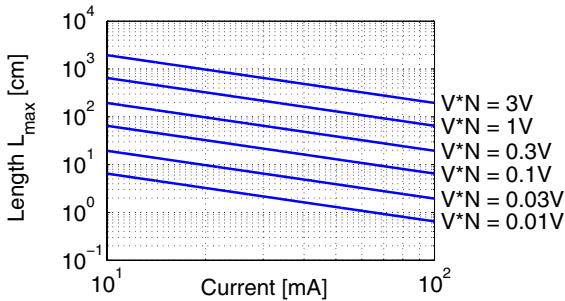


**Figure 4.8:** Maximum wire length as function of current, voltage and number of wires

#### 4.5.1. Routing strategy applied to the Fabric Integrated Wireless Temperature Sensor

This routing strategy and design process has been applied to the *Fabric Integrated Wireless Temperature Sensor* presented in Chapter 2. The corresponding results are given in Table 4.1. The current distribution from battery connector to the circuit is looped the following way: *Battery connector* → *Bluetooth* →  $\mu C$  → *Amplifier* → *Current Source*.

**Table 4.1:** Number of power/ground wires & maximal power supply wire lengths for the Fabric Integrated Wireless Temperature Sensor (Chapter 2)

Group	$I_{Group}$ [mA]	$V_{min}$ [V]	# of wires	$L_{max}$ [m]	$\Delta V_{max}$ [V]	Interposer size [mm <sup>2</sup> ]
Current src	2.55	2.7	1	22.9	0.9	11 x 10.3
Amplifier	0.20	2.7	1	21.2	0.9	8 x 10
$\mu$ C	0.35	2.0	1	33.5	1.6	8.5 x 9.7
Bluetooth	40.0	3.0	4	3.6	0.6	13.3 x 14.2
Battery con.	43.1	3.6	5	-	-	10 x 13.5
Process step	(1)		(3)	(4)		

$I_{Group}$  and  $V_{min}$  are obtained in process step (1) of the process flow in Figure 4.7. The number of wires result from step (3) and the maximal power wire length  $L_{max}$  and the maximal voltage drop  $V_{max}$  are determined in step (4).

#### 4.6. Routing constraint summary

A short overview of the routing rules and constraints in fabrics such as PE-TEX is summarized below.

- Components/Interposer must be placed in a quadratic grid.
- Interposer pads and vias must be aligned to the wire pitch within the fabric.
- A perpendicular routing must be ensured.
- A via needs to be placed at each change of trace direction.
- There are no ground/power planes available.
- Wire configurations with controlled impedances should be utilized for RF signals (see Section 3.3.1).
- The rather high resistance of thin copper wires must be considered, especially for power supply nets.
- A script according to method 2 should be applied to ensure reliable insulation of the electrical nets (Section 4.3.2).

# 5

## Wireless Connection Technology in Fabrics\*

*This chapter addresses textile Bluetooth antennas for Wireless Personal Area Networks (WPAN). Four antenna variants and their materials are discussed along with different manufacturing technologies. The antennas are electrically characterized using  $S_{11}$  and radiation pattern measurements. Additionally, the antenna performance under bent conditions is analyzed.*

---

\*based on [62]

## 5.1. Introduction

In this chapter, four purely textile patch antennas are presented for Bluetooth applications [19] in wearable computing using the frequency range at  $2.4GHz$ . We want to know how purely textile antennas behave and what effects bending of the antenna induces.

The fundamental composition of a patch antenna is shown in Figure 5.1. More information about antennas including an overview of antenna specific terms is given in [20].

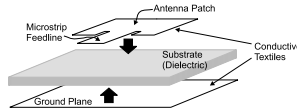


**Figure 5.1:** *Composition of a patch antenna with microstrip feedline*

The four manufactured antennas differ in the deployed materials and in the antenna polarization. All of them feature a microstrip line as antenna feed. Two of the four antennas have linear polarization and two of them have left-handed circular polarizations (LHCP). A manufacturing process has been developed that guarantees unaffected electrical behavior of the individual materials when composed to an antenna.

The flexible nature of the antennas allows embedding into clothing as depicted in Figure 5.2(a). Flexibility is important since bending radii as small as  $10mm$  can occur in garments along the body, especially around joints. Figure 5.2(b) qualitatively shows the curvature distribution along the human body. The darker a region appears, the smaller the radius is. A curvature on a human body consists of a superposition of bends in arbitrary directions.

## 5.2. Patch antenna design approach

Targeting wearable applications, a planar structure of the antenna is favored as well as a planar antenna feed. Thus, we discarded probe feeds. Instead, we use microstrip feed lines. In the design of the microstrip antenna patches, transmission line model formulas (5.1) and (5.2) such as given in Balanis [13] have been applied for a rough estimate.  $f_r$  is the resonance frequency of the antenna and  $\Delta L$  is the extended distance of the principal E-plane. The correspondence of the formula symbols  $L$  and  $W$  to the actual antenna shape is shown in Figure 5.3. The truncated corners  $c$  in Figure 5.3 introduce circular polarization (in our case: left-handed circular polarization; LHCP). For fur-

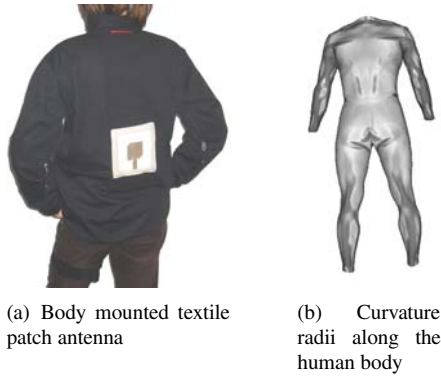


**Figure 5.2:** *Textile patch antenna on the human body*

ther information, please consult Balanis [13]. We will refer to these symbols later on in the chapter.

$$W = \frac{1}{2 \cdot f_r \sqrt{\mu_0 \epsilon_0}} \sqrt{\frac{2}{\epsilon_r + 1}} \quad [m] \quad (5.1)$$

$$L = \frac{1}{2 \cdot f_r \sqrt{\epsilon_{reff} \mu_0 \epsilon_0}} - 2 \cdot \Delta L \quad [m] \quad (5.2)$$

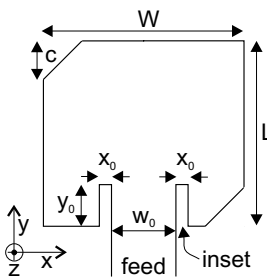


**Figure 5.3:** *Patch antenna sketch*

### 5.3. Related work

Fabric antennas presented by Salonen [79] and by Massey [68] are partially based on textiles possessing an inverted-F shape that results in a stiff structure (Figure 5.4(a)). Other textile antennas described by Tanaka *et al.* [89] and by Salonen *et al.* [78] are designed as rectangular patches with probe feed and linear polarization (Figure 5.4(b)). Antennas such as presented by Salonen *et al.* in [80] only utilize fabrics as substrate whereas the patches and ground planes are copper foils.

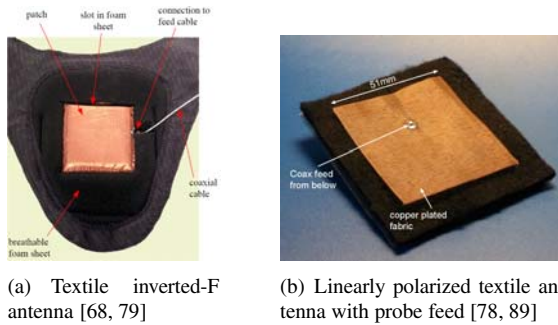


**Figure 5.4:** *Different textile antennas*

## 5.4. Textile materials

Inspired by the simple build-up of printed microstrip antennas, we adapted this technology to textiles. Therefore, we needed an electrically conductive fabric for the ground planes as well as for the antenna patches. Secondly, we required a fabric substrate with constant thickness and stable permittivity. The composition of a patch antenna is given in Figure 5.1.

In this section, we first study the electrical properties of two variants of conductive fabrics. Secondly, a felt and a spacer fabric are discussed as dielectric for the fabric Bluetooth antennas.

### 5.4.1. Electrically conductive fabric

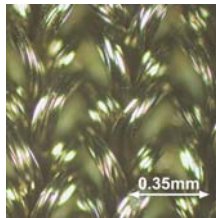
Among the many electrically conductive fabrics, we choose two variants for further investigations of their electrical properties:

**Table 5.1:** *Properties of conductive knitted and woven fabric*

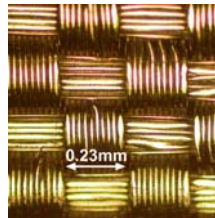
Property	Knitted (1)	Woven (2)
Fabric thickness	$0.55\text{mm} \pm 10\%$	$0.15\text{mm}$
Yarn polymer	Polyamide	Polyamide
Yarn pitch	$0.35\text{mm}$	$0.23\text{mm}$
Fibers per yarn	6	12
Weight	$180\text{g}/\text{m}^2$	$72\text{g}/\text{m}^2$
Plating	Ag	Ni / Cu / Ag
Sheet resistance	$< 1\Omega/\square$	$0.02\Omega/\square$
Equivalent Ag thickness	$16.3\text{nm}$	$815\text{nm}$

1. A silver plated knitted fabric from Statex [88].
2. A silver-copper-nickel plated woven fabric from Statex [87].

Table 5.1 states the properties of the two fabrics. In the last row, the table also gives the equivalent thickness of a pure silver foil to achieve the conductivity of the fabric. Pictures of the fabrics can be seen in Figure 5.5.



(a) Knitted fabric (1), P130 [88] ( $\uparrow y, \rightarrow x$ )



(b) Woven fabric (2), Nora [87]

**Figure 5.5:** *Electrically conductive fabrics*

The two fabrics are discussed in detail in the following subsections.

Note that the fabrics can only be shaped with finite precision given by the yarn thickness. In fact, the yarn pitch virtually 'discretizes' the possible sizes of the conductive patches as illustrated in Figure 5.6.

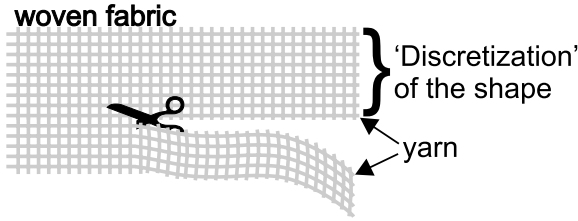


**Figure 5.6:** *Cuts parallel to the yarn direction 'discretizes' the feasible patch sizes*

#### 5.4.2. Silver plated knitted fabric (1)

##### Geometrical precision

The fabric consists of entirely plated polyamide fibers. Given by the nature of knitting, fabric 1 is viscoelastic featuring an approximated Young's modulus of  $E = 150kPa$ . The elasticity is a drawback during manufacturing of the antenna because precise shaping as well as assembly of the antenna without warpage is difficult. The antenna shapes manufactured finally achieved a geometrical accuracy of about  $\pm 0.5mm$ .

##### Resistance change due to stretch

Fabric elongations as they happen during bending of an antenna affect the sheet resistance of the conductive fabric. We measured this resistance change depending on elongation (and strain stress) in x- and y-direction. Figure 5.7 depicts a typical resistance change curve of the silver plated fabric. Since the knitting possesses a column-like structure (see Figure 5.5(a)), this resistance change behaves differently in the orthogonal axes (anisotropy). Elongation in y-axis has only minor effect on the resistance whereas the resistance increases significantly when elongated in x-axis. Both curves progress linearly for small elongations and flatten out for larger elongations.

#### 5.4.3. Silver-copper-nickel plated woven fabric (2)

The fibers of this fabric are plated before weaving resulting in a low electrical resistance (Table 5.1).

Compared to the knitted fabric 1, fabric 2 features low elasticity due to its woven structure (see Figure 5.5(b)). Thus, bending of a composed antenna is limited. The Young's modulus of about  $2.4GPa$  is mainly determined by the



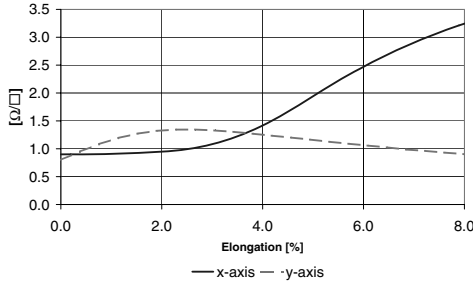


**Figure 5.7:** Sheet resistance change due to elongation of knitted fabric (1)

polyamide material of the yarn in fabric 2.

The edges of this fabric tend to fray easily due to the nature of woven fabrics. This effect can be minimized by using manufacturing techniques explained in Section 5.6. Antennas with geometrical accuracies of about  $\pm 0.15\text{mm}$  are feasible.

#### 5.4.4. Plating thickness

The targeted frequency range ( $2.4\text{GHz}$ ) features a skin depth of about  $1.3\mu\text{m}$  given by formula (5.3) where Ag plating is assumed.  $\delta$  is the skin depth,  $f$  the frequency,  $\mu$  the magnetic permeability and  $\sigma$  is the electrical conductivity. The skin effect increases the electrical resistance that causes additional losses. Moreover, the plating thickness of the fabrics is restricted to several hundred nanometers in order to maintain textile properties. This fact as well increases damping in the final antenna occluding the skin effect.

$$\delta = \frac{1}{\sqrt{\pi f \mu \sigma}} \quad [m] \quad (5.3)$$

#### 5.4.5. Textile substrates

The textile substrate provides the dielectric between the antenna patch and the ground plane (see Figure 5.1). The thicker the substrate and the lower the permittivity is, the larger the antenna patch becomes for a specific resonance frequency. The larger an antenna patch is, the less influenced is its antenna characteristic by absolute tolerances in geometry. Thus, we aim for substrates with thicknesses in the millimeter range.

We choose a woolen felt with a thickness of  $3.5\text{mm}$  and a polyamide spacer fabric with a thickness of  $6\text{mm}$  as substrates. The felt with a density

of  $1050g/m^2$  is mechanically more stable and harder to bend whereas the spacer fabric with  $530g/m^2$  is lighter and elastic due to its knitting-based structure. Further, the spacer fabric can easily be compressed as can be seen in Figure 5.8. A pressure of about  $25kN/m^2$  leads to a compression of  $3mm$ . Nevertheless, the fabric totally recovers after release of the load. Foam could be another alternative, though not considered in this chapter.

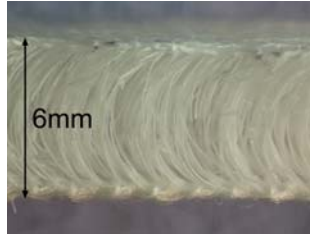


**Figure 5.8:** *Cross-section of spacer fabric substrate*

We use techniques explained in Appendix A.2 to extract the effective relative permittivity of the textile substrates and to eliminate impedance discontinuities of the measurement setup. This method utilizes scattering parameter measurements of two transmission lines of different lengths. For the measurements, we have built microstrip transmission lines in two lengths ( $12cm$  and  $18cm$ ) using the conductive woven fabric (2) and the substrate under investigation, i.e. the felt and the spacer fabric. From the extracted effective relative permittivity  $\epsilon_{r_{eff}}$ , we can conclude to the relative permittivity  $\epsilon_r$  of the substrate using formulas from microstrip line theory, e.g. given in Balanis [13].

The connection to the measurement equipment is established using the same adapters as for the final antennas themselves (see Figure 5.13(a) as well). The same measurement setup and methods are deployed as described in Subsection 3.3.2.

Finally, a relative permittivity  $\epsilon_r = 1.45 \pm 0.02$  for the felt and  $\epsilon_r = 1.14 \pm 0.025$  for the spacer fabric have been extracted at a frequency of  $2.4GHz$ . Extensive humidity measurements covering a range from  $20\%RH$  to  $80\%RH$  within a temperature range of  $25^\circ C$  till  $80^\circ C$  showed that permittivity variations are negligible compared to the measurement uncertainty. This result closely corresponds to the numbers given in [23] for the humidity effect on permittivity of air since both substrate permittivities are close to 1.

**Table 5.2:** *Designed antenna variants and materials*

Antenna name	Substrate	Substrate height	Conductive material	Polarization	Feed line $Z_0$
LF	felt	3.5mm	knitting (1)	linear	50 $\Omega$
CF	felt	3.5mm	knitting (1)	circular	50 $\Omega$
LS	spacer	6mm	knitting (1) & woven (2) *	linear	75 $\Omega$
CS	spacer	6mm	woven (2)	circular	75 $\Omega$

\* knitted antenna patch / woven ground plane

**Table 5.3:** *Dimensions of the four antennas including tolerances [mm]*

Dimension	LF	CF	LS	CS
$W$	64	44	58	47
$L$	49	51	53	57
$c$	0	8.5	0	8
$y_0$	13	8	14	9
$x_0$	1	3	3	3
$w_0$	14	14	14	14
Tolerance	$\pm 0.5$	$\pm 0.5$	$\pm 0.5$	$\pm 0.15$

## 5.5. Antenna design

This section presents the design of the four patch antennas regarding material choice, antenna geometry, feed line and insets. The mentioned symbols correspond to the symbols in Figure 5.3.

The applied materials for the four antennas (2 linearly and 2 circularly polarized) are listed in Table 5.2. The geometrical dimensions to the antennas are given in Table 5.3. The goal for the antennas is to satisfy the bandwidth specifications of Bluetooth [19] ranging from 2400MHz to 24.835MHz.

### 5.5.1. Antenna feed

We have chosen a 75 $\Omega$ -microstrip feed line for the spacer fabric since a 50 $\Omega$ -line would become about 28mm wide, leading to a disturbed radiation characteristic of the antenna. However, a 50 $\Omega$ -microstrip feed line has been used for the felt substrate with its higher permittivity. To avoid losses due to mismatch between feed line and antenna, we have applied commonly known techniques described by Chen *et al.* [101]. There, insets along the feed line

are incorporated into the antenna patch in order to adjust the antenna's input impedance (Figure 5.3). The width  $w_0$  of the microstrip feed to meet  $50\Omega$ - and  $75\Omega$ -line impedance, respectively, have been computed using the standard formulas given in Balanis [13] as well.

### 5.5.2. Antenna insets

During the design process and first implementations, we have noticed the importance of an accurate transition from microstrip feed line to the antenna patch. Whereas accuracies better than  $1\mu m$  are achievable in PCB manufacturing, tolerances for textiles lie in the range of  $0.5mm$  as explained in Section 5.4. Secondly, the feed to the antenna has microstrip configuration (MS), however, as soon as the insets begin, it more resembles a finite-width conductor backed coplanar waveguide structure (FW-CBCPW), i.e. a microstrip line surrounded with ground planes. Figure 5.9 shows the characteristic impedance of coplanar waveguides (CPW) with respect to the gap width between trace and these ground planes for the two textile substrates. In our context, the gap width of the CPW corresponds to the inset width  $x_0$  of the antenna. As expected, the impedance asymptotically approaches an upper bound given by the impedance of the microstrip line (MS), where the ground planes on the microstrip line side can be assumed as infinitely far away. A constant trace width of  $w_0 = 14mm$  has been assumed in Figure 5.9. The shape of the curve further implies that variations, e.g. imprecision in manufacturing, have bigger impacts on the impedance when the gap width is small. Figure 5.9 also indicates the impedance range of the feedlines due to manufacturing tolerances (see Section 5.4) for the four antennas. For instance, the CPW of the CS antenna features smaller tolerances than the CPW of the LS antenna since it is made of the woven fabric.

In conclusion, wide insets  $x_0$  smooth out the transition from microstrip feed line (MS) to CPW antenna inset regarding impedances. Secondly, the CPW impedance curve flattens out for wide insets that introduce higher robustness against dimensional tolerances due to manufacturing and deformation of the antenna.

## 5.6. Antenna manufacturing

First prototype trials have shown that composition of the conductive antenna patches with the dielectric substrate is critical. First of all, the dimensions of the patch must be retained while being attached to the substrate. Secondly, the attachment procedure must not affect the electrical properties of the patch,

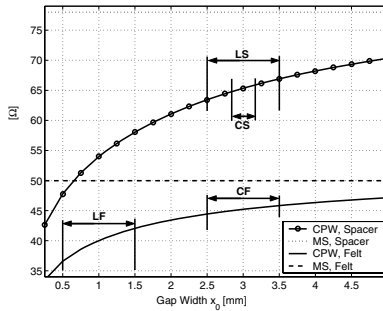


**Figure 5.9:** Characteristic impedances of CPWs w.r.t gap width  $x_0$  ( $w_0 = 14\text{mm}$ ) including manufacturing tolerances indicated by arrows

e.g. the sheet resistance. Thus, we run four experiments to find a feasible manufacturing approach for the patch antennas. The four approaches are explained in more detail below.

1. *Liquid textile adhesive (brand: Golden Fix).* Application of the liquid textile adhesive on conductive fabrics has shown soaking effects such that distribution of an evenly thin film of adhesives has been impractical. As a result, the adhesive acts as insulator among the conductive yarns. Because of the uneven distribution, electrical resistance has shown inhomogeneity and it can rise by a factor of ten at certain spots.
2. *Point-wise application of conductive adhesives.* A point-wise deposition of conductive adhesive in a  $1\text{cm}$ -spacing does not increase the sheet resistance. However, mechanical stability has been significantly worse compared to the textile adhesive (1). Secondly, accurate attachment of the antenna patch has not been ensured in terms of preserving geometry.
3. *Sewing.* Similarly for sewing, attention needs to be paid preventing warpage during the sewing process. Secondly, the seam spacing has been chosen to be  $< 2\text{cm}$  in order to minimize wrinkling. This behavior is illustrated in Figure 5.10. A wrinkling corresponds to uneven distances between the antenna patch and the ground plane resulting in distortion of the antenna characteristic.

Further, the sewing machine has stitched through both the patch and the ground plane of the antenna. Electrical measurements have revealed shorts between antenna patch and ground plane because the sewing

needle has pulled small conductive fibers from the patch through the substrate and has shorted them with the ground plane.

Besides, sewing cannot be used with the spacer fabric substrate since the high pressure of the sewing seam compressed the substrate permanently.

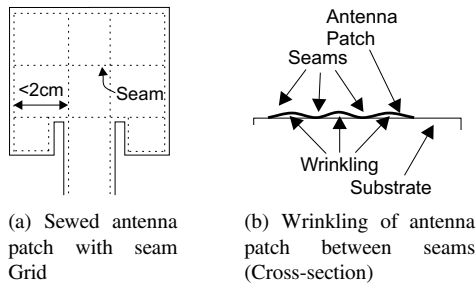


**Figure 5.10:** Sewed antenna

4. *Adhesive sheets, which are activated by ironing.* The adhesive sheets show the best results. It evenly deposits a thin layer on the conductive textile by ironing. Moreover, the adhesive only penetrates the surface of the conductive textile such that patch sheet resistance and substrate permittivity are not changed.

Nevertheless, maintaining of the geometrical dimensions needs to be guaranteed during attaching of the conductive antenna patch to the substrate. The knitted fabric is particularly challenging because it tends to curl. Therefore, we deploy a temporary stabilization and stiffening of the fabric until after its attachment. This is done by application of a water-soluble foil to the fabric. After ironing of the stiff, conductive fabric onto the substrate, the foil can entirely be dissolved in water.

From the mechanical point of view, the spacer fabric substrate too is elastic and stretchable because it is based on knitting as well (see Figure 5.8). By stretching the substrate, a knitted antenna patch (fabric 1) can be varied by several millimeters resulting in a big change of the antenna characteristic. As a consequence, we utilize a patch of non-elastic conductive woven fabric (fabric 2) for mechanical stabilization of the spacer fabric. In the case of the linearly polarized antenna with spacer fabric substrate (LS antenna), a woven ground plane has fulfilled our demands whereas we have had to apply the

woven fabric for both the antenna patch and the ground plane in the case of the circularly polarized antenna with spacer fabric substrate (CS).

Finally, we have achieved textile antennas with accurate shapes, good mechanical stability as well as stable and low sheet resistance by utilization of adhesive sheets and water-soluble foil. Two of the four antennas are shown for illustration in Figure 5.11.

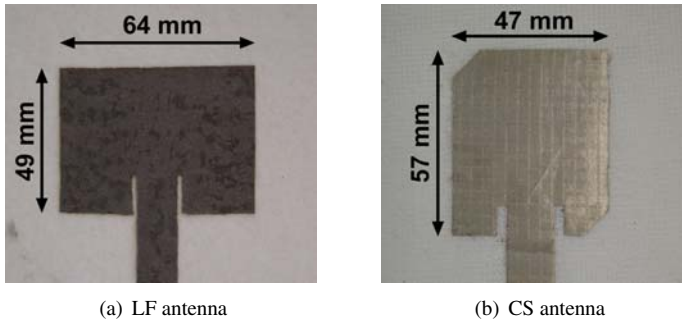


**Figure 5.11:** *Two of the four antennas manufactured (top view)*

## 5.7. Antenna simulation and measurement results

In this section, we compare the simulated antenna characteristics with the measurements conducted in the anechoic chamber. For the antennas, we show  $S_{11}$  (input reflection coefficient), radiation patterns and for the circularly polarized variants (CP) the axial ratio. Secondly, we carry out measurements with the antennas bent around cylinders (see Subsection 5.7.1) in order to investigate their potential behavior in wearable applications. Special attention has also been paid to the interconnect between measurement equipment and fabric antenna. Due to modeling of this connection using Ansoft HFSS, we could deduct its effect from the  $S_{11}$  measurements.

### 5.7.1. Antenna bending gauge

The bending gauge must not affect the measured antenna characteristic. Hence, we choose a thin-walled PVC (dielectric constant between 4 and 5) pipe with additional drilled holes such that the amount of air is maximized.  $S_{11}$  measurements of the antennas mounted on this pipe show minor differences to measurements on a solid pipe proving that the PVC pipe minimally

effects the antenna characteristic. Secondly, by using pipes in contrast to just folding the antennas as conducted by Tanaka *et al.* in [89], we can guarantee a well-defined bending radius and therefore reproducibility.

The radii for bending are chosen to be  $37.5\text{mm}$  and  $100\text{mm}$  for radiation pattern measurements, respectively. These radii are supposed to approximately correspond to the diameters of a small upper arm and a thick thigh. Additional bending radii are used in the  $S_{11}$  resonance frequency measurements.

In the following, only radiation pattern measurements conducted with the  $37.5\text{mm}$  bending radius are presented since this radius has a larger effect on the antenna characteristic than the  $100\text{mm}$  radius. Figure 5.12 shows the bending gauge ( $75\text{mm}$  diameter) used in the radiation pattern measurements.

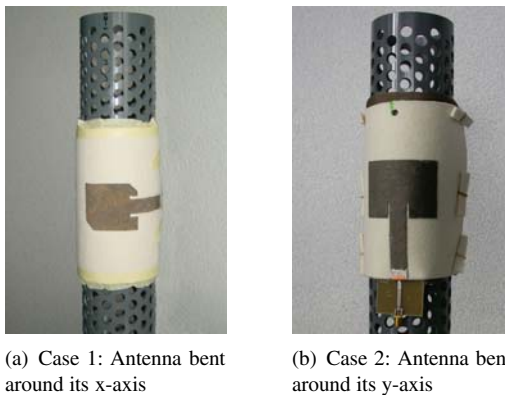


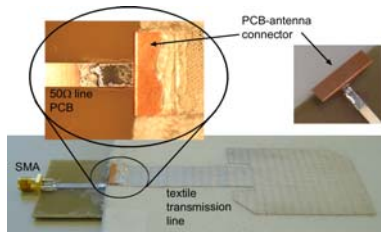
**Figure 5.12:** Bending gauge with  $75\text{mm}$  diameter

### 5.7.2. Antenna interconnect for measurements

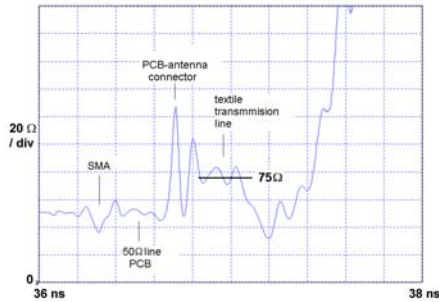
In order to interconnect the antennas with the measurement equipment, a PCB adapter with two connectors has to be deployed consisting of a SMA on one side and a special PCB-antenna connector on the other side. This transition actually serves the mechanical purpose of connecting from the PCB substrate to the much thicker fabric substrate as can be seen in the magnified section of Figure 5.13(a). Secondly, it electrically contacts the  $50\Omega$ -microstrip line of the PCB to the  $50\Omega$ - and  $75\Omega$ -microstrip feed line on the felt and spacer fabric, respectively. The two connectors on the PCB board can be regarded as discontinuities. In the impedance profile in Figure 5.13(b) obtained by time



domain reflectometry (TDR) [92], we can easily identify all parts of the interconnect, from the SMA connector over the  $50\Omega$ -line on the PCB, through the PCB-antenna connector to the antenna microstrip feed line (here:  $75\Omega$ ). Especially the connection from PCB to the textile substrate introduces a significant discontinuity.



(a) Antenna with PCB measurement adapter and magnified PCB-to-antenna connector



(b) TDR measurement curve of antenna with PCB measurement adapter

**Figure 5.13:** *Measurement of the antenna interconnect*

Thus, measured and simulated  $S_{11}$  parameters of the antennas cannot simply be re-normalized to achieve agreement. To remove this discontinuity, we model the PCB measurement adapters for the felt and spacer fabric antenna and deembed them from the  $S_{11}$  antenna measurements.

### 5.7.3. Return loss

The return loss or  $S_{11}$  describes the impedance mismatch between feed line and the antenna feed point. In our case, the feed line is the microstrip line and

the antenna feed point is located where the insets ends into the antenna patch (see Figure 5.3). We use a vector network analyzer (VNA) [7] to measure  $S_{11}$ .

Figure 5.14 shows the simulated and measured  $S_{11}$  characteristics of the four antennas when kept flat. All antennas except the CS antenna possess a good matching such that  $S_{11}$  is less than  $-10\text{dB}$  at their resonance frequency. Their  $-10\text{dB}$ -bandwidth features more than  $200\text{MHz}$ . The CS antenna can be optimized by further adjusting the antenna insets to  $75\Omega$  input impedance. The dielectric losses of the substrates introduce magnitude offsets of  $-3\text{dB}$  and  $-5\text{dB}$  for the spacer fabric and the felt, respectively. This behavior can be seen best at a frequency of  $2\text{GHz}$  in Figure 5.14.

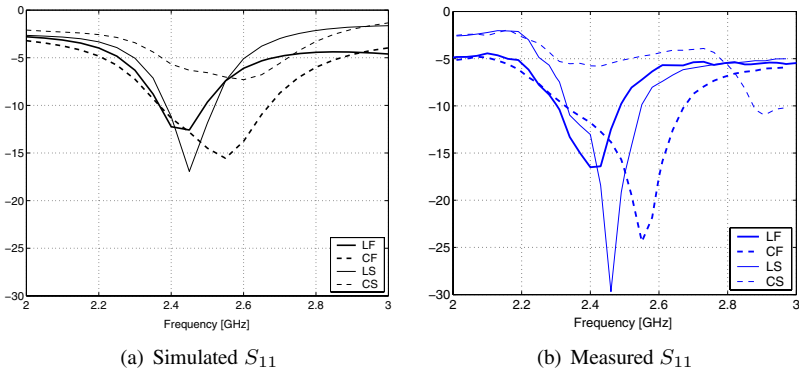


**Figure 5.14:** Simulated and measured  $S_{11}$  of the four planar antennas

### Return loss under bent conditions

We also conduct  $S_{11}$  measurements under defined bending conditions of the antennas. Figure 5.15 shows the change of the resonance frequency notch as a function of the bending radius. In this section, we focus on the LS and CF antennas for these and the later measurements under bent condition.

Generally, the resonances are shifted towards lower frequencies and the bandwidth becomes smaller when bent, independent of the bending direction. The smaller the bending radius is, the lower the resonance frequency becomes. Bending of a linearly polarized antenna according to case 1 (see Figure 5.12) elongates the antenna patch ( $L$  becomes bigger) and therefore, the resonance length. Formula 5.2 confirms such a behavior. Similarly, bending in case 2 widens the antenna patch whereby Formula 5.1 predicts a low-

ered resonance frequency.

Bending of circularly polarized antennas (CF and CS) affects both orthogonal radiation components at the same time. In case 1, the CF antenna performs like the LS antenna whereas the resonance frequency shows high immunity against bending in case 2.

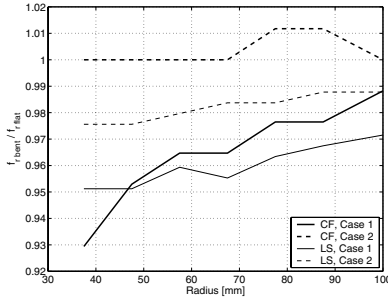


**Figure 5.15:** Measured resonance frequency  $f_{r,bent}$  as a function of bending radius normalized to the resonance frequency  $f_{r,flat}$  of the flat antenna. Bending axes correspond to the two cases given in Figure 5.12.

#### 5.7.4. Radiation patterns

A radiation pattern characterizes the variation of the radiated far-field intensity of an antenna as an angular function at a specific frequency. Usually, they are shown as cuts along the XZ and YZ planes according to the coordinate system given in Figure 5.3. The simulated and measured radiation patterns of two of the four antennas at  $2.4GHz$  are plotted in Figure 5.16 and 5.17 for the two orthogonal planes XZ and YZ. The measurements agree well with the simulation results. We observe only small differences, which are probably caused by manufacturing imperfections. The CP antennas show good left-handed circular polarization properties (only the Figures for the CF antenna are depicted). The results of the CP antennas should especially be appreciated since the current distribution in the two orthogonal directions is not obvious in the actual conductive textiles (see Figure 5.5). In the design process, we assumed isotropic parameters for the materials, which simplifies the actual inner structures of the materials. Our results prove that this assumption is reasonable.

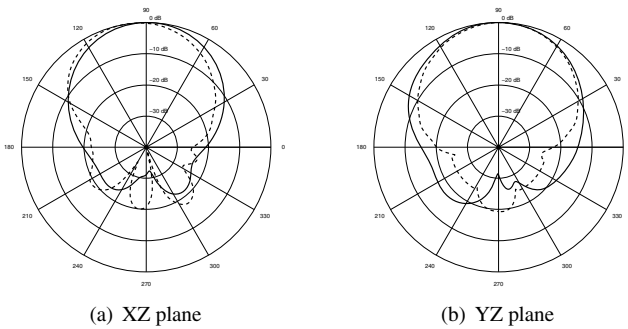


**Figure 5.16:** Simulated (solid) and measured (dashed) radiation pattern (co-polarization component) of LS antenna at 2.4GHz

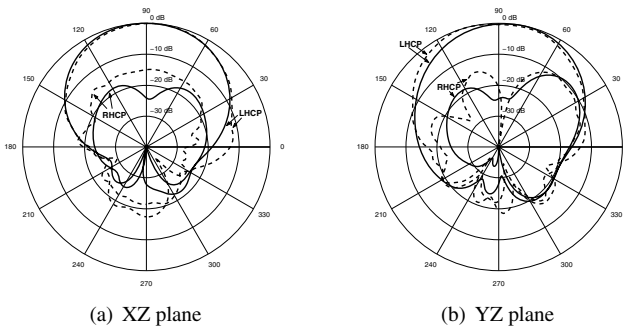


**Figure 5.17:** Simulated (solid) and measured (dashed) radiation pattern (co- and cross-polarization components) of CF antenna at 2.4GHz

### Radiation patterns under bend conditions

Since small bending radii show bigger effects on the antenna characteristic, we focused on radiation pattern measurements of bent antennas using the bending gauge with a radius of  $37.5\text{mm}$  as shown in Figure 5.12. Secondly, we only measured the LS antenna and the CF antenna in the two bending directions. The obtained patterns are presented in Figure 5.18 and 5.19, respectively. We can see that the bent antenna patterns are less directional for both antennas as compared to their patterns in flat shape. Secondly, bending according to case 1 shows bigger influence on the radiation patterns than

bending in case 2. Table 5.4 compares the half-power beamwidths of the antennas in flat and bent shape. The half-power beamwidth is the angle between the two points (on the same plane) at which the radiation falls to half ( $-3dB$ ) of the maximum power (normalized to  $0dB$ ). Evident is the increased level of back-radiation resulting from decreased shielding due to ground plane bending. In case of the CF antenna, we observe a degradation of CP performance, i.e. higher level of the cross-polarized RHCP component.

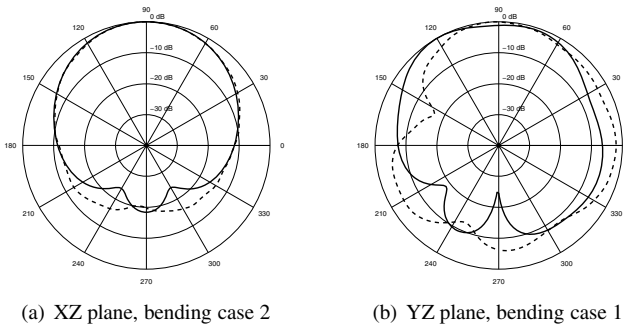


**Figure 5.18:** Simulated (solid) and measured (dashed) radiation pattern (only co-polarization component) of bent LS antenna (Radius 37.5mm) at 2.4GHz

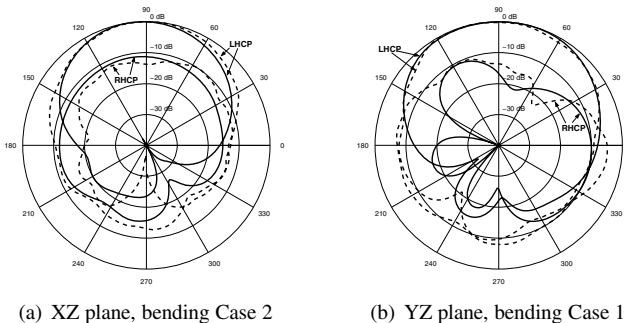


**Figure 5.19:** Simulated (solid) and measured (dashed) radiation pattern (co- and cross-polarization components) of bent CF antenna (Radius 37.5mm) at 2.4GHz

**Table 5.4:** Measured half-power beamwidth of LS and CF antenna

Configuration	LS	CF
XZ plane, Flat	57°	73°
YZ plane, Flat	62°	75°
XZ plane, Case 1	78°	82°
YZ plane, Case 2	87°	100°

### 5.7.5. Axial ratio (AR)

The axial ratio is a parameter to describe either elliptical or circular polarization [13]. It is defined as the ratio of the major to the minor axis of the polarizations ellipse of an antenna. To achieve circular polarization, the field vector (electric or magnetic) must fulfill the following conditions: a) the field must have two orthogonal linear components, b) the two components must have the same magnitude, c) the two components must have a time-phase difference of odd multiples of  $90^\circ$ . In the ideal case, AR would be equal to 1 (or  $0dB$ ). In practice, it is difficult to achieve  $AR = 1$ , especially for a wide frequency band and for a broad range of spatial directions of antenna propagation. Thus, an antenna is usually regarded to be circularly polarized (CP) when its axial ratio stays below  $3dB$  for a given direction of propagation.

We have extracted the AR from our simulated and measured radiation patterns of LHCP (left-hand rotating circular polarization) and RHCP (right-hand rotating circular polarization) field components for the circularly polarized antennas (CF and CS). The AR has been computed using Formula (5.4).

$$AR = \frac{LHCP + RHCP}{LHCP - RHCP} \quad (5.4)$$

It is evident that AR reaches infinity when LHCP and RHCP are equal meaning that the antenna is linearly polarized. In Figure 5.20, we can see the comparison between simulated and measured AR in the direction of maximum radiation for the CF and CS antennas.

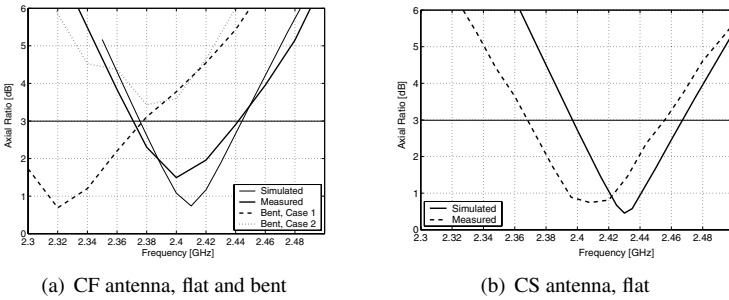
### Axial ration under bent conditions

Additionally, we have been interested in the effect of bending on the axial ratio. Again, we have concentrated on the radius of  $37.5mm$  and the CF antenna. Figure 5.20(a) also includes the bent measurements of the CF antenna. Bending pushes the axial ratio curve towards lower frequencies by about  $80MHz$  and abolishes circular polarization at all, respectively. In ad-

**Table 5.5:** Measured bandwidth of axial ratio for CF and CS antenna

Antenna	Measured BW [MHz]	[%]	Bending radius [mm]
CS	88	3.65	$\infty$
CF	71	2.96	$\infty$
CF	100	4.3	37.5mm, Case 1
CF	no CP		37.5mm, Case 2

dition, bending in case 1 broadens the bandwidth of the axial ratio as can be verified in Table 5.5.

**Figure 5.20:** Simulated and measured axial ratios [dB] of CF and CS antenna

## 5.8. Conclusion

We have shown that standard design techniques for patch antennas perform well even for textile substrates and conductive textiles. The antennas presented not only feature good properties, but they are also easy to manufacture. They show bandwidths of about  $200\text{MHz}$  and possess directivity with a half-power beamwidth of less than  $75^\circ$ .

The antennas satisfy Bluetooth specifications even when bent down to radius of  $37.5\text{mm}$  and mounted according to case 2 (Figure 5.12(b)). Generally,  $S_{11}$  and radiation pattern show better robustness against bending in case 2 whereas the axial ratio is more sensitive in this configuration. Bending causes a similar impact on the characteristic of linearly and circularly polar-

ized antenna, though, circularly polarized antennas lose their CP property at the specified center frequency ( $2.4GHz$ ).

The choice of a knitted or a woven conductive textile for antennas depends on the application and its favored deformation behavior. In our investigations, we could see that mechanical stabilization is essential to preserve the desired antenna characteristic. This requirement can either be satisfied by using a stable (non-knitted) substrate such as the felt or by using a stable (non-knitted) patch/ground plane.



# 6

## Fabric Embedded Temperature Sensor\*

*In this chapter, a smart fabric with temperature sensing capability is presented. The goal is to achieve a measurement accuracy of 0.5 Kelvin over a temperature range of 10°C to 60°C that is comparable to commercial products such as thermistors (e.g. Pt100) and thermocouples. The woven structure of the fabric itself represents an array of temperature sensors that can be utilized to measure the temperature profile of a surface.*

---

\*based on [61]

## 6.1. Introduction

We use the same PETEX fabric as introduced in Chapter 3 for our fabric embedded temperature sensor. A picture of PETEX is shown in Figure 3.2. In this chapter, two variants of fabric embedded temperature sensors are presented in order to measure temperature profiles of surfaces. The array grid sensor utilizes single wires as sensors whereas the meander-shaped sensor uses several wires to form the sensor element.

Using fabrics for temperature measurement is only one option, however, fabrics have the capacity to integrate other sensing functionality. Lorussi *et al.* [63] work on fabric-based strain sensors in order to track body postures. Companies such as Softswitch [86], Eleksen [12] and ITP [39] investigate in fabric pressure sensors.

## 6.2. Measurement concept

In this section, the measurement concept along with measurement accuracy considerations are briefly described. In the proposed method, the temperature dependence of the electrical resistance of metals is utilized for temperature measurement according to (6.1).

$$R_{wire} = R_0(1 + \alpha_{metal} \cdot \Delta T) \quad [\Omega] \quad (6.1)$$

$R_0$  specifies the wire resistance at temperature  $T_0$  and  $\alpha_{metal}$  is the temperature coefficient.  $\alpha_{metal}$  is similar for all metals and features about  $0.4\%/K$  for copper. The wire length elongation as well as the quadratic coefficient of resistance change due to temperature variations are negligibly small for our intended measurement range from  $0^\circ C$  to  $60^\circ C$ . We utilize the same fabric as presented in Chapter 3 with thin copper wires of about  $17\Omega/m$  at  $20^\circ C$ . Due to the low mass of a wire ( $123d tex = 12.3\mu g/m$ ) and the high thermal conductivity of copper, such a sensor reacts quickly towards temperature changes.

### 6.2.1. Electronic measurement circuit

Since the resistance of the thin copper wire as well as its temperature coefficient  $\alpha_{Cu}$  are small, the 4-wire resistance measurement principle is recommended to achieve the target accuracy of  $0.5K$ . Secondly, a difference measurement method for the ohmic resistance is proposed in order to eliminate circuit offsets and component tolerances. A possible circuit of such a

measurement method is presented in Appendix D.

### 6.2.2. Theoretical temperature measurement accuracy

The temperature measurement accuracy is influenced by different factors and effects.

1. *Wire length*: accuracy improves the longer a measurement wire in the fabric is. A longer wire directly corresponds to a higher resistance. Thus, a larger resistance change per Kelvin occurs as compared to a short wire. This behavior can be seen from Formula (6.1).
2.  $\alpha_{metal}$ : this material constant in Formula (6.1) is not precisely known for the copper alloy of the wire.
3. *Offset Voltage*  $V_{ofs}$ : Electronic components such as operational amplifiers possess offset voltages.
4. *Component tolerances*: All electronic components in a circuit have tolerances (e.g. resistances, capacities, reference diodes, analog-to-digital converters).
5. *Thermal noise*  $V_{noise}$ : Generally, measurements of the wire resistance are corrupted with thermal noise.
6. *Temperature drift*  $V_{drift}$ : Electronic components show temperature drift.

Item 1 – 4 of the list above have a constant effect on the temperature measurement accuracy. They are eliminated by a difference measurement as proposed in Appendix D and by a measurement calibration as described in Subsection 6.5.1.

Thus, the dynamic elements in item 5 + 6 of the measurement system remain that can be modelled the following way (6.2)

$$V_{AD} = V_{Rwire}(T_{wire}) + V_{noise} + V_{drift} \quad [V] \quad (6.2)$$

$V_{Rwire}$  is an affine function of the wire temperature. It describes the voltage drop that corresponds to the actual temperature of the wire. However, the measurement is perturbed by  $V_{noise}$  and  $V_{drift}$ . The thermal noise  $V_{noise}$  can statically be reduced by multiple measurements  $N$  with an accuracy improvement following the  $1/\sqrt{N}$ -law. The temperature drift of the circuit  $V_{drift}$  can be lowered by choosing components with low temperature drift or by a temperature compensated measurement circuit.

### 6.3. Fabric temperature sensors

We present two geometrical variants of textile embedded temperature sensors: an array grid sensor and a meander-shaped sensor. The meander-shaped sensor is utilized in the proof-of-concept circuit presented in Chapter 2.

#### 6.3.1. Array grid sensor

The grid of copper wires in PETEX allows the measurement of temperature along a surface. In our experiments, we utilized a  $10 \times 10 \text{ cm}^2$  fabric patch as temperature sensor array. A principle schematic is given in Figure 6.1. The measurement electronic connects to opposing ends of sensor wires. Due to the wire topology, location information of 'hot spots' can be extracted by measuring wire resistance in x- and y-direction.

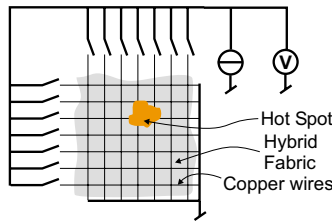


**Figure 6.1:** *Temperature measurement array*

#### Measurement ambiguity

Instantly, such a sensor topology seems to be attractive to measure temperature distribution across a surface. However, the system is under-determined from a mathematical point of view since we only have  $2N$  measurements in a  $N \times N$  grid with  $N^2$  cross-points for temperature measurement. This fact leads to spatial ambiguity. Unless all the 'hot spots' are aligned in a row or a column, additional virtual 'hot spots' are measured.

For instance, the measurement of two actual 'hot spots' on the fabric result in detection of two additional virtual 'hot spots' as can be seen in Figure 6.2. Three actual 'hot spots' result in an additional 6 virtual 'hot spots', etc.

#### 6.3.2. Meander-shaped sensor

Figure 6.3 shows the meander-shaped sensor embedded in the fabric. The overall wire length is  $38 \text{ cm}$  that corresponds to about  $6.5 \Omega$ . The total sensor

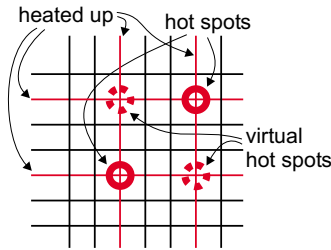


**Figure 6.2:** Measurement ambiguity due to the wire grid structure

area is  $2x2cm^2$ .

Such sensors can be arranged in arrays to measure the temperature profile of a surface. Attention must be paid that the four feed lines of each sensor can escape from the array and be connected to the measurement electronics.

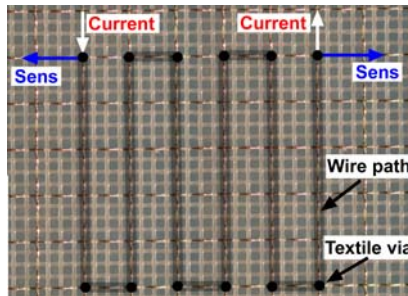


**Figure 6.3:** Principle of the meander-shaped fabric embedded temperature sensor

### 6.3.3. Comparison of the sensor variants

The two sensor variants possess several advantages and disadvantages listed in Table 6.1.

The notation *unsharpness* in the table is explained in the following. In the array grid sensor, the measured temperature is averaged of the wire length. For instance, the measured temperature of a single wire is the same whether the entire wire is heated up by  $1K$  or only half of the wire is heated up by  $2K$ . Secondly, we do not know the location where the wire has been heated. The measurement returns the averaged temperature of the wire whereby 'hot

**Table 6.1:** Advantages (+) and disadvantages (-) of the two sensor variants

	Array grid	Meander-shaped
+	<ul style="list-style-type: none"> <li>• Simple sensor structure (just a straight wire)</li> <li>• Structure to measure surface temperature distribution simple. It consists of cross-running wires.</li> </ul>	<ul style="list-style-type: none"> <li>• No spatial ambiguity because of sensor area of <math>2 \times 2 \text{ cm}^2</math></li> <li>• More accurate measurements due to a large overall wire length</li> <li>• No unsharpness between temperature and location of a 'hot spot'. Sensor is the 'hot spot'.</li> </ul>
-	<ul style="list-style-type: none"> <li>• Spatial ambiguity in temperature profile</li> <li>• Unsharpness between temperature and location of a 'hot spot'</li> <li>• Feed lines are on opposing sides of the wire</li> </ul>	<ul style="list-style-type: none"> <li>• Sensor structure needs textile vias</li> <li>• Difficult to feed sensors in an array structure</li> </ul>

spots' gets smeared out over the entire wire length.

Therefore, short wire improves the location information of the 'hot spot'. On the other hand, a short wire features a lower resistance, which results in a more imprecise temperature measurement using the same measurement electronic.

This behavior between temperature measurement accuracy and location information of temperature resembles an uncertainty principle.

## 6.4. Temperature profile estimation

A restriction of the array grid sensor to single 'hot spot' detection relaxes the problem of ambiguity. The temperature distribution estimation of such a single 'hot spot' is shown in Figure 6.4, where a finger touched the fabric in the rear corner. The estimated distribution of the temperatures is computed by taking the outer product of the temperatures along the row and column wires according to (6.3). This method corresponds to the geometrical mean temperatures of crossing wires.

$$T_{est} = \sqrt{T_{row} \cdot T_{col}^T} \quad [^{\circ}C] \quad (6.3)$$

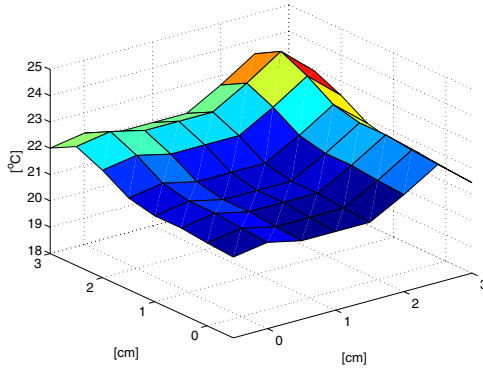


**Figure 6.4:** Temperature distribution along fabric surface

## 6.5. Temperature measurement accuracy

In this section, verification of the temperature sensors is described. We place the textile temperature sensor along with a reference thermometer in a climate chamber and measure the temperature at six stationary temperature levels. From these measurements, we then determine the actual  $\alpha_{metal}$  to calibrate the system.

Figure 6.5 shows the temperature linearity neglecting the tolerances of the reference thermometer. Note that our reference thermometer (Fluke DMM with thermocouple) itself has an accuracy of only  $\pm 1\% (+3^\circ C)$  [100].

Since we do not know  $\alpha_{metal}$  exactly, the slope of the measured curve with an assumed  $\alpha = 0.00404 K^{-1}$  (solid line in the figure) is too flat.

### 6.5.1. Calibration and determination of $\alpha_{metal}$

Since we do not know the true  $\alpha_{metal}$ , we approximate its value with linear regression using Formula (6.4).  $T_0$  corresponds to the reference temperature level and  $T_{act}$  is the temperature measured by the reference thermometer.  $T_{meas}$  corresponds to the temperatures measured by the textile sensor. Each element in the  $T_{meas}$  vector has been averaged over 500 measurement samples in advance.

$$\alpha_{true} = \alpha_{Cu} \frac{(T_{meas} - T_0)^T (T_{meas} - T_0)}{(T_{act} - T_0)^T (T_{meas} - T_0)} \quad [K^{-1}] \quad (6.4)$$

With this approach, we obtain an  $\alpha_{true} = 0.0035 K^{-1}$  for calibration of

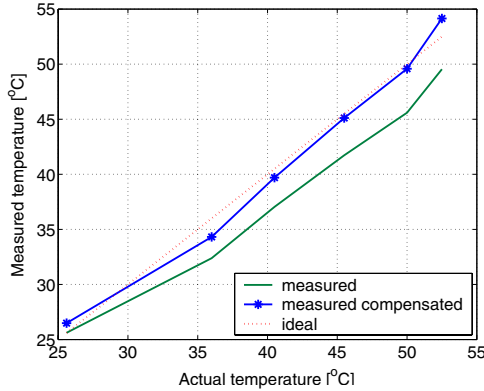


**Figure 6.5:** Temperature measurement linearity

the sensor. The corresponding  $\alpha$ -compensated curve is depicted as solid line with stars in Figure 6.5. The measurement points of the fitted curve feature a standard deviation of  $\sigma_e = 1.2K$  to a ideal curve (straight dotted line).

This approximation of  $\alpha_{true}$  (6.4) has been computed using the least mean square error approach shown in formula (6.5).

$$\frac{\partial}{\partial \alpha_{true}} \sum_i [T_{act_i} - T_0 - (T_{meas_i} - T_0) \frac{\alpha_{Cu}}{\alpha_{true}}]^2 = 0 \quad (6.5)$$

### 6.5.2. Measured temperature distribution

The same temperature at  $50^\circ C$  is repeatedly measured (e.g. 500 times) with the fabric temperature sensor in order to determine the measurement accuracy and repeatability. The measurements reveal a standard deviation of  $\sigma = 0.39K$  whereby the standard deviation behaves similarly for other temperatures. Figure 6.6 depicts the temperature distribution for  $50^\circ C$ .

## 6.6. Conclusion

This chapter has presented a fabric temperature sensor with an accuracy of about  $1.2K$  when using linear regression. We have shown that PETEX is suitable for measurement of temperature and temperature profiles. A calibration of the sensors is necessary to obtain the true  $\alpha_{metal}$  and to obtain  $R_0$  at  $T_0$ .



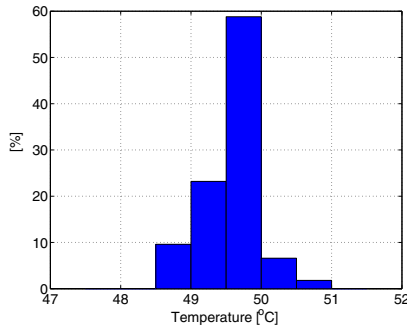


**Figure 6.6:** *Measurement distribution of the fabric temperature sensor over 500 iterations at 50°C*

The measurement accuracy can be improved to the targeted  $0.5K$  with several approaches

- Wires consisting of material with a higher resistivity, e.g. stainless steel ( $7.2 \cdot 10^{-7} \Omega m$ ) and nickel-chrome ( $1.5 \cdot 10^{-6} \Omega m$ ) and higher temperature coefficient than copper results in a larger resistance change per Kelvin.
- The entire temperature curve depicted in Figure 6.5 can be recorded as calibration set in advance. A measured temperature is then corrected according to this calibration set.
- A measurement circuit with temperature compensation and less noisy components reduces error sources in the measurements.



# 7

## Conclusions

### 7.1. Achievements

During the PhD studies, we have developed a light-weighted woven fabric<sup>1</sup> called PETEX whose embedded copper wires easily withstands the tensile stresses of daily life. Using these embedded thin copper wires, we tested several transmission line configuration regarding their electrical performance. Their bandwidths lie in the range of  $2GHz$  featuring line impedances between  $180\Omega$  and  $310\Omega$ . A new approach for unwrapping the signal phase has been proposed and applied to obtain a smooth permittivity curve. Floating parallel wires within the fabric do not affect the electrical performance of the transmission lines at frequencies below  $2GHz$ . Cross-running wires increase permittivity and introduce noise in the frequency response. Transmission lines that are printed on a fabric more resemble conventional CPWs on a PCB. Their electrical properties outperform the wire-based transmission lines.

Interconnects among the copper wires within the fabric are manufactured using the steps *wire coating removal*, *wire cutting*, *connecting the skinned wire sections* and *protecting the interconnect*. We have conducted extensive

---

<sup>1</sup>in collaboration with Sefar Inc.

studies to optimize the laser parameters in the skinning step. We have proposed five via configurations and we showed that via configurations for wire pairs feature a bandwidth of about  $600MHz$ , which is about  $1/3$  of the bandwidth of a transmission line.

Our novel interposer technology eases the design and assembly of electronic components onto the fabric. The elimination of cuts in the fabric not only simplifies fabrication, but also preserves mechanical stability of the fabric. Such an interposer connect features about the same inductivity as a bond wire in a chip package. We have further addressed the optimization of an application-independent interposer design and we determine the space occupancy of different interposer variants.

We have presented a flow chart on the design and routing of an SoT. Furthermore, we have identified additional constraints and hints for an SoT design regarding component placement, RF signal and analog signals. The utilization of the algorithm for automatic placement of necessary cuts within the fabric is recommended.

Our Bluetooth antennas for the WPAN possess flat structure and are designed in linear and circular polarization variants. Different manufacturing methods have been investigated. The antennas possess directive radiation patterns such that they radiate away from the human body in a WPAN. Simulations and measurements of the antennas generally agree, even under bent conditions.

Finally, a simple circuit for a fabric embedded temperature sensor has been presented. The sensor achieves an accuracy of about 1 Kelvin using two-point calibration for a temperature range from  $0^{\circ} - 60^{\circ}C$ .

## 7.2. Outlook

There are several opportunities for future research. From a theoretical point of view, routing strategies within the fabric can further be enhanced and optimized. Considering the existing geometrical tolerances in the fabric, a robust routing approach that is immune against inaccuracies is crucial. For that reason, the approach of using multiple wires in parallel for the global wiring might be extended.

The current epoxy resin encapsulation possesses a high leakage current, especially at elevated humidity. Different epoxy filler lowers this leakage current. Further, the epoxy must currently be applied to both sides of the fabric.

A lowering of its viscosity could simplify this procedure such that epoxy must only be applied to one side. On the other hand, viscosity must not be too low in order to avoid spreading on the fabric.

Up to now, only handcrafted prototypes of SoT's exist. There is still some effort needed for introduction to mass production, though the way is straightforward and already paved by the established flexible PCBs.

Alternatives to the presented *textile via* manufacturing process are feasible. The wire skinning and the wire interconnection could be done by thermo-compression bonding. This technology features the advantage that the two steps could be merged. Thermo-compression bonding includes heating and welding that removes the coating of the wires and joins them afterwards.

Regarding mechanical tests of the plain fabric and of the fabric with assembled components, cyclic load stress as well as washing cycles are planned.

From the electrical point of view, the interposer and interposer pads are weakly specified. However, specifications of crosstalk, reflections, impedances and capacities are highly dependent on the layout of a circuit. Once a critical application design is identified (e.g. signals with frequencies higher than  $600MHz$ ), these parameters can be determined by TDR and VNA measurements as well.

Printed textile transmission lines are still an interesting niche for dedicated applications requiring specific line impedances. Their structure leaves more freedom regarding line impedance and line shapes compared to the wire-based transmission lines.

The Bluetooth patch antennas have not been investigated considering effects of human body proximity. This influence need to be explored in the future.



# A

# Transmission Lines

## A.1. Introduction

Transmission line theory is a well-known approach to model wiring structures such as microstrip lines, coplanar waveguides and wire pairs. The theory is valid as long as a single mode propagates through the transmission line. In the following section, we will see that this assumption is not always true for textile transmission lines.

A transmission line can be modeled with elements known from electrical engineering, i.e. resistance, conductance inductance and capacitance, as shown in Figure A.1. They are normalized to one meter. The so-called *Telegrapher's Equations* (A.1) are directly derived from the figure. The *propagation constant*  $\gamma$  and the *characteristic impedance*  $Z_0$  are then obtained by using  $R'$ ,  $G'$ ,  $L'$  and  $C'$ . Their formulas for a non-dispersive transmission line are given in (A.2).  $\alpha$  corresponds to the damping in Neper<sup>1</sup> and  $\beta$  corresponds to the phase.

---

<sup>1</sup>1Np = 8.69dB

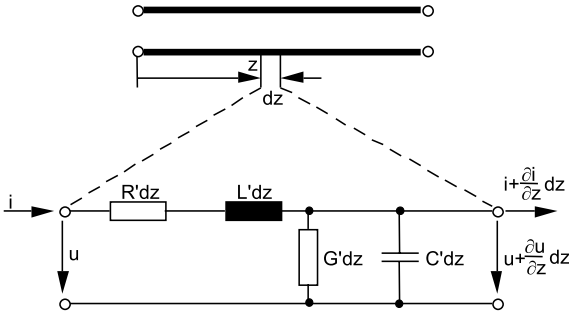


**Figure A.1:** Transmission line model

$$\frac{\partial}{\partial z} V(z, t) = -L' \cdot \frac{\partial}{\partial t} I(z, t) - R' \cdot I(z, t) \quad (\text{A.1})$$

$$\frac{\partial}{\partial z} I(z, t) = -C' \cdot \frac{\partial}{\partial t} V(z, t) - G' \cdot V(z, t)$$

$$\gamma = \sqrt{(R' + j\omega L')(G' + j\omega C')} = \alpha + j\beta \quad (\text{A.2})$$

$$Z_0 = \sqrt{\frac{R' + j\omega L'}{G' + j\omega C'}} \quad [\Omega]$$

Corollary, the values for  $R'$ ,  $G'$ ,  $L'$  and  $C'$  can easily be derived from Equations (A.2) using Formulas (A.3).

$$\begin{aligned} R' &= \text{Re}\{\gamma Z_0\} && [\Omega/m] \\ L' &= \text{Im}\{\gamma Z_0\}/\omega && [H/m] \\ G' &= \text{Re}\{\gamma/Z_0\} && [1/\Omega m] \\ C' &= \text{Im}\{\gamma/Z_0\}/\omega && [F/m] \end{aligned} \quad (\text{A.3})$$

## A.2. Transmission line parameter extraction

In order to determine these parameters for transmission lines including effective relative permittivity  $\epsilon_r$ , the approaches described in [41, 53, 67, 77, 85, 102] are applied. They all use similar techniques that deliver similar results.

For a better understanding, a simplified explanation of [53] is given here. The scattering parameters of two transmission lines of different lengths,  $l_1$  and  $l_2$ , are measured and translated into the scattering chain matrices repre-



sentation  $T_1$  and  $T_2$ <sup>2</sup>. In [53], they model the lines using the form  $T_1 = T_A T_B$  and  $T_2 = T_A T_L T_B$  where  $T_A$  and  $T_B$  are the chain matrices of the connection adapters (error boxes) on both sides of the transmission lines. An error box  $T_A$  represents the short transmission line (THRU) cut in half.  $T_L$  depicts the chain matrix of the transmission line with length  $\Delta l = |l_1 - l_2|$ . This model is shown in Figure A.2.  $T_L$  is assumed reflectionless and must be isolated in order to determine the transmission line parameters. By assuming equal error box matrices  $T_A, T_B$  for both transmission lines,  $T_L$  is extracted using approach (A.4).

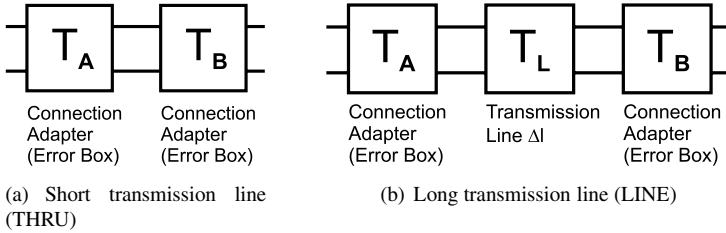


**Figure A.2:** Model of transmission lines in chain matrix representation

$$T = T_2 T_1^{-1} = T_A T_L T_A^{-1} \quad (\text{A.4})$$

Since  $\text{tr}(T) = \text{tr}(T_L)$  and  $T_L = \begin{pmatrix} e^{-\gamma \Delta l} & 0 \\ 0 & e^{\gamma \Delta l} \end{pmatrix}$ ,  $\gamma$  can be determined with Formula (A.5).

$$\gamma = \pm \frac{1}{\Delta l} \text{acosh} \left[ \frac{\text{tr}(T)}{2} \right] = \alpha + j\beta \quad (\text{A.5})$$

Note that  $e^{-\gamma \Delta l}$  is periodic in  $2\pi$ . Thus, a unique mapping between  $e^{j\beta l}$  and the phase  $\varphi = \beta l$  is not possible. As a result, the phase  $\varphi$  must first be unwrapped in order to arrive at the correct  $\beta$ . The effective relative permittivity  $\epsilon_{r_{eff}}$  is then computed from the unwrapped phase  $\varphi$  using Formula A.6 where  $c_0$  is the speed of light and  $f$  is the frequency.

$$\epsilon_{r_{eff}} = \left( \frac{c_0 \cdot \varphi}{2\pi f \cdot \Delta l} \right)^2 \quad (\text{A.6})$$

<sup>2</sup>This translation is described in Appendix B

The characteristic impedance  $Z_0$  is computed using  $\gamma$  and the scattering parameters of the error box  $T_A$  according to Grzyb *et al.* [41]. Alternatively,  $Z_0$  can directly be determined by using time domain reflectometry (TDR) measurements [92] as well.

### A.3. Textile transmission line characterization

A line impedance of  $50\Omega$  is usually desired in electronics. However, the structure of textile transmission lines as well as the low permittivity of textiles ( $\epsilon_r = 1..3$ ) do not allow achieving  $50\Omega$  (see Section 3.3). Measurements in Section 3.3 and [25, 60] have shown that wire pair line impedances lie in the range of  $250\Omega$ .

#### A.3.1. Measurement perturbations

Due to the high impedance step from the  $50\Omega$  measurement equipment to the approximately  $250\Omega$  textile transmission line, reflections and resonances occur resulting in higher odd modes. Tolerances in the fabric as well as length differences between signal and ground lines further support generation of these modes. Such effects have also been described by Cottet *et al.* [25]. In other words, several modes can propagate through the transmission line that are not easily describable with transmission line theory. Details to higher odd modes and their leakage are explained by Oliner *et al.*, Wen-Teng Lo *et al.*, Tien *et al.* and Shigesawa *et al.* in [58, 72, 83, 94].

The connection adapter defines another error source. An precise transition from connection adapter to fabric is not achievable because of geometrical and material incompatibilities, e.g. textile and PCB pitches. Thus, the necessary assumption of equal error boxes introduces additional errors in the parameter extraction.

Those higher odd modes cause additional damping (i.e.  $\alpha$ ) and perturbations of the phase (i.e.  $\beta$ ). Especially the phase is critical for the extraction of  $\epsilon_r$ . In section A.3.2, a new approach for a smooth unwrapping of a perturbed phase is proposed.

#### A.3.2. Unwrapping of a perturbed phase

Unwrapping the phase means to remove its  $2\pi$  periodicity. In a well-behaved phase response, unwrapping is easily done by adding a multiple of  $2\pi$  to the phase whenever a phase jump occurs. In a perturbed phase response, this procedure leads to parasitic phase jumps and therefore to errors in the unwrapped

phase response.

A new approach is to estimate the phase response in a first step and then, to unwrap the phase such that the error between estimated and actual phase is minimal. An ideal phase response of an ideal transmission line is proportional to the frequency,  $\varphi_i = m \cdot f_i$  (linear). In order to estimate the slope  $m$ , a least mean square error approach according to Formula (A.7) is proposed (linear regression). By differentiation, we arrive at Formula (A.8).

$$\min \sum_i (\varphi_i - \hat{\varphi}_i)^2 \quad (\text{A.7})$$

$$m = \frac{\sum_i \varphi_i f_i}{\sum_i f_i^2} \quad \left[ \frac{\text{rad}}{\text{Hz}} \right] \quad (\text{A.8})$$

Since a textile transmission line is far from being ideal, adaptive phase estimation is desired. Thus, we do not include all measurements for a global estimate of  $m$ , but only a few samples for a local estimate and then iteratively estimate the slope  $m_k$ . This algorithm is described in Formula (A.9) where  $N$  corresponds to the number of samples included for a current estimate  $k$ . A good start estimate of  $m_k$  is critical for an accurate unwrapping. In addition, a leaky bucket filter given in Formula (A.10) is applied to  $m_k$  in order to suppress outliers whereby  $t$  is an empirical number close to 1.

$$m_k = \frac{\sum_{i=k-N}^k \varphi_i f_i}{\sum_{i=k-N}^k f_i^2} \quad (\text{A.9})$$

$$m_{i+1} = t \cdot m_i + (1 - t) \cdot m_k \quad (\text{A.10})$$

Eventually, we arrive at the iterative algorithm given in (A.11) to unwrap the phase response  $\varphi_i$ . Note that the estimated slope  $m$  corresponds to a smoothed version of the unwrapped phase response  $\varphi$ .

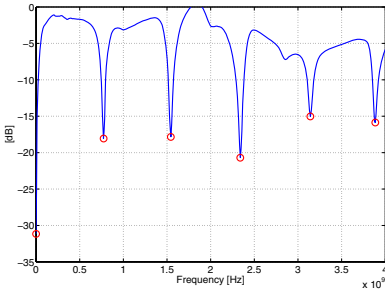
$$\left. \begin{aligned} \varphi_i &= \varphi_i + 2\pi n & \text{init } n=0 \\ n &= n + \underset{p \in \{0,1\}}{\text{argmin}} [\varphi_{i+1} + 2\pi(n+p) - m_{i+1} f_{i+1}]^2 \end{aligned} \right] \quad (\text{A.11})$$

A quick alternative to this iterative approach is a phase response estimate by analyzing the scattering parameter  $|s_{11}|$ . However, this alternative delivers only few supporting points and it works only reasonable with big impedance steps between measurement equipment and transmission line. In other words, big reflections must occur. Whenever a multiple of half-wavelengths of the measurement signal corresponds to the physical transmission line length  $L$ ,

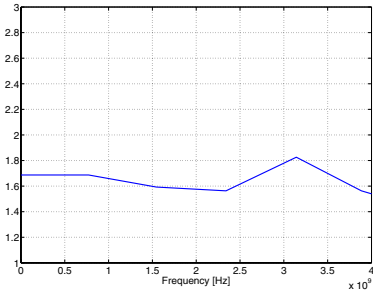
no reflections occur and  $s_{11}$  shows a sharp notch at this frequency  $f_i$ . An example of such a measurement curve is depicted in Figure A.3(a). Tracking these notches and using them together with Formula (A.12) and (A.13) delivers an estimate for  $\varphi$  and  $\epsilon_r$ . Figure A.3(b) shows the extracted  $\epsilon_r$  of measurement A.3(a).

$$\varphi_i(f_i) = \pi \cdot i \quad \text{with } i=0..(\# \text{ of notches})-1 \quad (\text{A.12})$$

$$\epsilon_{ri}(f_i) = \left[ \frac{c_0}{(f_{i+1} - f_i) \cdot 2L} \right]^2 \quad L : \text{line length} \quad (\text{A.13})$$



(a)  $S_{11}$  with notches in half-wavelength spacing indicated by 'o'



(b) Extracted  $\epsilon_r$  using the notch spacing and Formula (A.13)

**Figure A.3:** *Alternative approach to extract  $\epsilon_r$  from a single transmission line*

The advantage of this method is that only one transmission line must be measured in order to determine the effective relative permittivity  $\epsilon_r$ .

# B

## Matrix definitions and conversions

**Scattering parameters (s-parameters)**

$$\begin{bmatrix} b_1 \\ b_2 \end{bmatrix} = \underbrace{\begin{bmatrix} s_{11} & s_{12} \\ s_{21} & s_{22} \end{bmatrix}}_S \begin{bmatrix} a_1 \\ a_2 \end{bmatrix} \quad (\text{B.1})$$

**Transfer matrix (Scattering chain matrix, Wave chain matrix)**

$$\begin{bmatrix} b_1 \\ a_1 \end{bmatrix} = \underbrace{\begin{bmatrix} t_{11} & t_{12} \\ t_{21} & t_{22} \end{bmatrix}}_T \begin{bmatrix} a_1 \\ b_2 \end{bmatrix} \quad (\text{B.2})$$

**Chain matrix (ABCD matrix)**

$$\begin{bmatrix} V_1 \\ I_2 \end{bmatrix} = \underbrace{\begin{bmatrix} A & B \\ C & D \end{bmatrix}}_{ABCD} \begin{bmatrix} V_2 \\ I_2 \end{bmatrix} \quad (\text{B.3})$$

$$V_x = a_x + b_x \quad I_x = a_x - b_x$$

### Matrix conversion

$$\begin{aligned} S &= \frac{1}{t_{22}} \begin{bmatrix} t_{12} & |T| \\ 1 & -t_{21} \end{bmatrix} \\ &= \frac{1}{\Delta} \begin{bmatrix} A + B/Z_0 - Z_0C - D & 2(AD - BC) \\ 2 & -A + B/Z_0 - Z_0C + D \end{bmatrix} \end{aligned}$$

$$\text{with } \Delta = A + B/Z_0 + Z_0C + D, \quad Z_0 = Re(Z_0) \quad (\text{B.4})$$

$$\begin{aligned} T &= \frac{1}{s_{21}} \begin{bmatrix} -|S| & s_{11} \\ -s_{22} & 1 \end{bmatrix} \\ &= \frac{1}{2} \begin{bmatrix} A + B/Z_0 - Z_0C - D & A - B/Z_0 - Z_0C + D \\ A + B/Z_0 + Z_0C + D & A - B/Z_0 + Z_0C - D \end{bmatrix} \end{aligned}$$

$$\text{with } Z_0 = Re(Z_0) \quad (\text{B.5})$$

$$\begin{aligned} ABCD &= \frac{1}{2s_{21}} \begin{bmatrix} 1 + s_{11} - s_{22} - |S| & Z_0(1 + s_{11} + s_{22} + |S|) \\ (1 - s_{11} - s_{22} + |S|)/Z_0 & 1 - s_{11} + s_{22} - |S| \end{bmatrix} \\ &= \frac{1}{2} \begin{bmatrix} t_{11} + t_{12} + t_{21} + t_{22} & Z_0(-t_{11} + t_{12} - t_{21} + t_{22}) \\ (-t_{11} - t_{12} + t_{21} + t_{22})/Z_0 & t_{11} - t_{12} - t_{21} + t_{22} \end{bmatrix} \end{aligned}$$

$$\text{with } Z_0 = Re(Z_0) \quad (\text{B.6})$$

# C

## Practical textile routing hints

### **C.1. Interposer design**

The routing structure on an interposer follows the common rules of a PCB layout. The following routing properties are recommended.

- via ring diameter: 0.4mm
- via hole size: 0.15mm

Vias of the interposer are directly utilized as interconnecting pads to the fabric. Thus, these via pads must be placed in the wire grid spacing of the fabric. Vias that are not used as pads should be tented to avoid shorts. The via pads must be plated with gold to preserve good electrical contact with the conductive adhesive.

## C.2. EDA tool configuration for textile layout

The layout within the fabric must follow the perpendicular grid of the fabric. A via must be placed at each change from a vertical to a horizontal wire and vice versa (diameter: 0.4mm). In order to avoid errors in the layout, different layers are recommended for the horizontal and the vertical wires. Some EDA tools possess the feature to automatically 'remove loops' in a layout. This feature should be switched off as soon as several wires are deployed in parallel, e.g. in power nets.

## C.3. Correction of layout coordinates

Although the PETEX fabric is very precise, the copper wires within the fabric are not accurately enough located to immediately apply the EDA output data for a layout. Currently, we see two options to overcome this imprecision. The fabric is equipped with colored threads in a regular spacing and the laser machine as well as the assembly machine orient themselves according to these wires. Thus, the machine compensates the inaccuracy of the fabric. However, this method still needs interactions of the operator.

The second approach does an off-line correction. The fabric is scanned using an office scanner with a minimal resolution of 2400 DPI beforehand. The copper wires can clearly be identified at such a resolution. A matlab script tracks then the wires piecewisely within the scanned image in warp and weft by utilizing a matched filter. The wire intersections are then computed with the logged coordinates of the wires. A section of such a processed fabric can be seen in Figure C.1. Eventually, the EDA output data is corrected by the actual coordinates of the computed wire intersections.

This methods however requires that every fabric is scanned and measured before manufacturing.

## C.4. Fabrication files

Figure C.2 explains the data flow for generation of the fabrication data for the routing in the fabric.

The 'bottom solder paste mask' file (Gerber format) contains the coordinates of all vias that are not tented. In other words, these are the textile vias as well as via pads of the interposers. The IPC-356-D file contains all vias with their net names. A matlab script reads these files and assigns the net names to the vias while filtering out the tented vias.



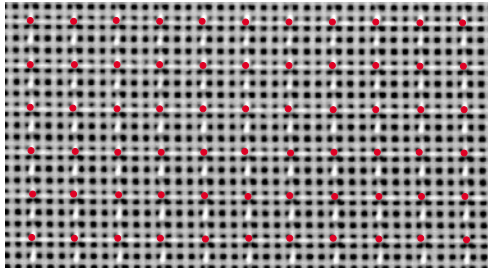


**Figure C.1:** *Fabric with tracked copper wire intersections*

The cuts are then placed (according to algorithm in Chapter 4) after assigning the net names.

Another matlab script tracks the intersections of the copper wires and writes their coordinates into a file (see Section C.3).

The coordinates of the vias with the added cuts are then corrected with the tracked wire intersection coordinates.

Finally, the via coordinates are written to a gerber file for laser ablation and the cuts are written to a gerber file for cutting.

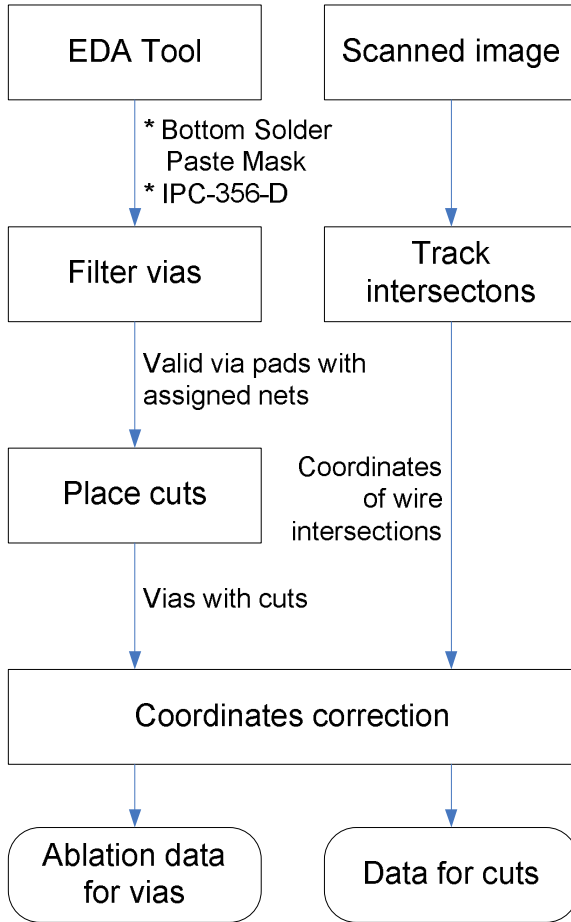


**Figure C.2:** *Data flow and interactions of scripts for generation of the fabrication data*

# D

## Potential temperature measurement circuit

The principle schematic of the proposed measurement circuit is shown in Figure D.1. By imposing a constant current through the copper wire and measuring the resulting voltage drop using the sense lines, the wire resistance can be extracted and therefore, the temperature according to (D.1).  $R_{wire0}$  defines the reference resistance of the wire at a certain temperature  $T_0$ , i.e.  $20^\circ C$ .

A constant current through the wire is ensured by the operational amplifier (OA), which regulates its output such that its (+) and (-) inputs feature the same potential. The instrumental amplifier (IA) boosts the differential signal such that a measurement resolution of  $0.4K/LSB$  is achieved for our demonstrator. The low pass filter reduces noise and avoids aliasing by limiting the signal bandwidth to  $f_c = 160Hz$ . This bandwidth is a compromise between noise reduction and measurement speed. The analog-to-digital converter features a resolution of  $12Bits$ , which translates to a LSB (least significant bit) of  $0.5mV$  using a reference voltage of  $2.048V$ .  $R_2$  can be switched to the circuit that allows applying different currents through the copper wire. This procedure further improves measurement accuracy.

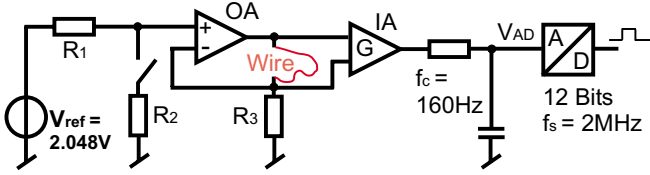


**Figure D.1:** Temperature measurement principle

$$\Delta T = \left( \frac{R_{wire}}{R_{wire0}} - 1 \right) \cdot \frac{1}{\alpha_{Cu}} \quad [Kelvin] \quad (D.1)$$

Formula (D.2) gives the wire resistance in relation to the measured voltages  $V_{ADh}$  and  $V_{ADl}$  at the analog-to-digital converter. The two voltages correspond to the two currents that are generated by switching  $R_2$  on and off the circuit. Due to subtraction of the voltages, constant circuit offsets (e.g. amplifier offsets) are eliminated.

Putting (D.2) into (D.1), the constants  $R_1 - R_3$ ,  $G$  and  $V_{ref}$  cancel out leading to formula (D.3). As a result, the accuracies of these constants become unimportant when using a reference wire resistance  $R_{wire0}$  determined by calibration. In fact, the voltages in formula (D.3) can directly be replaced with the  $bits_x$  correspond to the binary values of the analog-to-digital converter. This then leads to formula (D.4).

$$R_{wire} = \frac{R_3}{G} \cdot \frac{R_1 + R_2}{R_2} \cdot \frac{V_{ADh} - V_{ADl}}{V_{ref}} \quad [\Omega] \quad (D.2)$$

$$T = \left( \frac{V_{ADh} - V_{ADl}}{V_{ADrefh} - V_{ADrefl}} - 1 \right) \frac{1}{\alpha_{Cu}} + T_0 \quad [^{\circ}C] \quad (D.3)$$

$$T = \left( \frac{bits_h - bits_l}{bits_{refh} - bits_{refl}} - 1 \right) \frac{1}{\alpha_{Cu}} + T_0 \quad [^{\circ}C] \quad (D.4)$$

# Glossary

## Scalars

$A$	Absorbance / cross-section area
$B$	Magnetic flux density
$C'$	Capacitance per unit length
$E$	Young's modulus, initial modulus
$F$	Laser fluence / Force
$F_{th}$	Laser ablation threshold
$G'$	Conductance per unit length
$H$	Magnetic field strength
$I$	Current
$L'$	Inductance per unit length
$\Delta L$	Length difference
$Q$	Quality factor
$R'$	Resistance per unit length
$R_s$	Sheet resistance
$R_{DC}$	DC resistance
$P$	Power
$\Delta T$	Temperature difference
$V$	voltage
$Z_0$	Line impedance, Characteristic impedance
$\alpha$	Loss attenuation constant
$\alpha_{eff}$	Effective absorption coefficient
$\beta$	Propagation constant
$\delta$	Skin depth
$\epsilon_0$	Free space permittivity ( $= 8.85419 \cdot 10^{-12}$ F/m)
$\epsilon_r$	(Effective) relative dielectric permittivity
$\gamma$	Complex propagation constant
$\lambda$	Wavelength
$\mu_0$	Free space permeability ( $= 1.25663 \cdot 10^{-6}$ H/m)
$\mu_r$	Relative permeability

$\sigma$	Conductivity
$\varphi$	Phase
$\phi$	magnetic flux
$\omega$	Angular frequency
$c_0$	Light speed ( $= 2.99792 \cdot 10^8$ m/s)
$f$	Frequency
$t$	Metal thickness
$t_d$	Delay time
$\tan\delta$	Dielectric loss tangent
$v_p$	Phase velocity
$w$	Strip width

## Units

1 mil	$1/1000$ in = $0.0254$ mm
1 Neper [Np]	$8.69$ dB
1 tex	$1g/1000m$

## Abbreviations

3D	3 Dimensional
AWG	American Wire Gauge
AR	Axial Ratio
BAN	Body area network
BGA	Ball grid array
CBCPW	Conductor-Backed Coplanar Waveguide
CP	Circular Polarization
CPW	Coplanar Waveguide
CSP	Chip scaled package
CTE	Coefficient of Thermal Expansion
Cu	Copper
DC	Direct Current
DUT	Device Under Test
EDA	Electronic Design Automation
EMC	Electromagnetic compatibility

FEM	Finite Element Method
FGC	Finite-Ground Coplanar Waveguide
FGCPW	Finite-Ground Coplanar Waveguide
FW-CBCPW	Finite-Width Conductor-Backed Coplanar Waveguide
FW-CPW	Finite-Width Coplanar Waveguide
FR4	Flame resistant 4, substrate
GCPW	Grounded Coplanar Waveguide
GND	Ground
HFSS	High Frequency Structure Simulator
IC	Integrated Circuit
IPC	Association Connecting Electronics Industries
JTAG	Joint Test Action Group
LED	Light emitting diode
LP	Linear Polarization
MCM	Multi Chip Module
MSL	Microstrip line
PCB/PWB	Printed Circuit Board/Printed Wiring Board
PET	Polyester
PTFE	Polytetrafluoroethylene
PWR	Power
RF	Radio Frequency
SEM	Scanning Electron Microscope
SMA	Sub-miniature version A, connector
SMD	Surface Mount Devices
SMT	Surface Mount Technology
SNR	Signal-to-noise ratio
SOC	System-on-a-Chip
SOP	Small outline package
SOLT	Short-Open-Line-Thru
SOT	System-on-Textile
TDR	Time domain reflectometry
TDT	Time domain transmission
TL	Transmission Line
TRL	SThru-Reflect-Line

VNA	Vector Network Analyser
WBAN	Wireless body area network
WPAN	Wireless personal area network
XeCl	Xeon-Chlorine



## Bibliography

- [1] Acheson Industries Ltd. *Electrodag PF-410 product datasheet*.  
<http://www.achesonindustries.com>.
- [2] S. J. Adamson and C. Q. Ness. *Dam and Fill Encapsulation for Microelectronic Packages (Whitepaper)*. Asymtek, 2762 Loker Avenue West, Carlsbad, CA 92008, 1999.  
<http://www.asymtek.com>.
- [3] Agilent Technologies Inc. *Agilent 34401A user manual*.  
<http://www.agilent.com>.
- [4] Agilent Technologies Inc. *Agilent 34980A user manual*.  
<http://www.agilent.com>.
- [5] Agilent Technologies Inc. *Agilent E3631 user manual*.  
<http://www.agilent.com>.
- [6] Agilent Technologies Inc. *Hewlett Packard, HP4192 user manual*.  
<http://www.agilent.com>.
- [7] Agilent Technologies Inc. *Hewlett Packard, HP8753E user manual*.  
<http://www.agilent.com>.
- [8] F. Alimenti, P. Mezzanotte, L. Roselli, and R. Sorrentino. Modeling and characterization of the bonding-wire interconnection. *Microwave Theory and Techniques, IEEE Transactions on*, 49:142–150, 2001.
- [9] Altium. *Altium DXP 2004 user manual*, 2004.  
<http://www.altium.com>.
- [10] O. Amft, M. Lauffer, S. Ossevoort, F. Macaluso, P. Lukowicz, and G. Trster. Design of the qbic wearable computing platform. In *ASAP 2004: Proc. 15th IEEE International Conference on Application-specific Systems*, pages 27–29, September 2004.
- [11] Ansoft Corporation, Pittsburg. *Ansoft HFSS user manual*, 2002.  
<http://www.ansoft.com>.
- [12] C. M. A. Ashruf. Thin flexible pressure sensors. *Sensor Review*, 22(4):322–327, 2002.

- [13] C. A. Balanis. *Antenna Theory: Analysis and Design, 2 Edition*. Wiley and Sons Inc, 1996.
- [14] J. A. R. Ball. Characteristic impedance of unbalanced tdr probes. *Instrumentation and Measurement, IEEE Transactions on*, 51:532–536, 2002.
- [15] Bekaert SA. *Bekinox VN datasheet*.  
<http://www.bekaert.com>.
- [16] P. Berry, G. Butch, and M. Dwane. Highly conductive printable inks for flexible and low-cost circuitry. In *Proc. 37th International Symposium on Microelectronics (IMAPS 2004)*, November 2004.
- [17] V. Beyer, F. Kuchenmeister, M. Bottcher, and E. Meusel. Flexible polyimide interposer for csp preparation. In *Adhesive Joining and Coating Technology in Electronics Manufacturing, 1998. Proceedings of 3rd International Conference on*, pages 112–115, 1998.
- [18] W. D. Bjorndahl. Package size and epoxy mass effects on package hermeticity requirements. In *Aerospace Conference, 1997. Proceedings., IEEE*, volume 4, pages 277–283 vol.4, 1997.
- [19] Bluetooth SIG. *Specification of the Bluetooth System, Radio Specification*.  
<http://www.bluetooth.org>.
- [20] S. Brebels, J. Ryckaert, B. Cme, S. Donnay, W. D. Raedt, E. Beyne, and R. P. Mertens. Sop integration and codesign of antennas. *IEEE Transactions on Advanced Packaging*, 27(2):341–351, May 2004.
- [21] W. D. Brown. *Advanced Electronic Packaging : With Emphasis on Multichip Modules*. Wiley-IEEE Press., 1998.
- [22] Cadence. *Cadence Allegro manual*, 2004. <http://www.cadence.com>.
- [23] A. Carullo, A. Ferrero, and M. Parvis. A microwave system for relative humidity measurement. In *Proceedings of the 16th IEEE Instrumentation and Measurement Technology Conference (IMTC)*, volume 1, pages 124–129, May 1999.
- [24] M. Catrysse, R. Puers, C. Hertleer, L. V. Langenhove, H. van Egmond, and D. Matthys. Towards the integration of textile sensors in a wireless monitoring suit. *Sensors and Actuators A: PHYSICAL*, 114(2-3):302–311, 2004.

- [25] D. Cottet, J. Grzyb, T. Kirstein, and G. Tröster. Electrical characterization of textile transmission lines. *IEEE Transactions on Advanced Packaging*, 26(2):182–190, May 2003.
- [26] L. Dall’Acqua, C. Tonin, R. Peila, F. Ferrero, and M. Catellani. Performances and properties of intrinsic conductive cellulose-polypyrrole textiles. *Synthetic Metals*, 146:213–221, 2004.
- [27] R. W. DeVaul, S. J. Schwartz, and A. S. Pentland. Mithril: context-aware computing for daily life. In *MIT Media Lab Whitepaper*, pages 1–9, 2001.
- [28] A. Dhawan, A. M. Seyam, T. K. Ghosh, and J. F. Muth. Woven fabric-based electrical circuits - part i: Evaluating interconnect methods. *Textile Research Journal*, 74(10):913–919, Oct 2004.
- [29] A. Dhawan, A. M. Seyam, T. K. Ghosh, and J. F. Muth. Woven fabric-based electrical circuits - part ii: Yarn and fabric structures to reduce crosstalk noise in woven fabric-based circuits. *Textile Research Journal*, 74(11):955–960, Nov 2004.
- [30] R. Diestel. *Graph Theory*. Springer-Verlag, New York, 2000.
- [31] W. W. Duley. *UV Lasers: effects and applications in materials science*. Cambridge University Press, 1996.
- [32] Elektrisola Feindraht AG. *Textile Wire datasheet*. <http://www.textile-wire.com>.
- [33] Emerson & Cuming. *Stycast 2850 technical datasheet*. <http://www.emersoncuming.com>.
- [34] EPO-TEK. *EPO-TEK E4110 technical datasheet*. <http://www.epotek.com>.
- [35] ESi. *ESi 5330 UV laser uVia Drill datasheet*. <http://www.esi.com>.
- [36] B. Freyman and R. Marrs. Ball grid array (bga): The new standard for high i/o surface mount packages. In *Electronic Manufacturing Technology Symposium, 1993., Proceedings of 1993 Japan International*, pages 41–45, 1993.
- [37] V. Garg, D. Schimmel, D. Stogner, C. Ulmer, D. S. Wills, and S. Yalamanchili. Early analysis of cost/performance trade-offs in mcm systems. *IEEE Transactions on Components, Packaging, and Manufacturing Technology*, 20(3):308–319, 1997.

- [38] F. Gemperle, C. Kasabach, J. Stivoric, M. Bauer, and R. Martin. Design for wearability. In *Proceedings of 2nd IEEE International Symposium on Wearable Computers*, pages 116–122, Oct, 19-20 1998.
- [39] Gesellschaft für intelligente textile Produkte. *ITP*. <http://www.gitp.org>.
- [40] S. Gimpel, U. Möhring, H. Müller, A. Neudeck, and W. Scheibner. Textile-based electronic substrate technology. *Journal of Industrial Textiles*, 33(3):179–189, 2004.
- [41] J. Grzyb, D. Cottet, and G. Tröster. Systematic deembedding of the transmission line parameters on high-density substrates with probe-tip calibrations. In *Proc. 52nd Electronic Components and Technology Conference ECTC2002*, pages 1051–1057, May 2002.
- [42] E. Hirt and G. Troster. Early footprint comparison for area i/o packages and first level interconnect. In *Electronic Components and Technology Conference, 1999. 1999 Proceedings. 49th*, pages 1210–1216, 1999.
- [43] A. S. Hockenberger, S. Koral, and M. A. Wilding. Recovery from strain and shrinkage measurements of poly(m-methylene terephthalate) and poly(ethylene 2,6-naphthalate) fibers. *Textile Research Journal*, 72(2):111–116, 2005.
- [44] Infineon Technologies. *PBA 313 07 Singlestone datasheet, T3130-7V10P02-7600*, 2004. <http://www.infineon.com>.
- [45] IPC. *D-356B - Bare Substrate Electrical Test Data Format*, 2002. <http://www.ipc.org>.
- [46] J. R. Jiang and R. D. Arnell. The effect of substrate surface roughness on the wear of dlc coatings. *Wear*, 238(1):1–9, 2000.
- [47] M. Jones, T. Martin, and Z. Nakad. A service backplane for e-textile applications. In *Workshop on Modeling, Analysis, and Middleware Support for Electronic Textiles (MAMSET)*, pages 15–22, October 2002.
- [48] S. Jung, C. Lauterbach, M. Strasser, and W. Weber. Enabling technologies for disappearing electronics in smart textiles. In *IEEE International Solid-State Circuits Conference*, San Francisco, CA, February 9-13 2003.

- [49] C. Kallmayer, T. Linz, R. Aschenbrenner, and H. Reichl. System integration technologies for smart textiles. *mst news*, 2:42–43, 2005.
- [50] M. Kamon, C. Smithhisler, and J. White. *FastHenry USER'S GUIDE, Version 3.0*. Massachusetts Institute of Technology, 1996. <http://www.fastfieldsolvers.com>.
- [51] Keithley Inc. *Keithley 485 Picoampere meter user manual*. <http://www.keithley.com>.
- [52] H. Kurata, T. Ogata, K. Mitsuka, and H. Matsushita. Over-coated flip-chip fine package development for mcm fabricated with si ic and gaas mmic. In *Proc. 50th IEEE Electronic Components and Technology Conference (ECTC)*, pages 949–954, May 2000.
- [53] M.-Q. Lee and S. Nam. An accurate broadband measurement of substrate dielectric constant. *IEEE Microwave and Guided Wave Letters*, 6(4):168–170, 1996.
- [54] D. Lehn, C. Neely, K. Schoonover, T. Martin, and M. Jones. e-tags: e-textile attached gadgets. In *Communication Networks and Distributed Systems Modeling and Simulation Conference*, January 2004.
- [55] T. Linz, C. Kallmayer, R. Aschenbrenner, and H. Reichl. Embroidering electrical interconnects with conductive yarn for the integration of flexible electronic modules into fabric. In *Proceedings 9th International Symposium on Wearable Computers ISWC 2005*, pages 86–89, October 2005.
- [56] T. Lippert and J. T. Dickinson. Chemical and spectroscopic aspects of polymer ablation: Special features and novel directions. *Chem. Rev.*, 103(2):453–486, 2003.
- [57] T. Lippert, M. Hauser, C. R. Phipps, and A. Wokaun. Polymers designed for laser applications: fundamentals and applications. In *Proc. SPIE*, volume 4760, 2002.
- [58] W.-T. Lo, T. C.-K.C., S.-T. Peng, and C.-H. Lin. Full-wave and experimental investigations of resonant and leaky phenomena of microstrip step discontinuity problems with and without top cover. *IEEE Microwave Symposium Digest, MTT-S International*, 1:473–476, 1994.
- [59] I. Locher, T. Kirstein, and G. Tröster. Packaging-Technologien für textile Substrate. In *DVS/GMM-TAGUNG, Elektronische Baugruppen*

- *Aufbau- und Fertigungstechnik -Die Trends von heute - die Chancen von morgen*, pages 477–482, Feb 2004.

- [60] I. Locher, T. Kirstein, and G. Tröster. Routing methods adapted to e-textiles. In *Proc. 37th International Symposium on Microelectronics (IMAPS 2004)*, November 2004.
- [61] I. Locher, T. Kirstein, and G. Tröster. Temperature profile estimation with smart textiles. In *Proc. 1st International Scientific Conference Ambience 05*, September 2005.
- [62] I. Locher, M. Klemm, T. Kirstein, and G. Tröster. Design and characterization of purely textile patch antennas. *Submitted to IEEE Transactions on Advanced Packaging*.
- [63] F. Lorussi, W. Rocchia, E. P. Scilingo, A. Tognetti, and D. De Rossi. Wearable, redundant fabric-based sensor arrays for reconstruction of body segment posture. *IEEE Sensors Journal*, 4(6):807–818, December 2004.
- [64] LPKF Laser & Electronics AG. *MLD 600x600 HS specifications*. <http://www.lpkf.de>.
- [65] P. Lukowicz, U. Anliker, G. Troster, S. J. Schwartz, and R. W. DeVaul. The weararm modular, low-power computing core. *IEEE Micro*, 21:16–28, May/June 2001.
- [66] S. Mann. On the bandwagon or beyond wearable computing. *Personal Technologies*, 1(4):203–207, 1997.
- [67] R. Marks. A multiline method of network analyzer calibration. *IEEE Transactions on Microwave Theory and Techniques*, 39(7):1205–1215, 1991.
- [68] P. Massey. Mobile phone fabric antennas integrated within clothing. In *Proceedings of the 11th IEE Conference on Antennas and Propagation (IEE Conf. Publ. No. 480)*, volume 1, pages 344–347, April 2001.
- [69] C. Mattei and A. P. Agrawal. Electrical characterization of bga packages. In *Electronic Components and Technology Conference, 1997. Proceedings., 47th*, pages 1087–1093, 1997.
- [70] C. Merritt, K. Tae-Ho, B. Karaguzel, J. Wilson, B. Pourdeyhimi, H. T. Nagle, and E. Grant. Electrical characterization of transmission lines on nonwoven textile substrates. page H4.7, March 2005.

- [71] H. Narushima, Y. Tsukamoto, and J. Koshimura. Electrical aging of adhesive. In *Electrical Insulation and Dielectric Phenomena, 1989. Annual Report., Conference on*, pages 168–172, 1989.
- [72] A. A. Oliner and K. S. Lee. The nature of the leakage from higher modes on microstrip line. In *Microwave Symposium Digest, MTT-S International*, volume 86, pages 57–60, 1986.
- [73] M. Orth. Defining flexibility and sewability in conductive yarns. *Proc. Mat. Res. Soc. Symp. (MRS)*, 736:D1.4.1–D1.4.12, December 2002.
- [74] S. Park, K. Mackenzie, and S. Jayaraman. The wearable motherboard: a framework for personalized mobile information processing (pmip). In *Proc. 39th ACM/IEEE Design Automation Conference (DAC)*, pages 170–174, 2002.
- [75] R. Peek. Liquid encapsulation protects electronic components. *EP&P magazine*, 217:170–180, 2001.
- [76] E. R. Post, M. Orth, P. R. Gershenfeld, and N. Russo. E-broidery: Design and fabrication of textile-based computing. *IBM Systems Journal*, 39(3+4):840–860, 2000.
- [77] J. A. Reynoso-Hernandez. Unified method for determining the complex propagation constant of reflecting and nonreflecting transmission lines. *IEEE Microwave and Wireless Components Letters*, 13(8):351–353, 2003.
- [78] P. Salonen and H. Hurme. A novel fabric wlan antenna for wearable applications. In *Proceedings of the IEEE Antennas and Propagation Society International Symposium*, volume 2, pages 700–703, June 2003.
- [79] P. Salonen, M. Keskilammi, and M. Kivikoski. Single-feed dual-band planar inverted-f antenna with u-shaped slot. *IEEE Transaction on Antennas and Propagation*, 48(8):1262–1264, August 2000.
- [80] P. Salonen, Y. Rahmat-Samii, H. Hurme, and M. Kivikoski. Dual-band wearable textile antenna. In *Proceedings of the IEEE Antennas and Propagation Society International Symposium*, volume 1, pages 463–466, June 2004.
- [81] B. P. Saville. *Physical Testing of Textiles*. CRC Press, Boca Raton FL, 1999.

- [82] H. Schaumburg. *Werkstoffe und Bauelemente der Elektrotechnik: Polymere*. B.G. Teubner Stuttgart, Hamburg, 1997.
- [83] H. Shigesawa, M. Tsuji, and A. A. Oliner. A new mode-coupling effect on coplanar waveguides of finite width. In *Microwave Symposium Digest, 1990., IEEE MTT-S International*, pages 1063–1066 vol.3, 1990.
- [84] R. N. Simons. *Coplanar Waveguide Circuits, Components, and Systems*. John Wiley & Sons, Inc., 2001.
- [85] R. A. Soares, P. Gouzien, P. Legaud, and G. Follot. A unified mathematical approach to two-port calibration techniques and some applications. *IEEE Transactions on Microwave Theory and Techniques*, 37(11):1669–1674, 1989.
- [86] Softswitch. *Softswitch website*. <http://www.softswitch.co.uk>.
- [87] Statex Produktions & Vertriebs GmbH, Bremen, Germany. *Nora technical data sheet*. <http://www.statex.de>.
- [88] Statex Produktions & Vertriebs GmbH, Bremen, Germany. *P130 technical data sheet*. <http://www.statex.de>.
- [89] M. Tanaka and J. Jae-Hyeuk. Wearable microstrip antenna. In *Proceedings of the IEEE Antennas and Propagation Society International Symposium*, volume 2, pages 704–707, June 2003.
- [90] L. K. Teh, M. Teo, E. Anto, C. C. Wong, S. G. Mhaisalkar, P. S. Teo, and E. H. Wong. Moisture-induced failures of adhesive flip chip interconnects. *IEEE Transactions on Components and Packaging Technologies*, 28:506–516, 2005.
- [91] Tektronix Inc. *Tektronix CSA-803A user manual*. <http://www.tektronix.com>.
- [92] Tektronix Inc. *IPA-510 Interconnect Parameter Analyzer, Reference Manual*, 1992.
- [93] Texas Instruments. *MSP430F1232 datasheet*, 2004. <http://www.ti.com>.
- [94] C.-C. Tien, C.-K. C. Tzuang, S. Peng, and C.-C. Chang. Transmission characteristics of finite-width conductor-backed coplanar waveguide. *IEEE Transactions on Microwave Theory and Techniques*, 41(9):1616–1624, 1993.



- [95] W. Tong and A. Teng. Moisture diffusion monitoring in globtop encapsulant with microdielectric sensors. In *Electronic Materials and Packaging, 2000. (EMAP 2000). International Symposium on*, pages 464–469, 2000.
- [96] L. Torrisi, S. Gammino, L. Ando, V. Nassisi, D. Doria, and A. Pedone. Comparison of nanosecond laser ablation at 1064 and 308 nm wavelength. *Applied Surface Science*, 210:262–273, 2003.
- [97] J. P. Troyk, R. Francovik, and J. E. Anderson. Experimental techniques for electrical testing of microelectronics coatings. *IEEE Transactions on Components, Hybrids, and Manufacturing Technology*, 14:428–435, 1991.
- [98] R. R. Tummala, E. J. Rymaszewski, and A. G. Klopfenstein. *Microelectronics Packaging Handbook*. Springer, 1997.
- [99] Varian Inc. *Cary 500, UV-Vis Spectrometer*.  
<http://www.varianinc.com>.
- [100] Velleman Components. *DVM97CM Thermocouple Module datasheet*.  
<http://www.velleman.be>.
- [101] C.-K. W. W.-Sh. Chen, K.-L. Wong. Inset microstripline-fed circularly polarized microstrip antennas. *IEEE Transaction on Antennas and Propagation*, 48(8):1253–1254, August 2000.
- [102] C. Wan, B. Nauwelaers, and W. D. Raedt. A simple error correction method for two-port transmission parameter measurement. *IEEE Microwave and Guided Wave Letters*, 8(2):58–59, 1998.
- [103] Wolfram research. *Definition of absorbance*.  
<http://scienceworld.wolfram.com/physics/Absorbance.html>.
- [104] D. Zenga, K. Yung, and C. Xie. Uv nd:yag laser ablation of copper: chemical states in both crater and halo studied by xps. *Applied Surface Science*, 217:170–180, 2003.



# Curriculum Vitae

## *Personal Information*

Ivo Locher  
Born April 11, 1973  
Zug, Switzerland  
Citizen of Remetschwil AG, Switzerland

## *Education*

- 2002–2005: Ph.D. student at Swiss Federal Institute of Technology (ETH) Zurich
- 2002: M.Sc. degree in Electrical Engineering with focus on Signal Processing from UCLA, USA  
Thesis: *Design and Implementation of iBadge and its Distributed Speech Processing Capability*
- 2000–2002: M.Sc. study in Electrical Engineering at UCLA under Prof. Abeer Alwan and Prof. Mani Srivastava, USA
- 1993–1997: B.Sc. studies at HTA Lucerne. Thesis: *MFSK - Minimum Frequency Shift Keying*
- 1989–1993: School for Engineering at GIBZ, Zug

## *Work*

- 2002–2005: Teaching and research assistant at Electronics Laboratory, ETH Zurich
- 2000–2002: Research assistant at Networked and Embedded Systems Lab, UCLA
- 1999–2000: Test Engineering developer at Ascom/Flextronics
- 1997–1999: Assistant for Telecommunications at HTA Lucerne
- 1989–1993: Professional education as electrical engineer at Landis & Gyr, Zug

